

Large Two-photon Absorption of Highly Conjugated Porphyrin Arrays
and Their in vivo Applications

by

Jong Kang Park

Department of Chemistry
Duke University

Date: _____

Approved:

Warren S. Warren, Co-supervisors

Michael J. Therien, Co-supervisors

Martin C. Fischer

David N. Beratan

Dissertation submitted in partial fulfillment of
the requirements for the degree of
Doctor of Philosophy in the Department of
Chemistry in the Graduate School
of Duke University

2015

ABSTRACT

Large Two-photon Absorption of Highly Conjugated Porphyrin Arrays
and Their in vivo Applications

by

Jong Kang Park

Department of Chemistry
Duke University

Date: _____

Approved:

Warren S. Warren, Co-supervisors

Michael J. Therien, Co-supervisors

Martin C. Fischer

David N. Beratan

An abstract of a dissertation submitted in partial
fulfillment of the requirements for the degree
of Doctor of Philosophy in the Department of
Chemistry in the Graduate School of
Duke University

2015

Copyright by
Jong Kang Park
2015

Abstract

Two-photon excited fluorescence microscopy (TPM) has become a standard biological imaging tool due to its simplicity and versatility. The fundamental contrast mechanism is derived from fluorescence of intrinsic or extrinsic markers via simultaneous two-photon absorption which provides inherent optical sectioning capabilities. The NIR-II wavelength window (1000–1350 nm), a new biological imaging window, is promising for TPM because tissue components scatter and absorb less at longer wavelengths, resulting in deeper imaging depths and better contrasts, compared to the conventional NIR-I imaging window (700–1000 nm). However, the further enhancement of TPM has been hindered by a lack of good two-photon fluorescent imaging markers in the NIR-II.

In this dissertation, we design and characterize novel two-photon imaging markers, optimized for NIR-II excitation. More specifically, the work in this dissertation includes the investigation of two-photon excited fluorescence of various highly conjugated porphyrin arrays in the NIR-II excitation window and the utilization of nanoscale polymersomes that disperse these highly conjugated porphyrin arrays in their hydrophobic layer in aqueous environment. The NIR-emissive polymersomes, highly conjugated porphyrins-dispersed polymersomes, possess superb two-photon excited brightness. The synthetic nature of polymersomes enables us to formulate fully

biodegradable, non-toxic and surface-functionalized polymersomes of varying diameters, making them a promising and fully customizable multimodal diagnostic nano-structured soft-material for deep tissue imaging at high resolutions. We demonstrated key proof-of-principle experiments using NIR-emissive polymersomes for *in vivo* two-photon excited fluorescence imaging in mice, allowing visualization of blood vessel structure and identification of localized tumor tissue. In addition to spectroscopic characterization of the two-photon imaging agents and their imaging capabilities/applications, the effect of the laser setup (e.g., repetition rate of the laser, peak intensity, system geometry) on two-photon excited fluorescence measurements is explored to accurately measure two-photon absorption (TPA) cross-sections. A simple pulse train shaping technique is demonstrated to separate pure nonlinear processes from linear background signals, which hinders accurate quantification of TPA cross-sections.

Dedication

This dissertation is dedicated to Hyejin Yoo, my wife. I thank her for unwavering love, support, and encouragement.

Contents

Abstract	iv
List of Tables.....	xii
List of Figures	xiii
List of Schemes	xix
Acknowledgements	xx
1. Two-photon Excited Fluorescence Microscopy	1
1.1 Motivation of the dissertation.....	1
1.2 Nonlinear absorption.....	3
1.3 Quantification of two-photon excited fluorescence.....	5
1.4 Two-photon fluorophores	10
1.5 Basic components of a two-photon excited fluorescence microscope (TPM)	14
1.6 A new tissue imaging window (NIR-II) for TPM; an approach to enhance performance of TPM	17
1.7 Dissertation goals and outline	22
2. Introduction to Highly Conjugated Porphyrin Arrays and Polymersomes.....	27
2.1 Porphyrin.....	27
2.2 Highly-conjugated ethyne-bridged porphyrin arrays	32
2.3 Polymersome is a soft vesicle	36
2.4 NIR-emissive polymersome.....	37
3. Exceptionally Large Two-Photon Absorption Cross-section of Highly Conjugated Multiporphyrins under NIR-II Wavelength Excitation.....	40

3.1 Introduction.....	40
3.2 Result and discussions.....	44
3.2.1 Linear optical properties of PZn _n	44
3.2.2 Density functional theory calculation on PZn _n	45
3.2.3 Comparative TPA properties of the benchmark porphyrin monomers and PZn ₂	53
3.2.4 Extremely large TPA cross-sections of PZn _n in the NIR-II window.....	59
3.2.5 Theoretical interpretation based on the three essential state model	62
3.2.6 TPA trends evident for PZn _n fluorophores.....	63
3.3 Conclusion.....	68
3.4 Experimental	69
3.4.1 Materials	69
3.4.2 Instrumentation	69
3.4.3 Two-photon absorption cross-section measurement	69
3.4.4 Computational methods.....	70
4. Nano-vesicular Two-photon in vivo Imaging Agent with Super-brightness for NIR-II Wavelength Excitation	71
4.1 Introduction.....	71
4.2 Result and discussions.....	74
4.2.1 Sample characterization and optimization of PZn _n -polymersome	74
4.2.2 Linear absorption and emission of PZn _n in PEO-PBD	77
4.2.3 Two-photon absorption of PZn _n in PEO-PBD	79

4.2.4 Verification of two-photon excited fluorescence of nano-sized emissive polymersomes under imaging conditions	82
4.3 Conclusion	92
4.4 Experimental	93
4.4.1 Materials	93
4.4.2 Polymersome synthesis	94
4.4.3 Cryogenic Transmission Electron Microscopy (Cryo-TEM)	94
4.4.4 Dynamic Light Scattering	95
4.4.5 Linear and nonlinear optical property characterization	95
4.4.6 Skinfold window chamber and cancer model.....	96
4.4.7 Two-photon imaging	97
4.4.8 Image analysis.....	98
5. Femtosecond Pulse Train Shaping Improves Two-photon Excited Fluorescence Measurements	99
5.1 Introduction.....	99
5.2 Result and discussions.....	104
5.2.1 Absorption and emission spectra of DD	104
5.2.2 Conventional multiphoton emission measurements	104
5.2.3 Estimation of relative linear and nonlinear fluorescence for weak and strong focusing.....	106
5.2.4 Hot-band model of linear absorption.....	107
5.2.5 Pulse train shaping technique.....	111
5.2.6 Estimation of two-photon absorption cross section of DD.....	116

5.2.7 Other effects potentially influencing multiphoton emission measurements..	119
5.3 Conclusion.....	121
5.4 Experimental.....	123
5.4.1 Materials.....	123
5.4.2 1 kHz power study.....	123
5.4.3 76 MHz power study.....	124
5.4.4 Pulse shaping technique.....	124
6. Two-photon Absorption of Various NIR-Emissive Porphyrin Arrays under NIR-II Wavelength Excitation.....	125
6.1 Introduction.....	125
6.2 Result and Discussions.....	130
6.2.1 Linear optical properties of highly conjugated porphyrins.....	130
6.2.1.1 Linear optical properties of meso-to-meso ethyne-bridged porphyrin arrays (DA-derived porphyrin arrays and PZn ₇).....	130
6.2.1.2 Linear optical properties of BTD-conjugated porphyrin arrays.....	134
6.2.2 Two-photon absorption of highly conjugated porphyrin arrays.....	139
6.2.2.1 Two-photon absorption of meso-to-meso ethyne-bridged porphyrin arrays (DA-derived porphyrin arrays and PZn ₇).....	139
6.2.2.2 Two-photon absorption of BTD-conjugated porphyrin arrays.....	142
6.3 Conclusion.....	144
6.4 Experimental.....	145
6.4.1 Materials.....	145
6.4.2 Linear absorption and emission spectra measurement.....	146

6.4.3 Two-photon absorption cross-section measurement	146
References	148
Biography	163

List of Tables

Table 1. Two-photon absorption cross-sections of commonly used fluorophores for $\lambda_{\text{ex}} = 700\text{--}1000\text{ nm}^{\text{a}}$	13
Table 2. Spectroscopic parameters of <i>meso</i> -to- <i>meso</i> ethyne-bridged (porphinato)zinc(II) oligomers measured in THF (ϕ : quantum yield, σ_2 : two-photon absorption cross-section).....	45
Table 3. Summary of calculated excited states of PZn_n and the corresponding assignment of the major states of one-photon absorption (OPA) and TPA transitions. Major contributions to each state were color-coded to clarify the characteristics of the responsible transition (black : bonding \rightarrow nonbonding, blue : bonding \rightarrow bonding, and pink : nonbonding \rightarrow nonbonding).....	51
Table 4. Summary of linear and nonlinear spectroscopic parameters of <i>meso</i> -to- <i>meso</i> ethyne-bridged (porphinato)zinc(II) oligomers incorporated into aqueous dispersed OB18 polymersome (ϕ : fluorescence quantum yield and σ_2 : two-photon absorption cross-section).....	78
Table 5. PZn_n copy number per vesicle as a function of vesicle size for a 5 mol% membrane loading.....	81
Table 6. Summary of Spectroscopic Parameters of Studied Oligomeric Porphyrins	133

List of Figures

- Figure 1. Schematic design of a typical two-photon microscope. Red lines indicate laser beam from Ti:Sapphire laser and blue lines indicate two-photon excited fluorescence. Adopted from So et al. (2000).¹² 15
- Figure 2. Absorption and scattering properties of typical biological components. Absorption properties were adopted from data set available in <http://omlc.org>. Scattering property was adopted from T. Matthews's dissertation (2012).²³ 19
- Figure 3. Two photon fluorescence images of cortical vasculature in a mouse brain. (a) Reconstructed z-stack images for 3D and (b) four individual images beyond 1 mm depth with scale bars of 50 μm for both (a) and (b). Adopted from Kobat et al. (2011).²⁴ 20
- Figure 4. Structure of porphyrin with the α -, β -, and *meso*-positions indicated. *M* in the center of the porphyrin ring represents metals (or H_2 for free-base porphyrin) that can be coordinated by binding with four nitrogens..... 28
- Figure 5. Linear absorption spectrum and its molecular structure of Tetraphenylporphyrin [$\text{H}_2(\text{TPP})$] in CCl_4 30
- Figure 6. (A) Representative highest occupied molecular orbitals (HOMO) and lowest unoccupied molecular orbitals (LUMO) of porphyrin. Blue and red colors represent the phase of electronic wavefunctions and the size represents the magnitude of probability of electronic distribution. (B) (top) Corresponding HOMO and LUMO diagram with possible transitions from HOMOs to LUMOs depicted by arrows. (bottom) Origin of two main optical transitions (Soret and Q) of porphyrins with corresponding symmetry. Adopted from Senge et al. (2014).⁴⁵ 31
- Figure 7. Molecular structure of *meso*-to-*meso* ethyne-bridged (porphinato)zinc(II) oligomers and their linear absorption spectra in THF. Inset shows the emission spectra of porphyrin arrays. Adopted from Duncan et al. (2006).⁴⁷ 34
- Figure 8. (Top) Schematic description of the formation of emissive polymersomes in aqueous medium. (Bottom) Imaged nano-sized and micron-sized polymersomes by cryo-TEM and by conventional confocal fluorescence microscope, respectively. Imaging of tumor mouse model was demonstrated by PZn_3 -dispersed polymersomes that visualize tumor region imaged by a whole animal fluorescence imager. Adopted from Ghoroghchian et al. (2005 and 2007).^{58,60} 38

Figure 9. (A) Development of the four frontier orbital bands in PZn_n . Green boxes enclose the nearly-degenerate nonbonding orbitals, while the bonding orbitals are evenly dispersed between the purple lines. (B) Electronic spectra (lines) of PZn_n compounds measured in THF solvent, and (squares) TDDFT-calculated transition energies of these same compounds. Computational data obtained using PCM solvation model (THF) and M11/6-311g(2d). 47

Figure 10. Frontier orbitals of PZn_2 (D_{2h} point group) plotted as 0.02 isodensity surfaces along with a diagram comparing their calculated energies. Those which comprise the highly delocalized bonding and antibonding bands are labeled H (HOMO), L (LUMO), H-1, L+1, etc. with bonding and antibonding bands explained in text. Computational data obtained using PCM solvation model (THF) and M11/6-311g(2d). The generation of TPA-allowed u (ungerade)- u or g (gerade)- g transitions explains the enormous TPA at an energy nonresonant with one-photon transitions for PZn_2 48

Figure 11. Frontier orbitals of PZn_3 plotted as 0.02 isodensity surfaces along with a diagram comparing their calculated energies. Computational data obtained using PCM solvation model (THF) and M11/6-311g(2d). 49

Figure 12. Frontier orbitals of PZn_5 plotted along with a diagram comparing their calculated energies. Computational data obtained using PCM solvation model (THF) and M11/6-311g(2d). 50

Figure 13. One- (solid line) and two-photon (black dot) absorption spectra of ZnTPP and EPZnE in THF [including magnified linear absorption spectra (blue lines) in the Q-band regions]. TPA spectra are plotted with doubled laser excitation energy for direct comparison with one-photon absorption spectra..... 55

Figure 14. Energy diagram of ZnTPP and PZn_2 comparing their frontier orbital energies. Computational data obtained using PCM solvation model (THF) and M11/6-311g(2d). 55

Figure 15. One- (solid line) and two-photon (black dot) absorption spectra of PZn_n in THF, with calculated energies for TPA states depicted as colored dotted lines. TPA spectra are plotted with doubled laser excitation energy for direct comparison with one-photon absorption spectra; computational data obtained using PCM solvation model (THF) and M11/6-311g(2d). 57

Figure 16. States diagram of PZn_n from linear (Q_x and B) and two-photon absorption (S_i and S_{TPA}) spectrum measured in THF; S_i is the intermediate state, Q_x is the x-polarized Q-state, S_{TPA} and the final two-photon active state, and B is the Soret state. The widths of

B-band were calculated from the difference of the highest- and the lowest-energy Soret peaks in the linear absorption spectra.	63
Figure 17. Single and multiple Gaussian fits to the two-photon absorption spectra of PZn _n in THF. TPA spectra are plotted with doubled laser excitation energy (bottom x-axis) to clarify the final two-photon accessible states.	66
Figure 18. Plot of calculated relative molecular length (<i>L</i>) and number of π -electron (<i>N_e</i>) dependence of σ_2 and experimental σ_2 of PZn _n	67
Figure 19. Cryogenic transmission electron microscopy (cryo-TEM) images of nano-sized PZn _n -based polymersomes. (In all three images, scale bar = 100 nm.)	76
Figure 20. Extinction coefficient and emission spectra of PZn _n -based polymersomes dissolved in deionized water (DIW).	78
Figure 21. Two-photon absorption cross-sections of PZn _n -based polymersomes on a per chromophore basis in DIW. Power studies were performed to confirm quadratic dependence of fluorescence signal.	80
Figure 22. Depth profile of two-photon excited fluorescence of nano-sized 5 mol% (A) PZn ₃ - and (B) PZn ₅ -based polymersomes in 1 mm cuvette under a microscope using 10x objective (λ_{ex} = 1100 nm, input power = 4 mW for PZn ₃ -based polymersome and 8 mW for PZn ₅ -based polymersome, respectively). A z-independent offset observed in PZn ₅ -based polymersome, which we attribute to linear-excited fluorescence. The power scaling of PZn ₅ -based polymersomes display a slope of ~1.4 while PZn ₃ -based polymersomes display quadratic dependence to excitation power.	84
Figure 23. Blood vessel imaging 2 hrs after tail vein injection of PZn ₃ -based polymersomes. (A) Stitched bright field microscopy images of a part of the dorsal window chamber. (B) Stitched two-photon excited fluorescence images of the corresponding area using low magnitude objective (10x/0.25) under 1100 nm excitation. Scale bar = 200 μ m. Input power = 12.8 mW. (C) Stitched two-photon excited fluorescence images using an objective of high magnification (40x/0.8W) for the region marked with a white box in (B). Scale bar = 50 μ m. Input power = 7.6 mW. The depth of the imaged region is ~200 μ m from the surface. (D) Reconstructed 3D view of blood vessels from individual z-stack images sampled every 2 μ m (40x/0.8W objective). Images were acquired at 256x256 or 512x512 pixel size. Two-photon excited fluorescence images were post-processed to reduce the stripe artifacts from mouse breathing (see Experimental section).	87

Figure 24. Comparison of two-photon excited fluorescence images ($\lambda_{\text{ex}} = 1100 \text{ nm}$, $P_{\text{in}} = 12.7 \text{ mW}$) from dorsal window chamber of a control mouse before (A) and 2 hrs after (B) tail vein injection of PZn₃-based polymersomes. The identical intensity scale was applied for two images. Scale bar = 200 μm . Post processing was applied for (B) to lessen stripe artifacts from mouse breathing. 88

Figure 25. Comparison of two-photon excited fluorescence images from a dorsal window chamber in a control mouse over time. Blood vessel images were obtained at 2 hr and 24 hr time points after PZn₃-based polymersome injection. Input power was 12.8 mW through a 10 \times /0.25 objective lens. The depth of the imaged region is $\sim 200 \mu\text{m}$ from the surface. Images were acquired at a 256 \times 256 pixel size. Two white rectangular boxes indicate the regions selected to calculate signal-to-background ratio. We applied post processing for two-photon excited fluorescence images to lessen the stripe artifacts arising from mouse breathing. 89

Figure 26. Two-photon excited fluorescence images of excised spleen, liver, and kidney using 1100 nm excitation. The organs were excised 26 hr after PZn₃-based polymersome injection. The top images were obtained using 10 \times /0.25 objective (scale bar = 100 μm) and the bottom images were obtained using 40 \times /0.8W objective (scale bar = 50 μm). The same intensity scale was used for 10 \times liver and 10 \times kidney images for direct comparison of the signal from PZn₃-based polymersomes. Input power was 12.8 mW for 10 \times objective and 7.6 mW for 40 \times objective. 90

Figure 27. Stitched bright-field and two-photon excited fluorescence images (10 \times /0.25 objective) of the dorsal window chamber in a tumor-bearing mouse 36 hrs after PZn₃-based polymersome injection. Tumor regions highlighted by accumulated PZn₃-based polymersomes are indicated by dotted circles. Input power was 12.7 mW. Scale bar = 200 μm 92

Figure 28. Linear electronic absorption and emission (inset) spectra of DD in THF solvent. 102

Figure 29. Logarithmic plots of the emission intensity of DD and R6G as a function of peak excitation intensity, $I_{\text{peak}} = \left(2 / \pi w_0^2\right) \left(P_{\text{avg}} / \sqrt{\pi} \tau_p f_p\right) (1 / h\nu)$ where w_0 is the beam waist, P_{avg} is the average power (in W), τ_p is the pulse duration (at 1/e of the temporal intensity), and f_p is the repetition rate; for comparison, $10^{28} \text{ photons cm}^{-2} \text{ s}^{-1}$ at $\lambda=800 \text{ nm}$ corresponds to $2.5 \times 10^9 \text{ W cm}^{-2}$. The numbers in the plots indicate the local power scaling within the indicated range (the slope in the log-log plot). The symbols are

measured data; the solid blue line in the left panel is a nonlinear least-squares fit to the sum of a linear and a quadratic component..... 103

Figure 30. Logarithmic plot of the emission intensity of DD as a function of excitation intensity with a confocal-type measurement (black dots : iris fully opened, red dots : iris closed) using the 76 MHz setup ($\lambda_{\text{ex}} = 800 \text{ nm}$). The respective power scaling is indicated in the graph..... 105

Figure 31. Logarithmic plot of the emission intensity of DD as a function of excitation intensity with the 1 kHz setup (left) and 76 MHz setup (right) at room temperature and 77 K ($\lambda_{\text{ex}} = 800 \text{ nm}$). The numbers on each data set indicate the local power scaling (the slope in the log-log plot). 108

Figure 32. Linear absorption and emission spectra of R6G in methanol (λ_{ex} was 500 nm for the emission spectrum). 110

Figure 33. Logarithmic plot of the emission intensity of R6G as a function of excitation intensity with the 76 MHz setup at room temperature ($\lambda_{\text{ex}} : 630 \text{ nm}$). The numbers on each data set indicate the local power scaling (the slope in the log-log plot). 110

Figure 34. (a) Schematic of the pulse train shaping technique where T is the total period of the pulse train, t is the duration of one on-off cycle, and N is the number of on-off cycles. Red lines represent individual pulses of a high-repetition rate laser (not to scale). Calculated “in-phase” and “out-of-phase” components of a lock-in amplifier’s signal as a function of N at frequency $f=1/T$ for the case of linear fluorescence (b) and two-photon fluorescence (c). 112

Figure 35. In-phase and out-of-phase components of pulse train shaping fluorescence signals in (a) R6G and (b) DD as a function of N (the number of on-off cycles). Measurements were performed with the 76 MHz system at $\lambda_{\text{ex}} = 800 \text{ nm}$ and $T = 2 \text{ ms}$. (c) Logarithmic plot of the in-phase component of the emission intensity of DD as a function of excitation intensity at $N = 200$ and $T = 2 \text{ ms}$; the power scaling is indicated in the graph. 114

Figure 36. The detection of the in-phase component of R6G and DD as a function of N (the number of on-off cycles). Measurements were performed with the 76 MHz system at $\lambda_{\text{ex}} = 800 \text{ nm}$ and $T = 2 \text{ ms}$ 115

Figure 37. (a) Transient absorption spectra of DD in THF under aerated condition. Delay times are at 30, 70, 130, 220, 380 and 1240 ns ($\lambda_{\text{ex}} = 550$ nm). (b) Decay profiles of the excited state at 510 nm.....	120
Figure 38. Frequency responses of R6G and DD under 80 MHz laser excitation. Experimental data and theoretical fitting line are represented by dots and solid lines, respectively ($\lambda_{\text{ex}} = 800$ nm). Lifetimes were fitted as 5.9 ns and 1.85 ns for R6G and DD, respectively.....	121
Figure 39. One- (solid line) and two-photon (blue dot) absorption spectra of donor-acceptor type <i>meso-to-meso</i> ethyne-bridged porphyrins arrays and <i>meso-to-meso</i> ethyne-bridged porphyrin heptamer in THF. While TPA spectra are plotted with doubled laser excitation wavelengths (bottom axis) for direct comparison with one-photon absorption spectra, original laser excitation wavelengths for TPA spectra are indicated at top axis.	132
Figure 40. Normalized emission spectra of donor-acceptor type <i>meso-to-meso</i> ethyne-bridged porphyrin arrays and <i>meso-to-meso</i> ethyne-bridged porphyrin heptamer (PZn ₇) measured by 480 nm excitation in THF.	134
Figure 41. One- (solid line) and two-photon (blue dot) absorption spectra of PZn-(BTD-PZn) _n in toluene. While TPA spectra are plotted with doubled laser excitation wavelengths (bottom axis) for direct comparison with one-photon absorption spectra, original laser excitation wavelengths for TPA spectra are indicated at top axis.	137
Figure 42. One- (solid line) and two-photon (blue dot) absorption spectra of BTD-PZn _n -BTD in THF [including magnified two-photon absorption spectra of BTD-PZn-BTD for clarity]. While TPA spectra are plotted with doubled laser excitation wavelength (bottom axis) for direct comparison with one-photon absorption spectra, original laser excitation wavelength for TPA spectra are indicated at top axis.	138
Figure 43. Emission spectra of PZn-(BTD-PZn) _n and BTD-PZn _n -BTD measured in toluene.	139
Figure 44. Two-photon absorption spectra of PZn-(BTD-PZn) _n and BTD-PZn _n -BTD measured in Toluene. While TPA spectra are plotted with doubled laser excitation wavelength (bottom axis), original laser excitation wavelength for TPA spectra are indicated at top axis.	143

List of Schemes

Scheme 1. Molecular structures of studied porphyrinoids.....	43
Scheme 2. (A) Molecular structure of bis-, tris-, and pentakis(porphinato)zinc(II) (PZn _n) arrays. (B) Schematic structure of an emissive polymersome	75
Scheme 3. Molecular structure of DD	101
Scheme 4. Molecular structures of studied donor-acceptor type <i>meso-to-meso</i> ethyne-bridged porphyrin arrays and <i>meso-to-meso</i> ethyne-bridged porphyrin heptamer (PZn ₇)	128
Scheme 5. Molecular structures of studied benzothiadiazole (BTD)-conjugated porphyrin arrays	129

Acknowledgements

First and foremost I would like to thank God for life through Jesus Christ and the opportunity to study at Duke.

I would also like to give my deepest gratitude to my advisors Drs. Warren Warren and Michael Therien for their support and patient understanding for the past 6 years. Without their willingness to help and guide me, I could not have completed my Ph.D. Working as a joint student between the two groups has been a great opportunity providing the environment to work with great scientists and engineers and to work on various laser setups. Also my third (unofficial) advisor, Dr. Martin Fischer, deserves my sincere appreciation for his invaluable support and advice on every single project that I have worked on at Duke. If I know anything about optics correctly, the knowledge is from him, who spent thousands of hours to teach me optics, electronics, and chemical physics. I am also grateful for the support and guidance from my last committee member, Dr. David Beratan, in my graduate life. He is a great scientist and teacher; I really enjoyed his electron transfer class.

I would like to express my gratitude to the (current and former) Warren group and Therien group members. I must single out several people who have provided tremendous contributions to my research projects: Dr. Melanie O'Sullivan who did the most important parts of the polymersome project, Dr. (and now a Professor) Jesse Wilson who was always willing to help solve problems in my research and personal life,

Dr. Jeff Rawson who provided various porphyrin samples and performed DFT calculations, Dr. Simone Degan who generously prepared mice for iv vivo two-photon imaging, Dr. Kimihiro Susumu (a former Therien group member whom I have never met in person) who synthesized various porphyrin arrays that I studied, Yusong Bai who always provided help for sample preparation and chemistry problems, Dr. Wei Qi who provided BTD-conjugated porphyrins, and Ruobing Wang who provided porphyrin samples. I would also like to acknowledge Dr. Jaehong Park and Dr. Ian Stanton for their input in the early stage of my Ph. D. work. Also, special thanks go to Dr. Paco Robles, George Bullard, Kevin Zhou, and Peter Jeong (and again to Drs. Melanie O'Sullivan, Jeff Rawson, Jesse Wilson, Simone Degan, Kimihiro Susumu) for their assistance in my dissertation writing. Even though I did not mention every group members' name here, it does not mean that they are not important figures; working with you guys was such a blessing to me.

I should not forget a few people out of the two groups: Dr. Todd Warner who demonstrated how to think as a scientist and teach concepts to others and Mr. Richard Nappi who opened up a new world into machining for me and also guided me to make numerous optomechanical parts for a multimodal microscope project. I am also thankful for financial supports from several organizations: the Joe Taylor Adams fellowship, the John T. Chambers scholar, and the APS-DLS travel grant.

Last but not least, I would like to express my love to my friends, my wife and parents who have given me their constant support and love.

1. Two-photon Excited Fluorescence Microscopy

1.1 Motivation of the dissertation

Molecular imaging based on optical nonlinearity provides high-resolution structural and functional information of specimens originating from molecular-specific nonlinear light-matter interaction. Among various nonlinear microscopic techniques, two-photon excited fluorescence microscopy (TPM) has now become one of the standard biological imaging tools for deep tissue imaging, thanks to its simplicity and versatility. TPM is often associated with near-IR (NIR) wavelengths of 700–1000 nm (NIR-I, a conventional biological imaging window) excitation which is easily accessible by Ti:Sapphire lasers. NIR-I excitation for TPM induces less scattering and less absorption from tissue components resulting in deeper imaging depth when compared to the depth limit of linear fluorescence microscopy which utilizes UV-vis wavelength excitation. While there has been extensive work utilizing NIR-I excitation for TPM, recent advances in laser technology have opened up the opportunity to explore a new biological imaging window of 1000–1350 nm (NIR-II) as excitation wavelengths, which is promising to extend the limits of imaging depth and contrast of TPM. Further enhancement of TPM using the NIR-II imaging window is, however, impeded by a dearth of bright and safe two-photon fluorescent imaging agents suitable for the spectral window.

Highly conjugated porphyrin arrays with *meso*-to-*meso* connectivity define a class of exceptional NIR-emissive chromophores possessing high fluorescence quantum

yields; along with their outstanding chemical and photochemical stabilities and excellent biocompatibility, this makes them promising candidates for contrast agents in biomedical imaging. We explore two-photon absorption of various highly conjugated porphyrin arrays with *meso-to-meso* connectivity focused on the NIR-II biological imaging window. Polymersomes, self-assembled vesicles made from diblock copolymer units, provide hydrophobic bilayers suitable for dispersion of the multiporphyrin fluorophores in aqueous environment. Importantly, nanoscale polymersomes afford the chemical stability, drug delivery capacity, and biocompatibility necessary for developing these structures as impressive diagnostic and therapeutic agents.

Thus the overarching goal of this dissertation work's is to design, characterize, and exploit novel two-photon imaging markers utilizing the highly conjugated porphyrin arrays dispersed in polymersomes optimized for NIR-II wavelength excitation toward deeper, brighter, and safer two-photon in vivo imaging.

The rest of this chapter will provide a brief overview on nonlinear light-matter interaction especially focused on two-photon absorption, which is the simultaneous absorption of two photons reaching a state of twice the energy of the individual photon, and TPM in which two-photon excited fluorescence provides three-dimensional optical sectioning capability with subcellular resolution. The last section of this chapter will provide an outline of the dissertation as guidance for the use of readers.

1.2 Nonlinear absorption

When photons pass through materials multiple phenomena can happen: reflection, refraction, scattering, and absorption. Absorption, often times followed by fluorescence, is of particular interest for spectroscopy and optical imaging because intensity change and consequent dynamics of absorbers induced by light absorption provides extensive information about the specimen by simply measuring the amount of light absorbed/emitted or by further temporal and spectral analysis.

For traditional linear (one-photon) absorption, the rate of absorption can be described by

$$\frac{dI}{dz} = -\alpha \cdot I = -\sigma_1 \cdot N \cdot I \quad (1.1)$$

where α is the linear absorption coefficient, σ_1 is the one-photon absorption cross-section (cm^2), N is the number of density of the absorber, and I is the incident light intensity. The one-photon absorption cross-section (cm^2) can be converted a molar extinction coefficient (ϵ , $\text{M}^{-1}\text{cm}^{-1}$) that is a more familiar concept to chemists by

$$\epsilon = \frac{N_A}{10^3 \ln(10)} \sigma_1 \quad (1.2)$$

where N_A is the Avogadro constant.

When light intensity gets stronger, the probability of multiphoton absorption increase nonlinearly described by Taylor expansion of eq (1.1)

$$\frac{dI}{dz} = -\alpha \cdot I - \beta \cdot I^2 - \gamma \cdot I^3 - \dots \quad (1.3)$$

The probability of multiphoton process depends on coefficients of the corresponding n-th order process and the input light intensity. For two-photon absorption (TPA), described by βI^2 in eq (1.3), the first theoretical consideration was developed by Goeppert-Mayer in 1931.¹ The absorption probability of two-photon absorption cross-section is described by σ_2 , two-photon absorption cross-section, with the GM (Goeppert-Mayer, 1 GM = 10^{-50} cm⁴s/photon) unit to honor her seminal work on two-photon absorption. To give a sense of comparison between the probability of one- and two-photon absorption, the one-photon absorption cross-section (σ_1) of typical organic chromophores is of the order of $\sim 10^{-17}$ cm² and two-photon absorption cross-section (σ_2) of a typical two-photon chromophores is of the order of $\sim 1 \times 10^{-50}$ cm⁴ s photons⁻¹ (1 GM). TPA is, thus, observable only when high intensity light (typically $> 10^{24}$ photons cm⁻² s⁻¹) is applied because TPA signal increases with quadratic dependence on incident light intensity. This explains why it took ~ 30 years after the theoretical prediction to demonstrate two-photon absorption experimentally in 1961 by Kaiser and Garrett soon after the laser was invented.² In recent years, the development of sub-ps laser enabled access to two-photon absorption more easily. At high intensity excitation conditions, higher order absorption processes than one- and two-photon absorption start to contribute due to n-th power dependence of n-th order absorption. Although high order absorption processes are beyond the scope of this dissertation, they are becoming more interesting topics of research, especially in biological imaging, as high power lasers at long NIR region become more accessible. In addition, it is noteworthy to mention that

there are multiple nonlinear light-matter interactions such as second-harmonic generation (SHG), third harmonic generation (THG), stimulated Raman scattering (SRS), and coherent anti-stokes Raman scattering (CARS), other than nonlinear absorption. All of these processes have been utilized for nonlinear microscopy.³

Beyond the scientific interest of two-photon absorption of materials as a tool to explore two-photon allowed excited states that cannot be directly accessed by linear absorption, the most exciting advantage of TPA was demonstrated with TPM first by Webb as a imaging tool.⁴ The most important merit of TPM is its intrinsic optical sectioning capability since two-photon excited fluorescence occurs only at focus where light intensity is efficiently high. Now TPM has become a standard imaging tool for biological research.

1.3 Quantification of two-photon excited fluorescence

It is crucial to understand the effect of laser parameters to the probability of TPA and the measurement of TPA cross-section. While rigorous theoretical analysis for generic multiphoton absorption has been worked by Xu et al.,⁵ here I will summarize the key components of TPA which will be critical to understand the results and discussion in this dissertation.

In a particular measurement condition for laser excitation, the total number of photons absorbed by two-photon excitation as a function of time and space is given by

$$N_{abs}(t) = \int_V d\mathbf{r} \sigma_2 C(\mathbf{r}, t) I^2(\mathbf{r}, t) \quad (1.4)$$

where σ_2 is the two-photon absorption cross-section, $C(\mathbf{r},t)$ is the concentration of an absorber, and $I(\mathbf{r},t)$ is the incident laser intensity. Assuming absorption induces no photo-bleaching and photo-degradation, the concentration of an absorber can be treated as a constant C . Moreover, in the case where the spatial and temporal part can be separated we have

$$N_{abs}(t) = \sigma_2 C I_0^2(t) \int_V d\mathbf{r} S^2(\mathbf{r}) \quad (1.5)$$

where $I_0(t)$ and $S(\mathbf{r})$ correspond to the temporal and spatial function of incident light.

Then the number of fluorescence photon by two-photon absorption collected per unit time is given by

$$F(t) = \frac{1}{2} \phi \eta N_{abs}(t) = \frac{1}{2} \phi \eta \sigma_2 C I_0^2(t) \int_V d\mathbf{r} S^2(\mathbf{r}) \quad (1.6)$$

where ϕ is the fluorescence quantum efficiency (we assume fluorescence quantum efficiency by two-photon excitation is the same as by one-photon excitation), η is the collection efficiency of the detection system.

In a laboratory, only the time-averaged fluorescence photon flux can be measured

$$\langle F(t) \rangle = \frac{1}{2} \phi \eta \sigma_2 C \langle I_0^2(t) \rangle \int_V d\mathbf{r} S^2(\mathbf{r}) \quad (1.7)$$

Because detectors generate signal proportional to $\langle I(t) \rangle^2$ not $\langle I^2(t) \rangle$, we can rewrite equation above with average intensity

$$\langle F(t) \rangle = \frac{1}{2} \phi \eta \sigma_2 g^{(2)} C \langle I_0(t) \rangle^2 \int_V d\mathbf{r} S^2(\mathbf{r}) \quad (1.8)$$

where $g^{(2)}$, a 2nd-order temporal coherence of the excitation beam, is defined by

$$g^{(2)} = \frac{\langle I_0^2(t) \rangle}{\langle I_0(t) \rangle^2} \quad (1.9)$$

While $g^{(2)}$ is 1 for a single-mode continuous wave laser, $g^{(2)}$ for a pulsed laser is given by⁵

$$g^{(2)} = \frac{g_p^{(2)}}{f\tau} \quad (1.10)$$

$$g_p^{(2)} = \frac{\tau \int_{-1/(2f)}^{1/(2f)} I_0^2(t) dt}{\left[\int_{-1/(2f)}^{1/(2f)} I_0(t) dt \right]^2} \quad (1.11)$$

where f is the repetition rate of the laser, τ is the full width at half-maximum (FWHM) pulse duration, and $g_p^{(2)}$ is dimensionless quantity which depends on the shape of laser pulse. For a Gaussian pulse one can easily find that $g_p^{(2)} = 0.66$. For a typical laser system, a mode-locked Ti:Sapphire laser with 80-MHz repetition rate and ~100-fs pulse duration, that is employed for TPM $g^{(2)}$ is about 10^5 . Thus, although CW laser can be used to excite chromophores for two-photon absorption, a few hundred fs-pulsed lasers provide five orders of magnitude signal enhancement compared to CW lasers for two-photon excitation under the same average power and the same excitation geometry.

For most cases, lasers with TEM₀₀ mode provide Gaussian beam profile and its spatial distribution function $S(\mathbf{r})$ is given by

$$S(\mathbf{r}) = S(\rho, z) = \frac{w_0^2}{w^2(z)} \text{Exp} \left[-\frac{2\rho^2}{w^2(z)} \right] \quad (1.12)$$

where z is the distance for the narrowest point of the beam along the optical axis, ρ is the radial distance from the optical axis. Gaussian beam width, $w(z)$, is given by

$$w(z) = w_0 \left[1 + \left(\frac{z}{z_R} \right)^2 \right]^{1/2} \quad (1.13)$$

$$z_R = \frac{n_0 \pi w_0^2}{\lambda} \quad (1.14)$$

where z_R is called the Rayleigh range which corresponds to the distance from the center of the beam where the beam size is $\sqrt{2}w_0$. The spatial distribution function is strongly dependent on excitation geometry. The most relevant excitation condition for single-point excitation in conventional two-photon microscopy employing MHz lasers is the thick sample limit ($z_R \ll l$) or tight focusing geometry using an objective lens where the Rayleigh range is much smaller than sample thickness (l). In this case, numerical calculations with the paraxial approximation show that⁵

$$\int_V dr S^2(\mathbf{r}) \approx \frac{8n\lambda^3}{\pi^3 (NA)^4} \quad (1.15)$$

where NA (the numerical aperture) = $n \sin \theta$, n is the refractive index, and θ is the half-angle of collection for the lens.

Using the relation of $I(t)$ and P , the incident power which is measured by

experiment, $I_0(t) = \frac{\pi (NA)^2}{\lambda^2} P(t)$, we can obtain the time-averaged two-photon excited

fluorescence photon flux for the thick sample limit

$$\langle F(t) \rangle = \frac{1}{2} \phi \eta \sigma_2 C \frac{g_p}{f \tau} \frac{8n_0 \langle P(t) \rangle^2}{\pi \lambda} \quad (1.16)$$

In this limit, experimentally detected two-photon excited fluorescence induced by pulsed laser is quadratically dependent on the average incident power and inversely proportional to the pulse width and repetition rate of lasers but dependent not by the size of focal spot. This fact that two-photon absorption is independent of the focusing power simplifies the consideration of focal size selection for two-photon excited fluorescence generation especially in imaging condition.

Another widely used condition for two-photon absorption measurement is the thin sample limit (or loose focusing limit, $z_R \geq l$) which can be obtained by loosely focused beam into the sample by amplified lasers (kHz) because of high pulse energy. Using a flat beam approximation, we can put $w(z) = w_z$ as a constant. The corresponding spatial distribution is given by

$$\int_V d\mathbf{r} S^2(\mathbf{r}) = \int_V d\mathbf{r} \left\{ \frac{w_0^2}{w_z^2} \text{Exp} \left[-\frac{2\mathbf{r}^2}{w_z^2} \right] \right\}^2 = 2\pi \Delta z \frac{w_0^4}{8w_z^2} \quad (1.17)$$

where Δz is the sample thickness. The time-averaged two-photon excited fluorescence photon flux for the thin sample limit is then

$$\langle F(t) \rangle = \frac{1}{2} \phi \eta \sigma_2 C \frac{g_p}{f \tau} \frac{\Delta z}{4w_z^2} \langle P(t) \rangle^2 \quad (1.18)$$

In this thin sample limit, the amount of two-photon excited fluorescence depends on sample thickness but is not dependent on sample position as long as beam size $[w(z)]$ is considered to be constant.

In theory, there is no complexity to estimate two-photon absorption both in thick and thin sample limits. In practice, however, experimental comparison between two cases can produce confusing result when each excitation and molecular conditions are not properly selected. I will discuss the complication of contributing factors to measure two-photon excited fluorescence by comparing molecules, excitation geometry, repetition of the laser, and detection geometry in more detail in Chapter 5.

1.4 Two-photon fluorophores

Since two-photon absorptivity and fluorescence quantum efficiency under photon excitation are directly related to the performance of TPM, there have been increasing demands to characterize TPA of chromophores and to develop better two-photon chromophores. For fluorophores, fluorescent chromophores, the most widely used technique to measure σ_2 is the two-photon excited fluorescence method developed by Xu and Webb et al.⁵ Fundamental approach is to excite fluorophore solution by a focused laser beam followed by collecting two-photon excited fluorescence into a sensitive detector at a 90°-angle geometry while rejecting excitation light.

One can measure two-photon absorption cross-section using eq (1.16) or eq (1.18) depending on excitation condition by careful measurements of temporal and spatial parameters of the incident laser beam and the characterization of sample conditions including the concentration, the fluorescence quantum yield, and the collection efficiency of the detection system. However this process is not trivial. When a well-characterized reference chromophore is available, TPA cross-section measurement

becomes much easier with minimal calibration by relative measurement. The relative fluorescence signal of a reference sample and an unknown sample by two-photon excitation for a specific wavelength is obtained under the assumption that the same excitation power are used is given as⁶

$$\frac{\langle F(t) \rangle_{ref}}{\langle F(t) \rangle_{smp}} = \frac{\phi_{ref} \eta_{ref} \sigma_{2,ref} C_{ref} n_{ref}}{\phi_{smp} \eta_{smp} \sigma_{2,smp} C_{smp} n_{smp}} \quad (1.19)$$

where ϕ is the fluorescence quantum yield, η the collection efficiency of the system, C is the concentration, n the refractive index of solvents, and *ref* and *smp* denote the reference and unknown samples, respectively. We can simply cancel out the temporal coherence factor $[g^{(2)}]$ for relative fluorescence signal because it is independent to samples. Rearrangement of eq (1.19) gives

$$\sigma_{2,smp} = \frac{\phi_{ref} \eta_{ref} \sigma_{2,ref} C_{ref} n_{ref} \langle F(t) \rangle_{smp}}{\phi_{smp} \eta_{smp} C_{smp} n_{smp} \langle F(t) \rangle_{ref}} \quad (1.20)$$

Thus one can easily measure TPA cross-section of a new sample without rigorous characterization for beam and detection system. Once fluorescence quantum yield, concentration of solutions, and solvent refractive index are known, TPA cross-section can be extracted by measuring fluorescence signal intensities of reference and unknown sample. The collection efficiency of the reference and the unknown sample can be assumed to be the same for simplicity when the reference and the unknown sample emit fluorescence in a similar spectral region. More careful calibration on collection efficiency can be done by measuring relative spectral collection efficiency which will be

described in Chapter 5. Practically, multiple fluorophores are available as a reference studied by several groups;⁵⁻⁷ Rhodamine6G (R6G) and Styryl9M are good reference fluorophores with modest signal [$\sigma_{2,\max}$ (R6G) = 65 GM at 800 nm, ϕ (R6G) = 0.92 in MeOH and $\sigma_{2,\max} \phi$ (Styryl9M) = 780 GM at 1240 nm, ϕ (Styryl9M) = 0.24 in CHCl₃] for λ_{ex} = 700–1000 nm and 900–1500 nm, respectively. The more relevant quantity for TPM is two-photon action cross-section, $\sigma_2 \phi$, which is the direct figure of merit to estimate how bright fluorophores is under two-photon excitation.

One requirement of this technique is to confirm the quadratic dependence of the fluorescence intensity versus the input laser power, otherwise direct comparison of the fluorescence intensity of reference to an unknown sample to calculate σ_2 is not valid. This method is directly applicable to obtain higher order absorption cross-section than two-photon absorption under the condition that power scaling confirms the corresponding order of process. Table 1 summarizes the σ_2 or $\sigma_2 \phi$ of some of commonly used two-photon chromophores measured by the two-photon excited fluorescence method.

**Table 1. Two-photon absorption cross-sections of commonly used fluorophores for λ_{ex}
= 700–1000 nm^a**

Fluorophores	Solvents	Excitation wavelength (nm)	σ_2 (GM)	$\sigma_2 \phi$ (GM) ^b
Intrinsic fluorophores				
NADH	H ₂ O, pH7.2	700	~0.02	
GFP wild type	H ₂ O	800	~6	
Retinol	H ₂ O, pH7.2	700		0.07
Flavins	H ₂ O, pH7.2	700-730		~0.1-0.8
Folic acid	H ₂ O, pH7.2	700-770		0.007
Extrinsic fluorophores				
Rhodamine 6G	MeOH	800	65 (± 9)	
Rhodamine B	MeOH	840	195 (± 25)	
Fluorescein	H ₂ O, pH11	780	46 (± 6)	
Coumarin 307	MeOH	776		19 (± 5.5)
Coumarin 485	MeOH	800	37	
Coumarin 540A	CCl ₄	800	45	
Lucifer Yellow	MeOH	840	2.9	
Tetraphenylporphyrin	CCl ₄	790	12	
Perylene	CH ₂ Cl ₂	820	4.5	
Fura-2 (free)	H ₂ O	700		11
Fura-2 (with Ca ²⁺)	H ₂ O	700		12
Cascade blue	H ₂ O	750		21 (± 0.6)
BODIPY	H ₂ O	920		17 (± 4.9)
Alexa Fluor 430	H ₂ O	870		11.6
Alexa Fluor 488	H ₂ O	720		97.9
Alexa Fluor 568	H ₂ O	760		157
Alexa Fluor 594	H ₂ O	780		99.8

(^a Collected from various sources: Xu et al. (1996)⁵, Kierdaszuk et al. (1996)⁸, Albota et al. (1998)⁶, Makarov et al. (2008)⁷, Muetze et al. (2012)⁹, and http://www.drbio.cornell.edu/cross_sections.html ^b Abbreviation : NADH, Nicotinamide adenine dinucleotide; GFP, Green fluorescent protein. Two-photon absorption cross-section of another set of fluorophores can be found in a review by Svoboda and Yasuda (2006)¹⁰ including calcium indicators, fluorescent proteins, and photo-switchable fluorescent proteins)

1.5 Basic components of a two-photon excited fluorescence microscope (TPM)

After experimental observation of nonlinear optical process it did not take long to realize the potential of nonlinear interaction for optical microscopy. The initial nonlinear optical microscopies was first demonstrated by SHG.¹¹ It was found that the interaction of light with the specimen is produced only at focal volume because the signal intensity scales nonlinearly with the intensity of light. The potency of nonlinear microscopy was not fully recognized until the first demonstration of laser scanning two-photon excited fluorescence microscopy developed by Denk and Webb et al.⁴

The basic component of TPM is depicted in Figure 1. Although linear and nonlinear fluorescence microscopes operate based on different orders of absorption process, they share common features for microscope assembly in their illumination source, scanning elements, collection and detection. The components described above also work for other type of nonlinear microscope based on different contrast mechanisms such as SHG, THG, three-photon absorption, and nonlinear phase modulation with minimal modification, which provides the possibility to build up multimodal microscopes.

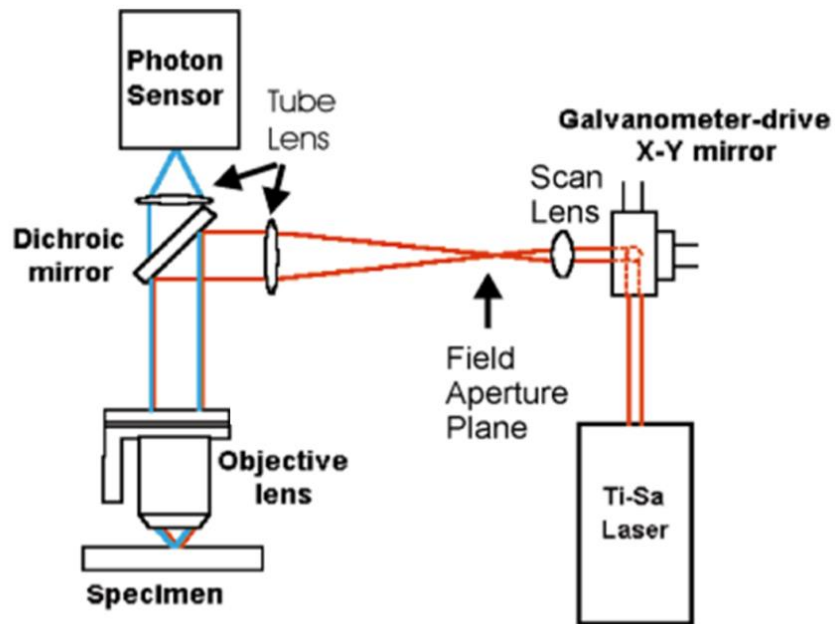


Figure 1. Schematic design of a typical two-photon microscope. Red lines indicate laser beam from Ti:Sapphire laser and blue lines indicate two-photon excited fluorescence. Adopted from So et al. (2000).¹²

A typical light source for TPM is high repetition rate (MHz) laser with fs- or ps-pulse width. Two-photon excitation require high intensity (photon flux), in turn, a pulsed laser is huge advantage, as shown in eq (1.16), to achieve efficiently high photon flux without depositing extreme light-dose that would cause photo-induced damage in biological samples. High repetition rate is also required to image large area in reasonable amount of time for single-point scanning excitation scheme. Typically, four or five orders of magnitude higher signal can be generated from 100-fs pulses with 80 MHz laser compared to CW laser under the same excitation power.⁵

The biggest difference between bright-field microscopy, the most basic microscope by white-light illumination, and TPM is that TPM utilizes the scanning

elements to scan specimen based on point excitation approach. The scanning elements include a scanning mirror, a scan lens, and a tube lens in which the scanning mirror rotates to change the beam position at the specimen (typically by raster scanning) and scan lens and tube lens combination provide beam propagation with proper collimation and collection.

The objective lens is critical component for TPM because it focuses the excitation laser beam into small area (~ femto liter) to generate high photon flux and localization of the signal source. The proper selection of the objective lens is important for desired applications. Multiple major properties are needed to be considered: NA (numerical aperture) that determines resolution and fluorescence gathering power, the magnification that determines the field of view, and working distance that determines the maximal depth of image.¹⁰ The wavelength of incident beam into the objective lens is also a determining factor for the lateral and axial resolution. Theoretical resolution of images is determined by diffraction limit, $R \approx \frac{\lambda}{2NA}$ where λ is the wavelength of the incident light. For example, a 40x/NA 0.75 objective lens with back-aperture filled by 800 nm laser beam provides ~530- μ m lateral resolution. Axial resolution is typically 2–3 times larger than lateral resolution.¹³

The most distinct difference between confocal fluorescence microscopy based on one-photon excited fluorescence and TPM, where both systems use laser as an excitation source and point-source scanning strategy, is detection scheme. In confocal microscopy, an iris is required to be placed before a detector to get rid of photons originated from

off-focus region and selectively collect photons from localized excitation volume that significantly reduces the collection efficiency of generated photons.¹⁴ The properly controlled size of the iris is to be typically less than about two Airy units, which is defined by the size of the point spread function of excitation beam at the focal plane. In contrast, TPM does not require an iris because two-photon excitation offers intrinsic optical sectioning capability provided by the fact that two-photon excited fluorescence is dominant only at focal area where high intensity is achieved. Detection in TPM typically is done with a photon multiplier tube (PMT) due to ultra-sensitivity of PMT for single photon detection.¹⁰

1.6 A new tissue imaging window (NIR-II) for TPM; an approach to enhance performance of TPM

There have been continuous efforts to improve and maximize the utility of TPM. At early stage of TPM for biological imaging, the most widely used light source was a Ti:Sapphire lasers that produce ~100-fs pulse with tunable wavelength range of 700–1000 nm.¹³ This wavelength range, called a biological imaging window or NIR-I, has been extensively utilized as excitation window because of reduced scattering and absorption from tissue than visible wavelength and simply accessibility from the laser source. Based on these advantages, the TPM technique with NIR-I excitation at 700–1000 nm has been applied to various tissue imaging allowing an understanding of structures and functions below several hundred microns depth.¹⁵⁻¹⁸ Typically a factor of two or three enhancement is obtained in imaging depth from NIR-I TPM when compared to traditional one-photon confocal microscopy.

While NIR-I imaging window is better than visible wavelength excitation range, longer wavelength over 1000 nm is potentially more beneficial but it has been relatively unexplored. With advent of laser technology, long NIR wavelength has become easily accessible opening up capability to utilize a new biological imaging window (NIR-II, 1000–1350 nm).¹⁹⁻²² This wavelength window is particularly useful because of multiple factors: (i) it enables deeper penetration depth than NIR-I due to less scattering (ii) it produces negligible autofluorescence because TPA of intrinsic chromophores in NIR-II window is negligible (iii) there is less absorption from biological elements (e.g. Hb, HbO₂, melanin) compared to NIR-I (iv) water absorption is still insignificant which becomes a limiting factor beyond 1400 nm. The absorption and scattering properties of several tissue components are compared in Figure 2.

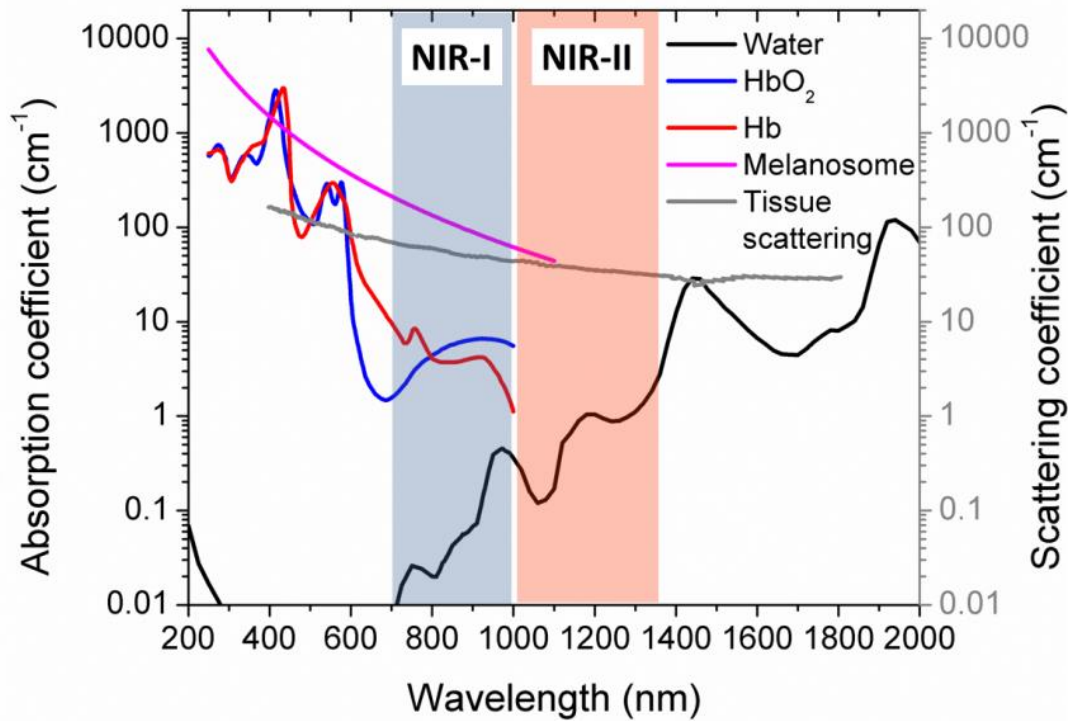


Figure 2. Absorption and scattering properties of typical biological components. Absorption properties were adopted from data set available in <http://omlc.ogi.edu>. Scattering property was adopted from T. Mattews's dissertation (2012).²³

Recently, Kobat et al. have shown that TPM is able to image a mouse's brain vasculature up to 1.6 mm using a 1280 nm pulsed laser excitation aided with a near-IR dye²⁴ (Figure 3) while imaging depth of typical TPM with 775 nm using MHz laser (nJ pulse energy) was limited $\sim 500 \mu\text{m}$ in mouse cortex.²¹ Even TPM using a Ti:Sapphire regenerative amplifier (μJ pulse energy) with 800 nm excitation applied to enhance imaging depth has been limited to ~ 1 mm for living mouse brain which corresponds to the theoretical depth limit of 800 nm excitation.²⁵ In addition, the superior penetration depths of longer excitation wavelength have been reported in several phantom tissue

models²⁶, ex vivo, and in vivo tissues.²⁷⁻²⁸ The greatly enhanced imaging depth of up to ~1.6 mm over early TPM studies using NIR-I wavelength excitation could be achieved via two critical factors: (i) NIR-II wavelength excitation (e.g. 1280 nm) and (ii) an exogenous two-photon NIR fluorophore (Alexa680-dextran).

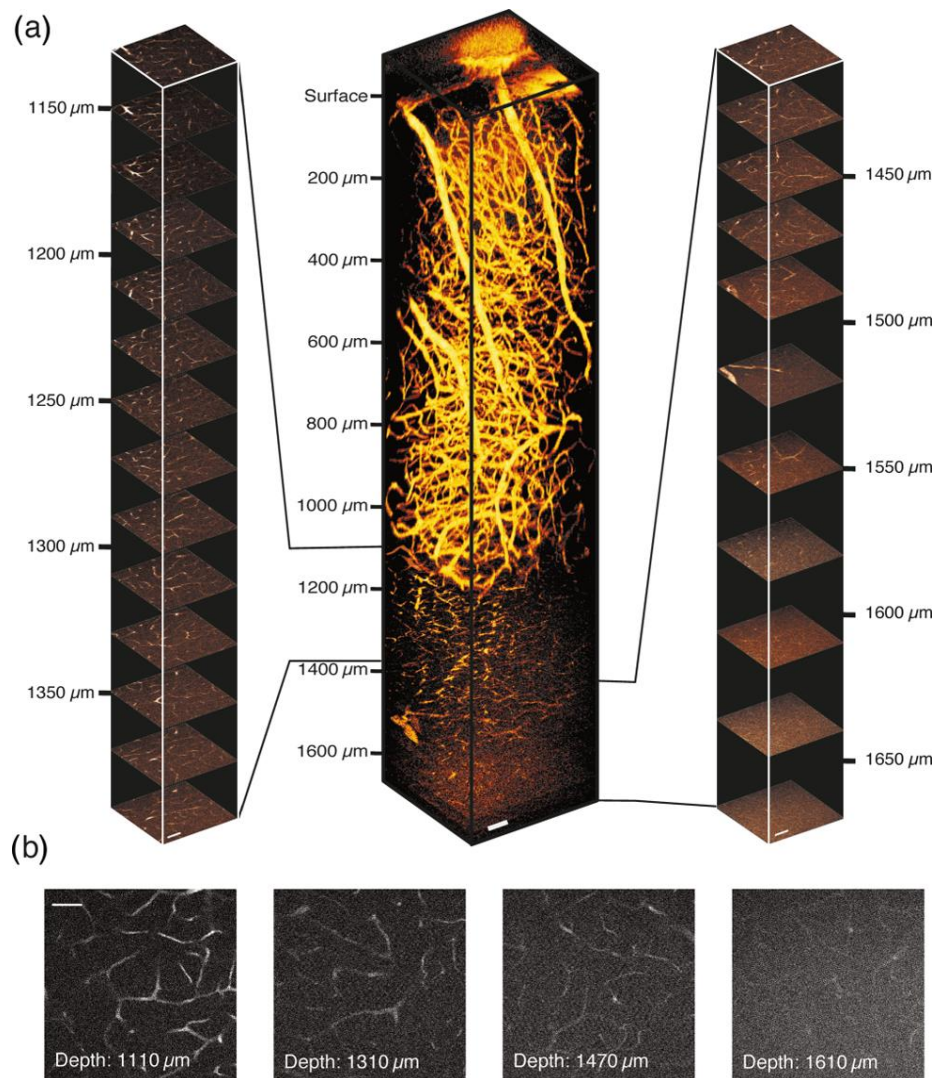


Figure 3. Two photon fluorescence images of cortical vasculature in a mouse brain. (a) Reconstructed z-stack images for 3D and (b) four individual images beyond 1 mm depth with scale bars of 50 μm for both (a) and (b). Adopted from Kobat et al. (2011).²⁴

NIR-II wavelength is, thus, a promising biological imaging window for TPM with the combination of a fluorophore possessing high two-photon action cross-section. However, good TPA fluorophores for NIR-II wavelength window are limited. Intrinsic fluorescent markers typically have negligible two-photon action cross-section beyond 1000 nm.²⁹ They show low two-photon action cross sections at NIR-I [e.g. $\sigma_2\phi$ (NADH) = $\sim 10^{-3}$ GM at 800 nm] and even smaller at NIR-II that requires excitation power of about a hundred milliwatts (Ti:Sapphire laser) to generate reasonable two-photon fluorescence signal. Rhodamine6G, one of the gold standard among exogenous fluorophores, show $\sigma_2 = 65$ GM at 800 nm but its σ_2 rapidly decrease beyond 900 nm ($\sigma_2 < 10$ GM at 900–1000 nm).⁷ Alexa Fluor and Cy dyes are relatively good TPA fluorophores in NIR-II wavelength [$\sigma_2\phi$ (Alexa680) = 75 GM at 1280 nm and $\sigma_2\phi$ (Cy5.5) = 60 GM at 1280 nm].²¹ However, when compared to quantum dots, size-controllable inorganic nanoparticles typically varying from a few nm to a few tens of nm, Alexa and Cy dyes are not promising. Larson et al. claimed that water soluble quantum dots ($\sim 4-5$ nm in diameter) display remarkable two-photon action cross-section of up to 48000 GM at $\lambda_{ex} = 700-1000$ nm³⁰ which is 3-4 orders of magnitude higher than those of organic chromophores listed in Table 1. However quantum dots' composition, such as CdSe, is still debated for its safety concern for biological use. Currently available fluorescent materials for the NIR-II tissue imaging window do not satisfy (i) large two-photon action cross-section ($\sigma_2\phi$) and (ii) safety for biological use. Thus, good TPA chromophores providing high brightness

under NIR-II excitation and biocompatibility to facilitate the maximal efficacy of TPM toward a deeper, faster, and safer tissue imaging are in great need.

1.7 Dissertation goals and outline

As stated in the beginning of this chapter, the main goal of this dissertation work is the investigation of two-photon excited fluorescence of highly conjugated porphyrin arrays in NIR-II excitation window and the utilization of biocompatible nanoscale emissive polymersomes that disperse these highly conjugated porphyrin arrays and possess unprecedented brightness under two-photon excitation which is potentially an ideal multimodal imaging agent for various biological applications. In addition to the spectroscopic interrogation of the two-photon excited fluorescence of the highly conjugated porphyrin arrays dispersed in organic solvents and in polymersomes, the effect of laser condition on two-photon excited fluorescence measurement has been explored. It was found that confounding linear fluorescence can be generated during two-photon absorption cross-section measurements when employed high repetition rate lasers. A pulse train shaping technique that separates pure nonlinear processes from linear background fluorescence is demonstrated as a solution.

The following sections provide short summaries of each chapter in the rest of the dissertation:

Chapter 2. (Introduction to Highly Conjugated Porphyrin Arrays and Polymersomes) – This chapter will provide a brief overview about porphyrins and

polymerosomes which are the main target materials. Fundamental optical and chemical properties of highly conjugated porphyrins and polymerosomes will be briefly discussed.

Chapter 3. (Exceptionally Large Two-Photon Absorption Cross-section of Highly Conjugated Multiporphyrins under NIR-II Wavelength Excitation) – This chapter explores the two-photon absorption of *meso*-to-*meso* ethyne-bridged (porphinato)zinc(II) oligomers (**PZn_n**) at NIR-II wavelengths. Monomeric porphyrins, **Zn(II)TPP** and bisethynyl (porphinato)zinc(II) monomer, were also investigated as benchmark fluorophores. Exceptionally large TPA cross-sections up to 76,000 GM (**PZn₅**) were observed in the NIR-II wavelength window with multiple peaks. Also it was found that two-photon transition energy is insensitive to the molecular length in **PZn_n** which is contrast to the progressively red-shifted one-photon S₁ transitions as the conjugation length increases. The collaboration with Dr. Rawson who was a former graduate student in the Therien lab revealed the origin of two-photon absorption of **PZn_n** at NIR-II wavelengths from a simple molecular orbital concept based on DFT (density functional theory) calculation. This work not only suggests **PZn_n** are promising two-photon fluorophores in the NIR-II wavelength window but also provides an insight for design motif to develop good two-photon chromophores based on macrocyclic systems as a building block. The work in this chapter has been done as collaborative effort with Dr. Jeff Rawson who performed DFT calculations and Dr. Kimihiro Susumu who synthesized the studied porphyrins.

Chapter 4. (Nano-vesicular Two-photon in vivo Imaging Agent with Super-Brightness for NIR-II Wavelength Excitation) – Chapter 4, as a continuing work from the previous chapter, explores one-photon and two-photon absorption of *meso-to-meso* ethynyl bridged multiporphyrin-incorporated polyemersomes, which are NIR-emissive polymersomes. I found that the large TPA cross-sections of **PZn_n** remain in the polymer matrix resulting in TPA cross-section >10⁷ GM per nano-object providing unprecedented brightness at NIR-II wavelengths. Also I demonstrate two-photon in vivo imaging to visualize blood vasculature of mice using dorsal window chamber model via NIR-emissive polymersome injection. Tumor (4T1) detection utilizing the NIR-emissive polymersomes under 1100 nm two-photon excitation in using dorsal window chamber models was performed. Importantly, nanoscale polymersomes can afford the chemical stability, drug delivery capacity, and biocompatibility necessary for developing these structures as impressive diagnostic and therapeutic agents. It is expected that this multimodal diagnostic and therapeutic agent with unprecedented two-photon brightness based on the porphyrin-incorporated polymersomes will significantly contribute to on-going efforts in biomedical applications. The work in this chapter has been done as collaborative effort with Dr. Melanie C. O'Sullivan who provided nano-sized emissive polymersomes, Dr. Simone Dagan who prepared mice and histology slides, Dr. Jesse W. Wilson who performed image analysis, Yusong Bai, Ruobing Wang and Dr. Jeff Rawson who provided ethyne-bridged multiporphyrins.

Chapter 5. (Femtosecond Pulse Train Shaping Improves Two-photon Excited Fluorescence Measurements) – Chapter 5 explores the effect of laser condition on TPA cross-section measurement and a pulse shaping technique to single out pure two-photon process out of linear background signal. Measurements of TPA cross-sections are greatly confounded by even very weak linear absorption, for example from hot bands. In this case, the experimental power dependence of fluorescence from amplified and mode-locked laser systems can differ drastically, even if the peak intensity is adjusted to be the same in both cases. A simple pulse train shaping method suppresses linear contributions and extracts the nonlinear absorption cross section, demonstrated here for *meso-to-meso* ethyne-bridged bis[(porphinato)zinc(II)] fluorophores at 800 nm. This approach permits reliable TPA cross-section measurement, even with standard modelocked lasers under conditions identical to that used for multiphoton microscopy. This chapter has been published as: Park, J. K.; Fischer, M. C.; Susumu, K.; Therien, M. J.; Warren, W. S., *Opt. Lett.* **2014**, 39 (19), 5606-5609.

Chapter 6. (Two-photon Absorption of Various NIR Emissive Porphyrin Arrays under NIR-II Wavelength Excitation) – Porphyrin oligomers with *meso-to-meso* connectivity have shown distinctive features depending on spacers' length, steric hindrance and perturbed electronic properties induced by auxiliary groups. In this chapter, two-photon absorption of various types of multiporphyrin compounds, which exhibit high fluorescence quantum yields in NIR regions, at NIR-II wavelengths are investigated. The various porphyrin oligomers include donor-acceptor type ethyne-

bridged multiporphyrins, and benzothiadiazole (BTD)-conjugated multiporphyrins. These series of compounds possess strong TPA in the NIR-II wavelength window confirming the facts that the connection of porphyrins via effective π -conjugated bridges makes them potent two-photon absorbers. Especially, it was found that BTD-conjugated porphyrin arrays are promising for wavelength selection from $\lambda_{\text{ex}} = 1050$ nm to 1210 nm while **PZn_n** are optimal for 1030–1100 nm excitation. The work in this chapter has been done as collaborative effort with Dr. Kimihiro Susumu who provided donor-acceptor type ethyne-bridged multiporphyrins, Dr. Jeff Rawson who provided ethyne-bridged porphyrin heptamer, Dr. Wei Qi who provided BTD-conjugated multiporphyrins, and Sean Rodget who assisted TPA cross-section measurements.

2. Introduction to Highly Conjugated Porphyrin Arrays and Polymersomes

This chapter will provide a brief overview about porphyrins and polymersomes, which will be presented in the rest of this dissertation, to help understand their fundamental properties and terminologies.

2.1 Porphyrin

Porphyrin, a naturally occurring macrocyclic chromophore made of four pyrroles linked by four methane bridges, is one of the most important natural pigments (Figure 4). Chlorophyll and heme are the most well-known porphyrins operating in nature.³¹ Chlorophylls take part in photosynthesis, converting sun light into chemical energy in plants. Heme is a cofactor in red blood cells, involved in oxygen transport in the blood of vertebrates. Depending on environment and variation in structure, the roles of porphyrin and its derivatives range from light harvesting(chlorophyll), oxygen transport(heme), oxygen storage (hemoglobin and myoglobin) to electron transport (paeophyrin) and metabolism (siroheme).³¹ Inspired by nature, people have tried to utilize porphyrins and their derivatives in various research directions toward biomedical applications and the material science field.³²⁻³⁵ Porphyrins and porphyrin derivatives are popular materials due to their photochemical stability, biocompatibility, large extinction coefficient [ϵ (molar extinction coefficient) $\sim 10^5 \text{ M}^{-1}\text{cm}^{-1}$] in the visible wavelength region, and versatility as a building block for complex multidimensional

nanomaterials. Also, the metal binding pocket of the center of porphyrin systems provides a variety of functionality.

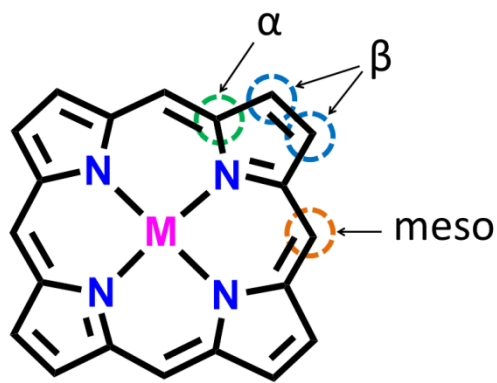


Figure 4. Structure of porphyrin with the α -, β -, and *meso*-positions indicated. *M* in the center of the porphyrin ring represents metals (or H_2 for free-base porphyrin) that can be coordinated by binding with four nitrogens.

One promising application is porphyrin-based photo electrochemical cells with porphyrins as a sensitizer in a light-harvesting compartment, because they possess a large extinction coefficient in the UV-vis wavelength region, chemical stability, and handy control of redox potentials to match energy levels with nanocrystalline metal oxides as anode materials.³² Porphyrins can be easily modified at their β - and *meso*-positions and metal binding site, as well. Various types of porphyrins were developed toward higher power conversion efficiency. A class of porphyrins with high power conversion efficiency include β -functionalized zinc porphyrins with a diarylamino group³⁶, and *meso*-functionalized zinc porphyrins with a diarylamino group³⁷⁻³⁸.

Porphyrins and their derivatives have been extensively studied in the field of medical imaging and photodynamic/photothermal therapy.^{35, 39} Even without

sophisticated imaging tools, the red color of heme in blood has been used as a diagnosis of hemorrhage for a long time. More sophisticated imaging tools were used to visualize specific regions of interest from optical, magnetic and thermal responses of porphyrin derivatives. Porphyrin derivatives have also been utilized in photodynamic therapy⁴⁰, a therapeutic technique based on cytotoxic singlet oxygen generation under light exposure with the aid of a photosensitizer. Multiple compounds (e.g. PhotofrinTM and VisudyneTM) that are based on the porphyrin structure have been approved by the FDA for photodynamic therapy.⁴⁰⁻⁴¹

Since extensive applications using porphyrins are based on its electronic absorption and its dynamics upon light excitation, it is crucial to understand porphyrins' absorptive characteristics. The electronic absorption of porphyrin [for example, tetraphenylporphyrin, H₂(TPP)], is composed of a strong single S₂ transition (also called B- or Soret-band) at ~ 400 nm and a quasi-allowed S₁ transition (denoted Q-band) with multiple vibronic structures at 500-650 nm (Figure 5). This basic absorptive property is dependent on the binding of various metals by coordination at the four nitrogens in the center of the macrocyclic ring and variations on the pyrrole rings.

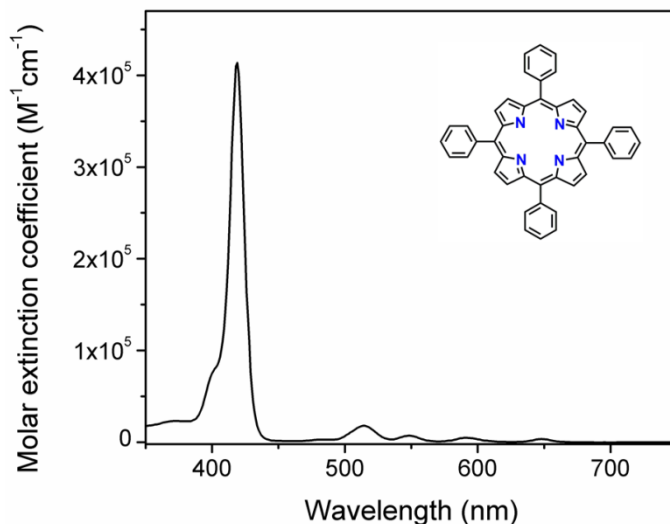


Figure 5. Linear absorption spectrum and its molecular structure of Tetraphenylporphyrin [H₂(TPP)] in CCl₄.

The four-orbital model, developed by Gouterman in the 1960s, describes the UV-vis absorption of porphyrinoids based on simple molecular orbital theory without complex quantum mechanical calculations.⁴²⁻⁴⁴ Briefly, since porphyrin is a π -conjugated macrocyclic chromophore, π -electrons are responsible for its UV-vis absorption. According to Gouterman's model, the energy and properties of four orbitals, two highest-occupied molecular orbitals (HOMO; a_{1u} and a_{2u}) and two lowest-unoccupied molecular orbitals (LUMO; degenerate e_g), determines the transition energies and strength in their UV-visible absorption. For the fundamental porphyrin molecule, two possible states, fully allowed S_2 and forbidden S_1 transition, arise from four possible transitions between two HOMOs to two LUMOs. Under the assumption that two HOMOs are degenerate, high energy transition ($2E_u$) is fully allowed and low energy transition ($1E_u$) is forbidden. Any deviation from degeneracy of two HOMOs generate a

low energy transition that is allowed, and the degree of energy difference between two HOMOs directly correlate with the strength of low energy transitions which explains the experimental absorption spectrum of typical porphyrins; a strong Soret band and a weak Q-band.

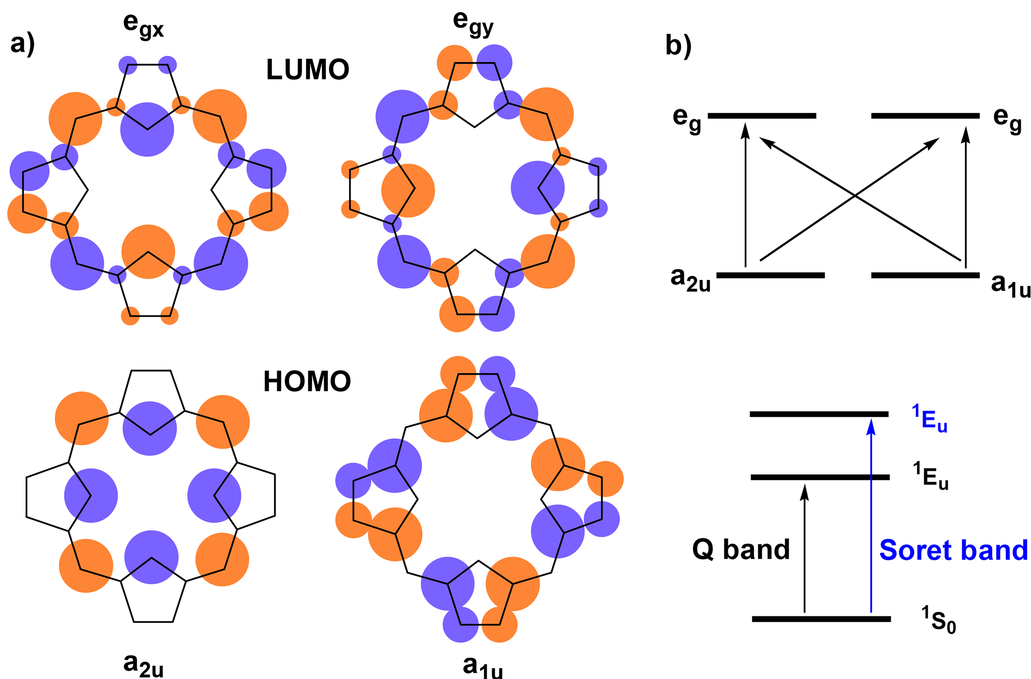


Figure 6. (A) Representative highest occupied molecular orbitals (HOMO) and lowest unoccupied molecular orbitals (LUMO) of porphyrin. Blue and red colors represent the phase of electronic wavefunctions and the size represents the magnitude of probability of electronic distribution. (B) (top) Corresponding HOMO and LUMO diagram with possible transitions from HOMOs to LUMOs depicted by arrows. (bottom) Origin of two main optical transitions (Soret and Q) of porphyrins with corresponding symmetry. Adopted from Senge et al. (2014).⁴⁵

Also this model explains the absorption trends found in other types of four-pyrrole pigments using a similar pattern; chlorin and bacteriochlorin display strongly allowed S_1 bands due to broken degeneracy of a_{1u} and a_{2u} and their transition shift to low

energy as more pyrrole rings are reduced. We will get back to this model to explain the linear and nonlinear absorption of highly conjugated ethyne-bridged multiporphyrins which is the main interest in Chapter 3 of this dissertation.

2.2 Highly-conjugated ethyne-bridged porphyrin arrays

Beyond monomeric porphyrin there have been tremendous efforts to explore multimeric porphyrins by many research groups to generate novel optical and electrochemical properties. Multimeric porphyrin can be mainly divided into two categories (i) linearly conjugated multimeric arrays connected by bridges and (ii) multi-dimensional structures either by self-assembly or cyclic conjugation. Although multi-dimensional porphyrin structures are an important research direction⁴⁶, it is beyond of the scope of this dissertation.

Linking porphyrin units can alter the electronic properties significantly when two moieties are in close proximity or conjugated by efficient π -bridges. While multiple linearly conjugated porphyrin systems have been developed³³, *meso-to-meso* ethyne-bridged porphyrins stand out as a result of their unique molecular properties due to ethyne connectivity achieving the maximal π -conjugation among porphyrins without severely disturbing π -delocalization in individual porphyrin units.⁴⁷⁻⁵²

Meso-to-meso ethyne-bridged (porphinato)zinc(II) oligomers (**PZn_n**) are featured by (i) broad S₂ band [full-width half maximum (FWHM) = ~3500–5000 cm⁻¹] originating from exciton coupling between monomeric porphyrin units (ii) fully allowed S₁ transition (Q-derived) that shifts to lower energy as molecular length increases (694

nm - 842 nm) (iii) near-IR (NIR) fluorescence with high fluorescence quantum yield ($\phi = 14-22\%$) (iv) strong $S_1 \rightarrow S_n$ transition tunable over a wide 850-1400 nm spectral window.⁴⁷ Note that **PZn_n** exhibits high fluorescence quantum yields over 10% in NIR. It is known that materials with a narrower energy gap (HOMO-LUMO) displays lower quantum yields due to enhanced non-radiative decay rate which is called the energy gap law.⁵³ Porphyrin arrays, however, do not follow the trends [ϕ (**PZn₂**) = 16%, ϕ (**PZn₃**) = 22%, and ϕ (**PZn₃**) = 14%]. Fluorescence lifetime and femto-second (fs) transient absorption studies revealed it is partially caused by the reduced intersystem crossing rate to a triplet state to compensate for the enhanced non-radiative decay rate as the conjugation length increase in **PZn_n** system.⁴⁷

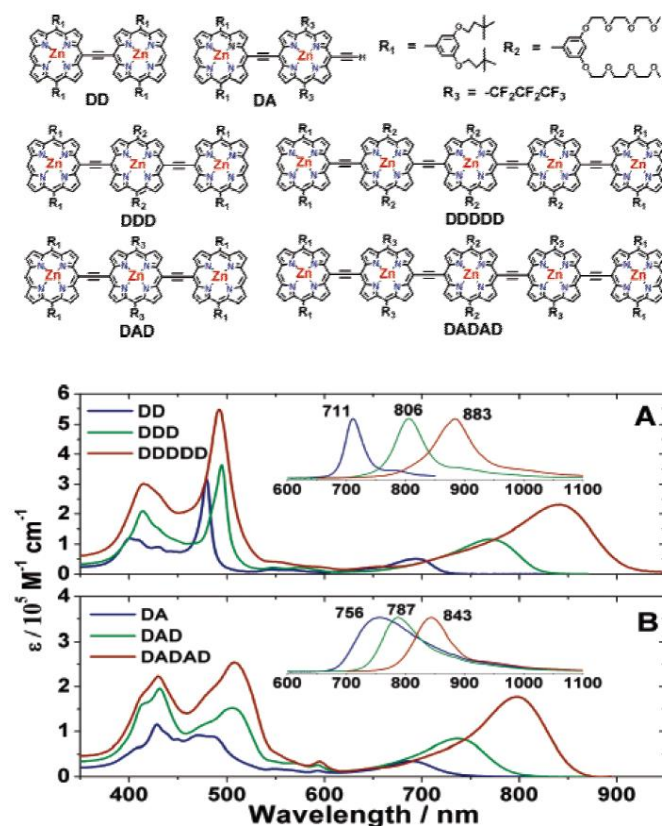


Figure 7. Molecular structure of *meso-to-meso* ethyne-bridged (porphinato)zinc(II) oligomers and their linear absorption spectra in THF. Inset shows the emission spectra of porphyrin arrays. Adopted from Duncan et al. (2006).⁴⁷

While the fundamental idea of Gouterman's four orbital model holds in most multimeric porphyrins, the additional key concepts to understand the electronic absorption characteristics of *meso-to-meso* ethyne-bridged porphyrins are (i) exciton coupling, the communication of (transition) dipole moment between porphyrin and neighboring porphyrin, in which significant contribution made by M. Kasha, and (ii) π -electron conjugation. Based on a resonance dipole-dipole interaction mechanism in weakly coupled electronic system, the exciton model⁵⁴ predicts spectral shifts and splitting of absorptive characteristics of molecular composites based on interaction of

dipole moments between individual moiety; one dipole in along the long-axis of the molecule and the other is orthogonal to the long-axis dipole moment. These can interact with two dipole moments in another moiety. For porphyrin dimers, the same model can be extended to explain the splitting of Soret-transitions. Parallel excitons (two dipoles in each porphyrin moiety facing side-by-side) give rise to high energy B_y -transitions and in-line (or head-to-tail) excitons give rise to low energy B_x -transitions. Accounting for free rotation of porphyrin along the long molecular axis of the dimer, the B_y -transition can be broadened depending on the dihedral angle between the planes of macrocyclic rings. However, the simple exciton coupling model fails to explain quantitatively the B -transitions of porphyrin dimers because electronic conjugation through an ethyne bridge is strong. The assumption that each porphyrin unit is a separate moiety is not valid any longer in ethyne-bridged porphyrins.

In *meso*-to-*meso* ethyne-bridged bis(porphinato)zinc(II), **PZn₂**, a Q-derived transition is strongly allowed in contrast to monomeric porphyrin due to orbital degeneracy which is a requirement for the forbidden transition to no longer hold. Instead, ethyne bridged porphyrins display single fully allowed [ϵ (**PZn₂**) = 51,400 M⁻¹cm⁻¹, ϵ (**PZn₃**) = 116,000 M⁻¹cm⁻¹, ϵ (**PZn₂**) = 230,000 M⁻¹cm⁻¹; THF] Q-derived transitions. Also, the shift of the lowest transition [λ_{\max} (**PZn₂**) = 694 nm; λ_{\max} (**PZn₃**) = 770 nm; λ_{\max} (**PZn₅**) = 842 nm, in THF] follows a Particle-in-a-box model – energy gap decreases as box length (or molecular length) increases – simply governed by π -conjugation through the entire molecule.

2.3 Polymersome is a soft vesicle

Since their first demonstration⁵⁵, polymersomes, artificial vesicles made of di-block copolymers, have become intriguing nano vesicular systems. A di-block copolymer where one part of the polymer is hydrophilic and another part of the polymer is hydrophobic is the key ingredient in preparing polymersomes. When they are dissolved in water they can form a vesicle structure under specific amphiphilic proportions. To form a vesicle structure in water, the general requirement is that the ratio (f) of hydrophilic part to total polymer mass should be 25-40%. Otherwise the polymer can be inverted to microstructures ($f < 25%$) or micelles ($f > \sim 50%$) in water.⁵⁶

Polymersomes have shown promising biomaterial properties, including (i) multimodal delivery for hydrophilic compounds (such as a drug molecule) in their hydrophilic hollow part or hydrophobic compounds (such as a fluorescent marker) in the hydrophobic inter-layer, (ii) controllable vesicle and layer size by modifying the length of diblock copolymers, (iii) augmented chemical and physical stability compared to those of liposomes comprised of natural phospholipids, and (iv) prolonged blood circulation time compared to liposomes.⁵⁶⁻⁵⁷

The most important advantage of polymersomes over liposomes, vesicles comprised of phospholipids derived from nature, for the main focus of this dissertation (in vivo imaging application) is the controllable thickness of bilayer membranes to contain large amounts of contrast agents. Lipid membranes provide limited space with thickness ranges of $d = 3\text{--}5$ nm. In contrast, polymersomes with average size of 100–200

nm (with MW of 2000–20000 Da) display the thickness ranges of $d = 8\text{--}21$ nm which provide sufficient space to contain various hydrophobic chromophores in the bilayer membrane⁵⁶; for example **PZn₅** (molecular length, $l = 5.4$ nm) can be contained in the bilayer membrane of polymersomes made of PEO₃₀-b-PBD₄₈ but not in liposomes. Accordingly, polymersomes are promising nano-size platforms that can carry and deliver various materials (hydrophilic drug molecules or hydrophobic fluorescent contrast agents) to specific target regions that can be equipped with further functionalization.

2.4 NIR-emissive polymersome

Despite the promising electro-optical properties of *meso*-to-*meso* ethyne-bridged (porphinato)zinc(II) oligomers, it requires enormous labor to make it water soluble for in vivo application. Also, polymersomes require fluorophores to make them optically active because polymersomes themselves are not emissive in the visible wavelength region. The Therien group developed the first NIR-emissive polymersome designed for in vivo imaging by incorporating **PZn_n** in polyethylene-block-polybutadiene (PEO₃₀-b-PBD₄₈) copolymer in 2005 (Figure 5).⁵⁸ The combination of two promising moieties, porphyrin arrays and polymersomes, engendered a NIR-emissive nano vesicle for diagnostic optical imaging.⁵⁸⁻⁵⁹ Confocal fluorescence imaging of micron sized NIR-emissive polymersomes indicates membrane specific accumulation of NIR fluorophores (NIRF) without the leaking of chromophores out of the vesicle. Also the strong absorption and emission property of NIRF still remains in PEO₃₀-PBD₄₈ similar to those

extensively explored in organic solvent, implying well-dispersed NIRFs in the polymer matrix. It is noteworthy to mention that SOPC (1-stearoyl-2-oleoyl-sn-Glycero-3-Phospho-choline) liposomes were not able to contain NIRFs (PZn_2 - PZn_5 ; molecular length = 2.1–5.4 nm) at even 500:1 molar ratios of lipid:NIRF because of thin membrane thickness. In contrast, polymersome could incorporate NIRFs up to 10:1 molar ratios of polymer:NIRF (10 mol%) which demonstrate the superiority of polymersomes over liposomes for further utility.

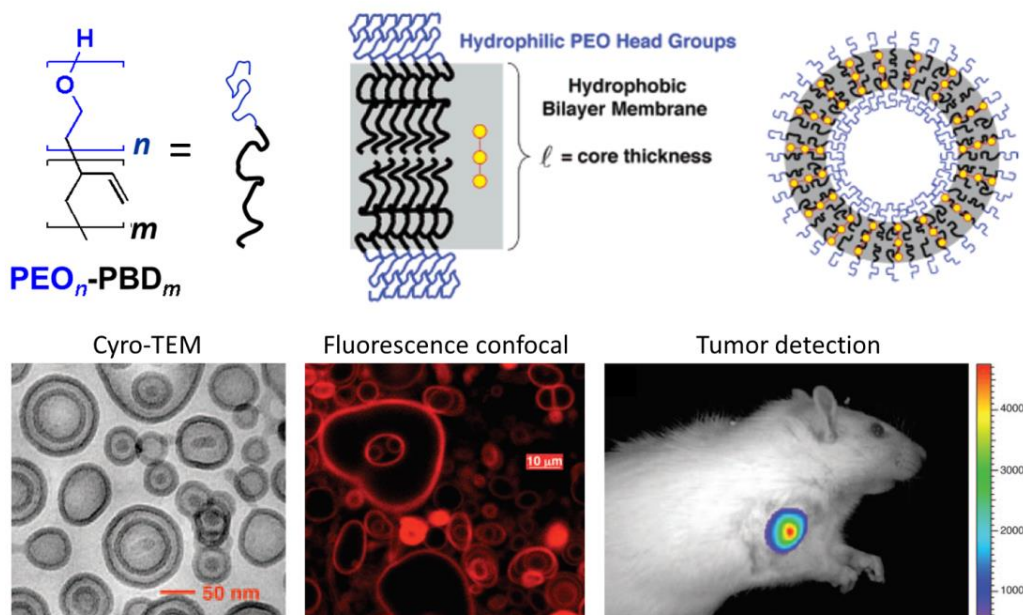


Figure 8. (Top) Schematic description of the formation of emissive polymersomes in aqueous medium. (Bottom) Imaged nano-sized and micron-sized polymersomes by cryo-TEM and by conventional confocal fluorescence microscope, respectively. Imaging of tumor mouse model was demonstrated by PZn_3 -dispersed polymersomes that visualize tumor region imaged by a whole animal fluorescence imager. Adopted from Ghoroghchian et al. (2005 and 2007).^{58,60}

One nano-sized vesicle can contain thousands of emitter copies (for example, a 100-nm diameter vesicle with 5 mol% fluorophore loading contains 2500 copies of NIRF

in their hydrophobic bilayer membrane). Accordingly, one particle of emissive polymersomes is estimated to possess an extinction coefficient up to $\sim 10^9 \text{ M}^{-1}\text{cm}^{-1}$. In addition, NIR-emissive polymersomes demonstrated high photobleaching thresholds ($>500 \text{ mW/cm}^2$) and strong chemical stability in physiological environments over one week. As a proof-of principle these NIR-emissive polymersomes were injected into a tumor model mouse, and the tumor region was visualized by a whole animal imager with strong fluorescence signal [Signal-to-Noise ratio (SNR) $> \sim 10$]. Taken together, NIR-emissive polymersomes, highly conjugated porphyrin array loaded artificial vesicles, demonstrated unique and superior chemical and optical properties for in vivo imaging agents. Further efforts also demonstrated to utilize NIR-emissive polymersomes to be targeted and delivery modality.^{57, 61-62} Therefore, NIR-emissive polymersomes are intriguing multifunctional delivery vehicles for therapeutic pharmaceuticals and contrast imaging agents for various biomedical applications.⁵⁷

My dissertation work is focused on exploring the utility of NIR-emissive polymersomes for two-photon excited fluorescence imaging agents beyond conventional imaging modality based on one-photon excitation.

3. Exceptionally Large Two-Photon Absorption Cross-section of Highly Conjugated Multiporphyrins under NIR-II Wavelength Excitation

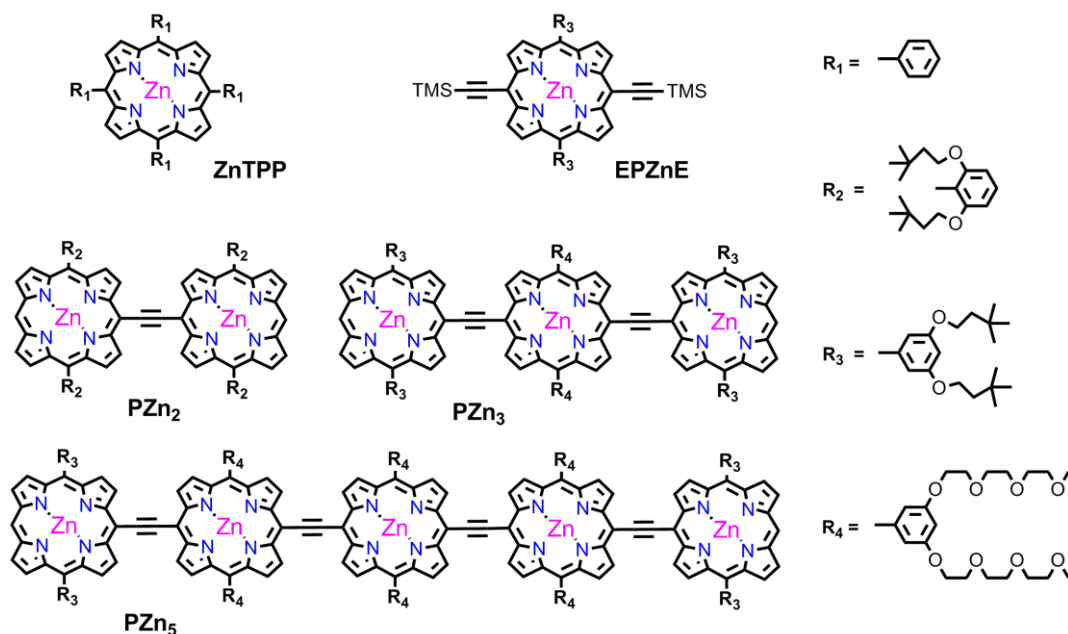
3.1 Introduction

Since its invention, two-photon excited fluorescence microscopy (TPM) has become a standard imaging technique, providing profound structural and functional insights into specimens with subcellular-resolution imaging.^{3-4, 12, 30, 63} For maximum utilization of multiphoton imaging toward deeper imaging depths, near-IR (NIR) emitting materials of superior brightness and long wavelengths (>1000 nm) of two-photon excitation beyond the conventional NIR imaging window (700–1000 nm, NIR-I) are required.⁶⁴⁻⁶⁶ Especially, the excitation imaging window of 1000–1350 nm (NIR-II) is of particular importance for *in vivo* imaging since scattering and absorption from tissue are much lower than in the conventional imaging window,²² but the water absorption that hampers the utility of longer wavelengths becomes significant beyond ~1400 nm. Exploitation of this promising tissue imaging window using multi-photon microscopy offers benefits that include better contrast, deeper penetration depth, and enhanced biological specimen viability.^{19, 22, 67} Recently, Kobat et al. demonstrated an imaging depth of 1.6 mm showing clear cortical vasculature structure in mouse brain.^{21, 24} These greatly enhanced imaging depths over the limit of early stage TPM could be achieved via two critical factors: NIR-II laser excitation at 1280 nm, and an exogenous two-photon NIR dye, Alexa680-Dextran.

Endogenous markers used for multiphoton imaging display small two-photon absorption (TPA) cross-sections: many endogenous markers such as reduced nicotinamide-adenine dinucleotide (NADH) and Riboflavin have σ_2 (TPA cross-section) < 1 GM [GM (Goeppert-Mayer, $1 \text{ GM} = 1 \times 10^{-50} \text{ cm}^4 \text{ s photon}^{-1}$)] at 700–1000 nm and are expected to be much smaller than 1 GM beyond 1000 nm.^{13, 68} Conventional extrinsic fluorophores such as rhodamine6G and fluorescein, which are considered to be gold standards for two-photon excitation, exhibit ~ 100 GM at excitation wavelengths that range over 700–1000 nm, but are not promising ($\sigma_2 < 10$ GM) at 1000–1350 nm.^{5, 7} The further advancement of TPM techniques is thus impeded by a dearth of appropriate fluorophores that possess significant TPA cross-sections at long wavelengths (NIR-II). There are several fundamental requirements that should be fulfilled by ideal two-photon imaging agents: (i) large two-photon absorption cross-section in NIR wavelength, (ii) high quantum yield fluorescence in NIR, and (iii) photostability and biocompatibility. Meeting these conditions is challenging, and very few chromophores can be used safely for TPM that possess large TPA cross-sections under λ_{ex} at 1000–1350 nm; indocyanine green (ICG) is one of the few safe markers useful for two-photon imaging having a measured TPA cross-section (σ_2) of ~ 500 GM at $\lambda_{\text{ex}} = 1550$ nm but not well characterized in the NIR-II imaging window.⁶⁹

While pristine monomeric porphyrins have received little attention for TPA application due to small TPA cross-section,^{7, 70-71} it was found that polarizable monomeric porphyrins and highly conjugated multimeric porphyrinoids display large

TPA cross-section; prior works have identified sizeable TPA cross sections in push-pull extended monomeric porphyrins⁷²⁻⁷⁴, porphyrin dimers bridged by ethyne, butadiyne, diethynylanthracene, and other π -conjugated linkers, and porphyrin multimers beyond dimers.⁷⁵⁻⁸¹ Among many, highly conjugated porphyrin arrays with *meso-to-meso* connectivity have displayed large TPA absorptivity ($\sim 10^2 - 10^4$ GM)^{75-76, 81}. The high TPA cross-sections reported for the porphyrin arrays have been explained using a three-state model, in which the intense x-polarized Q-derived states mediate TPA that is enhanced by resonance with Soret-manifold states.⁷⁵⁻⁷⁶ However, the TPA demonstrated for most porphyrin derivatives has employed photon energies that lie within the conventional imaging window (700–1000nm). In addition, highly conjugated *meso-to-meso* ethyne-bridged (porphinato)zinc(II) oligomers (**PZn_n** compounds, Scheme 1) which manifest strong coupling between monomeric porphyrins, with globally delocalized ground and excited states that give rise to high NIR absorptivities [$\lambda_{\text{abs,max}} = 695\text{--}840$ nm, ϵ (molar extinction coefficient) $> 10^5$ M⁻¹cm⁻¹] and high fluorescence quantum yields of 14–22% in NIR,^{47-52, 58-59, 82-86} have not been systematically studied for their two-photon absorption.



Scheme 1. Molecular structures of studied porphyrinoids

Here we report an experimental and theoretical study on two-photon absorption of highly conjugated *meso*-to-*meso* ethyne-bridged (porphinato)zinc(II) oligomers (**PZn_n** compounds) focused on the NIR-II wavelength region. We found highly emissive **PZn_n** manifest exceptionally large two-photon absorption cross-sections found in NIR-II region (λ_{ex} : 1000 – 1350 nm), up to $\sigma_2 \sim 76000$ GM of **PZn₅**, which is three orders of magnitude higher than conventional two-photon dyes such as rhodamine 6G ($\sigma_2 = 65$ GM at λ_{ex} : 800 nm).^{7,30} TDDFT calculations that exploit the M11 range-separated hybrid functional reproduce the low-energy Q-transitions of **PZn_n** compounds to within ~ 0.1 eV and distribute oscillator strength between the visible B and Q bands more accurately than the global hybrid B3LYP functional, at similar computational expense. These computational results elucidate TPA-active states at energies that correlate well with our experimental observations, and that have not been predicted for similarly-structured

compounds by earlier models.⁸⁷⁻⁸⁸ This combined experimental and theoretical work thus demonstrates: i) intense TPA-bands with energies of 1.84–2.48 eV (laser excitation wavelength range of 1000–1350 nm) that have not been fully explored in previous works of related, highly-conjugated multiporphyrin chromophores,⁷⁵⁻⁷⁶ ii) the spectroscopic significance of the characteristic orbital bands that emerge from the four canonical Gouterman orbitals in *meso*-to-*meso* ethyne-bridged porphyrin oligomers, and iii) a clear relationship between the structural characteristics of these compounds and their two-photon activity. Taken together, the results thus highlight NIR-emissive porphyrin arrays possessing unrivaled two-photon absorptivity in NIR-II excitation region for multi-photon imaging platforms while identifying key parameters for further chromophore design for large two-photon activity.

3.2 Result and discussions

3.2.1 Linear optical properties of PZn_n

Highly conjugated *meso*-to-*meso* ethyne-bridged (porphinato)zinc(II) oligomers manifest exceptional optical and electronic characteristics that include strongly allowed, Q-state derived π - π^* excited-states that are polarized along the long molecular axis (Q_x). These give rise to $S_0 \rightarrow S_1$ transitions that are intense and narrow [PZn_n : $\epsilon(S_0 \rightarrow S_1) \sim 229\,000\text{ M}^{-1}\text{ cm}^{-1}$, FWHM = 1562 cm^{-1}], and $S_1 \rightarrow S_n$ transitions that extend deep into the NIR spectral region with extinction coefficients on the order of 10^5 .^{47, 50-52} Table 2 exemplifies the trend of $\lambda_{1,\text{max}}$ of PZn_n with various conjugation length, the larger ϵ_{S_1} and lower energy S_1 state with increased conjugation length.

Table 2. Spectroscopic parameters of *meso-to-meso* ethyne-bridged (porphinato)zinc(II) oligomers measured in THF (ϕ : quantum yield, σ_2 : two-photon absorption cross-section)

Compound	$\lambda_{1,\max}$ (nm)	ϕ	λ_{TPA} (nm)	σ_2 (GM)	$\sigma_2 \phi$ (GM)
ZnTPP	555	0.03	1100	7.7	0.23
EPZnE	633	0.09	1120	13	1.1
PZn ₂	695	0.16	1030	1300	210
PZn ₃	770	0.22	1100	7000	1400
PZn ₅	842	0.14	1040	76000	11000
			1280	15000	2100

3.2.2 Density functional theory calculation on PZn_n

For the quantum chemical modeling of the electronic spectra for large molecules (> 30 non-hydrogen atoms), linear response TDDFT has emerged as the most accurate method (errors < 0.1 eV) that is tractable on commonly available computer systems.⁸⁹ While TDDFT is formally an exact theory, it is implemented with approximate exchange-correlation potentials, such as B3LYP,⁹⁰⁻⁹² that may exhibit incorrect asymptotic behaviors with respect to electron-nucleus separations. In the context of interrogating the electronic excitations of π -conjugated materials such as **PZn_n**, the most important consequences of this are poor accounting for the dependencies of polarizabilities upon system sizes, and the prediction of ‘ghost states’, charge-transfer type excited states that should lie in the UV range but are instead assigned visible-range energies.^{89, 93-94} Range-separation, as implemented in functionals including M11,⁹⁴ corrects these errors by

decomposing the Coulomb operator into short-range and long-range parts, where differing portions of the nonlocal Hartree-Fock-type exchange are admixed into a semilocal approximation.⁹⁵

Thus, range-separation improves the simulation of the \mathbf{PZn}_n spectrum by i) more accurately predicting the $S_0 \rightarrow S_1$ transition energy, ii) more correctly distributing the visible-range oscillator strength, and iii) eliminating spurious charge-transfer excitations from the predicted spectrum. This final point is especially significant because the resulting clarity aids the interpretation of the calculation, and because it permits simulation of the entire spectrum with a much reduced matrix of excited states (23 versus >60), affording an enormous reduction of the calculation's computational cost.

It has been previously observed that conjugation of two porphyrin macrocycles by a strongly coupling ethyne or butadiyne bridge leads to a dimer in which eight frontier orbitals are responsible for the visible-range optical transitions. Oligomers of three or five repeat units, as illustrated in Figure 9(A), give rise to 12 and 20 essential frontier levels that can be categorized into four bands based upon the degrees of interaction between their monomer Gouterman-derived orbitals. In two of these bands [green boxes in Figure 9(A)], nodal planes run the lengths of the bridge axes (Figure 10, Figure 11, and Figure 12); this restricts the delocalization of these orbitals and imparts them with nonbonding character. The other two bands [framed by purple dashed lines in Figure 9(A)] feature substantial interporphyrin wavefunction overlap that engenders varying degrees of bonding interaction (Figure 10, Figure 11, and Figure 12). The

nonbonding-character bands, the orbitals with nodal planes along the bridge axis, thus feature localized states that are near isoenergetic with their monomeric basis functions, while the bonding-character bands, with delocalized interporphyrin wavefunction distribution, are comprised of orbitals dispersed about their basis function energies. The widths of these bonding-character bands [occupied orbital band width for $\text{PZn}_2 = 0.91$ eV, for $\text{PZn}_3 = 1.23$ eV and for $\text{PZn}_5 = 1.47$ eV, Figure 9(A)] have been correlated with the strength of interporphyrin communication in work on similarly constructed porphyrin dimers.^{88, 96}

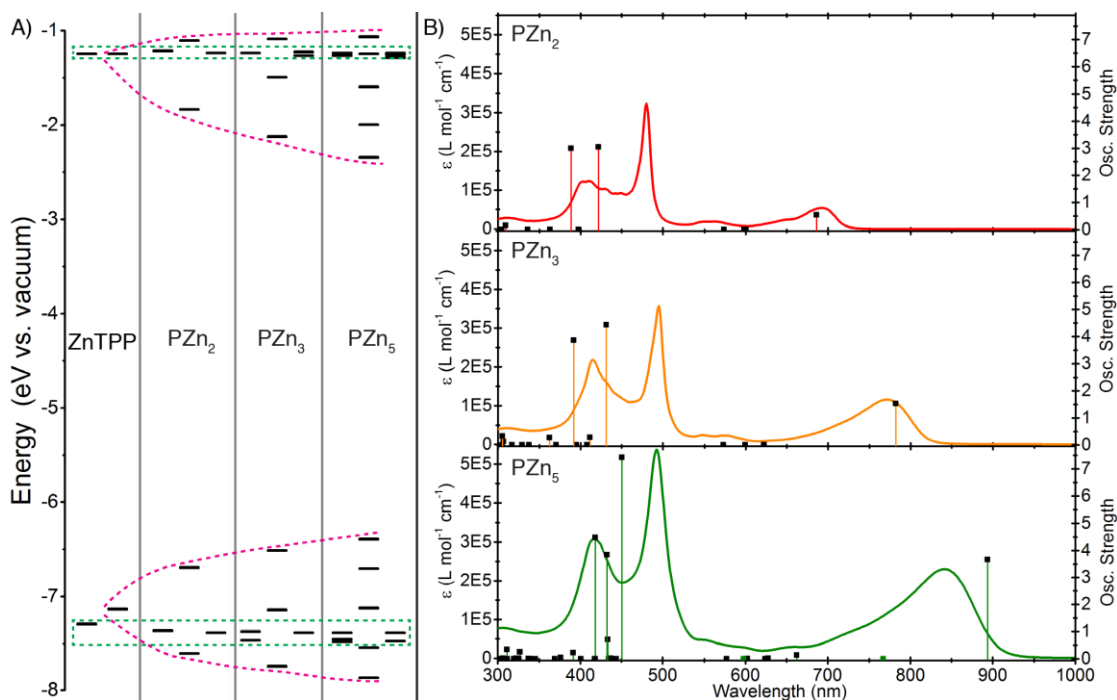


Figure 9. (A) Development of the four frontier orbital bands in PZn_n . Green boxes enclose the nearly-degenerate nonbonding orbitals, while the bonding orbitals are evenly dispersed between the purple lines. (B) Electronic spectra (lines) of PZn_n compounds measured in THF solvent, and (squares) TDDFT-calculated transition energies of these same compounds. Computational data obtained using PCM solvation model (THF) and M11/6-311g(2d).

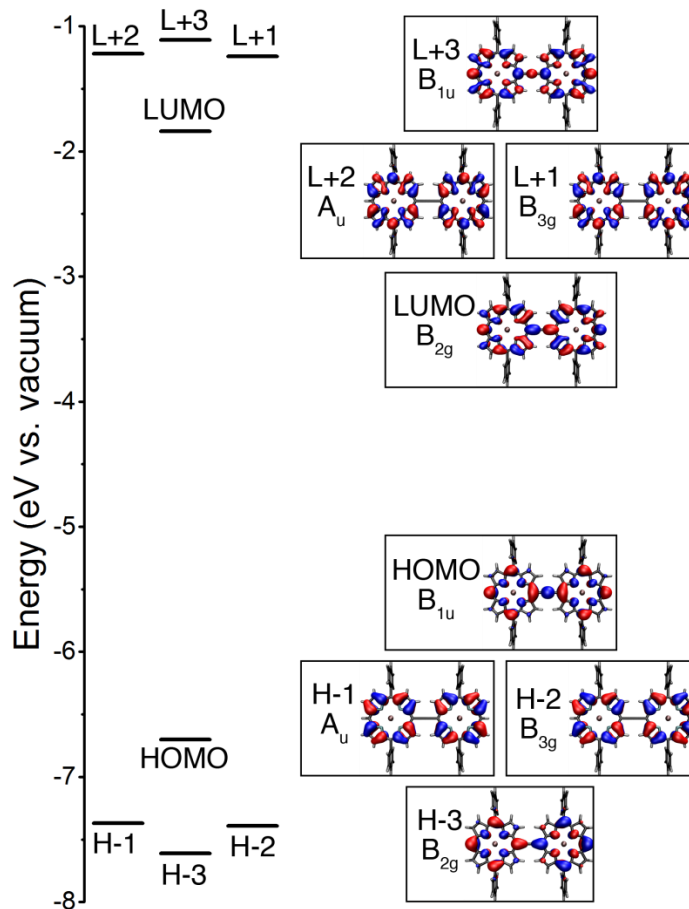


Figure 10. Frontier orbitals of PZn₂ (D_{2h} point group) plotted as 0.02 isodensity surfaces along with a diagram comparing their calculated energies. Those which comprise the highly delocalized bonding and antibonding bands are labeled H (HOMO), L (LUMO), H-1, L+1, etc. with bonding and antibonding bands explained in text. Computational data obtained using PCM solvation model (THF) and M11/6-311g(2d). The generation of TPA-allowed *u*(ungerade)–*u* or *g*(gerade)–*g* transitions explains the enormous TPA at an energy nonresonant with one-photon transitions for PZn₂

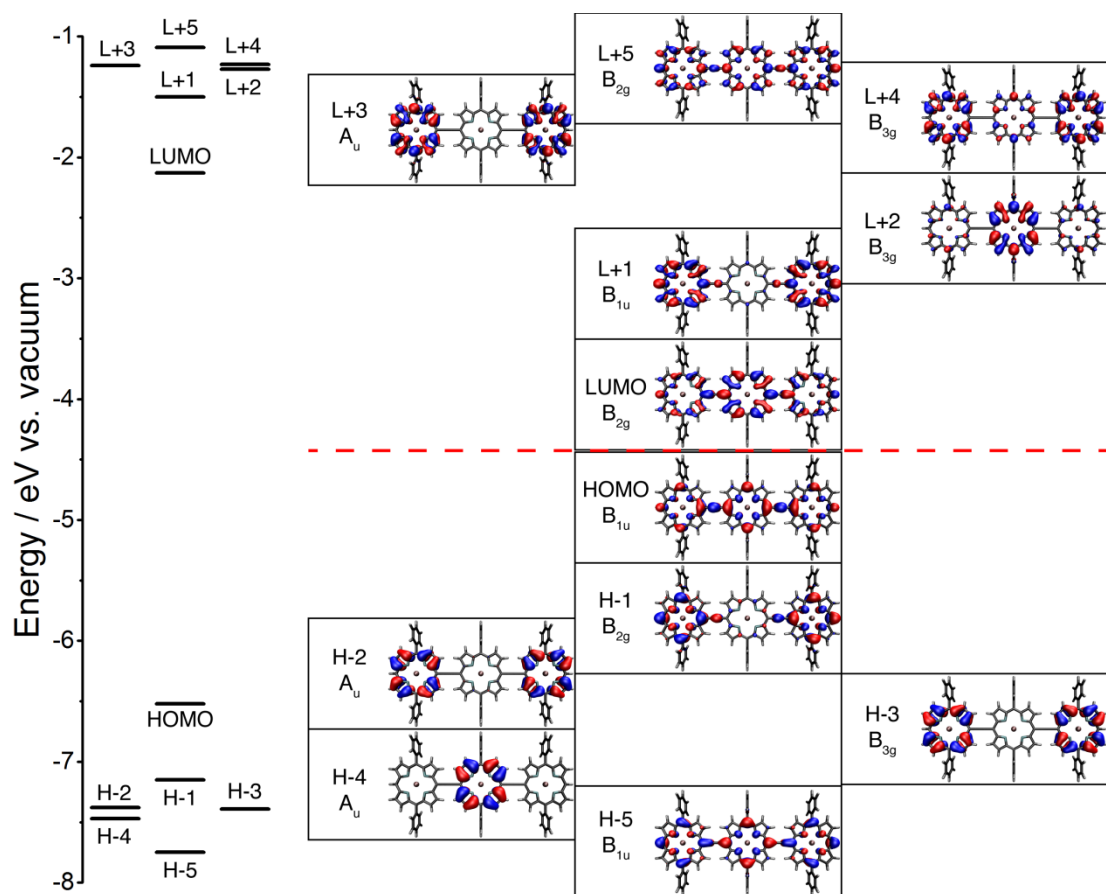


Figure 11. Frontier orbitals of PZn₃ plotted as 0.02 isodensity surfaces along with a diagram comparing their calculated energies. Computational data obtained using PCM solvation model (THF) and M11/6-311g(2d).

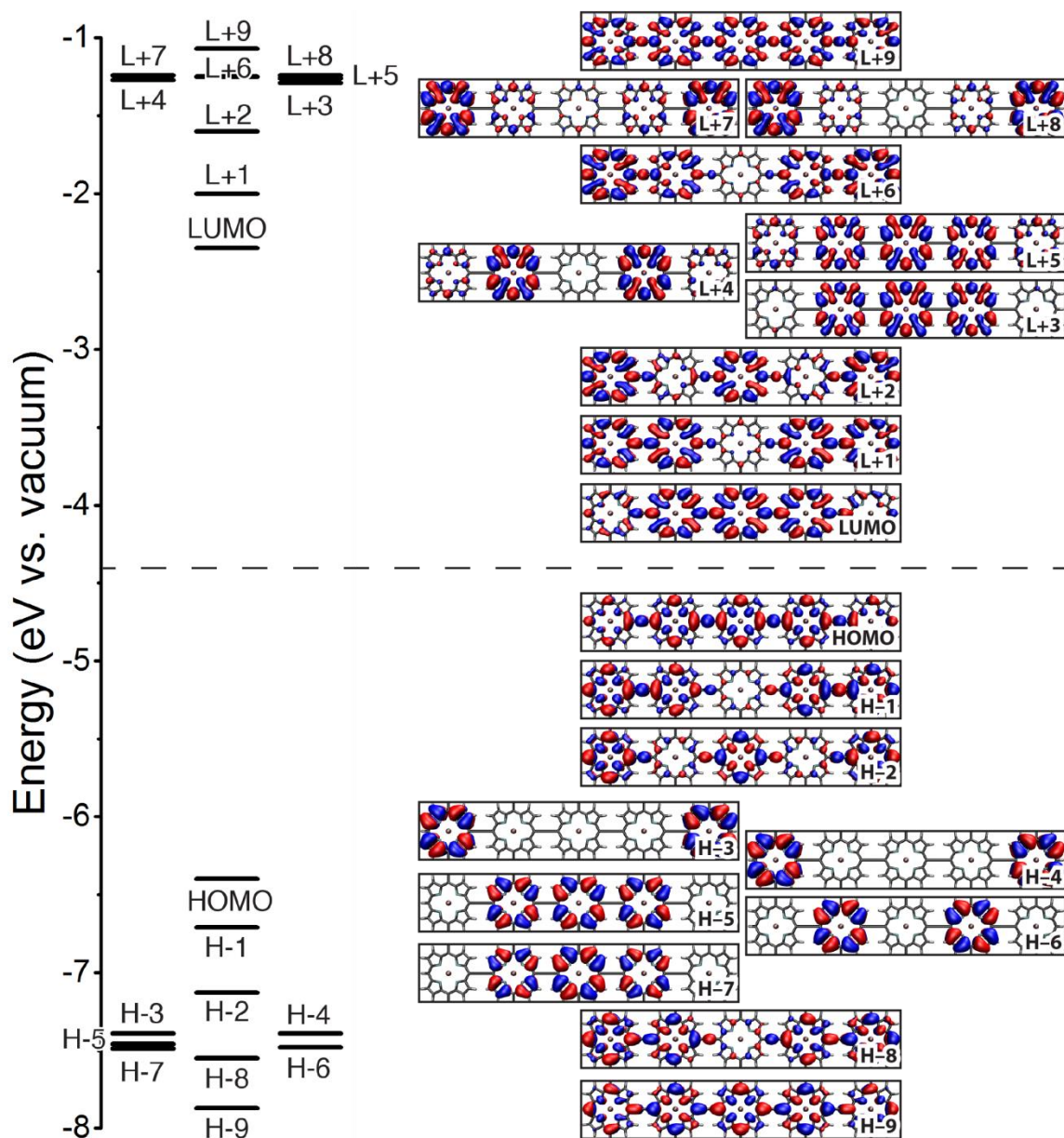


Figure 12. Frontier orbitals of PZn₅ plotted along with a diagram comparing their calculated energies. Computational data obtained using PCM solvation model (THF) and M11/6-311g(2d).

Table 3. Summary of calculated excited states of PZn_n and the corresponding assignment of the major states of one-photon absorption (OPA) and TPA transitions. Major contributions to each state were color-coded to clarify the characteristics of the responsible transition (black : bonding→ nonbonding, blue : bonding→bonding, and pink : nonbonding→nonbonding)

State number	ν / cm^{-1}	λ / nm	E / eV	f^a	Symmetry	Assignment	Major contributions
PZn₂							
1	14572.9	686.20	1.807	0.5396	Singlet-B _{3u}	Q _x	H-3->L+3 (13%) H-2->L+2 (10%) H-1->L+1 (10%) HOMO->LUMO (69%)
2	16659.5	600.26	2.066	0.0002	Singlet-B _{2u}	Q _y	H-3->L+2 (16%) H-2->L+3 (18%) H-1->LUMO (33%) HOMO->L+1 (35%)
4	17431.4	573.68	2.161	0	Singlet-A _g	TPA	H-3->LUMO (24%) H-2->L+1 (22%) H-1->L+2 (22%) HOMO->L+3 (31%)
5	23726.6	421.47	2.942	3.0466	Singlet-B _{3u}	B _x	H-2->L+2 (37%) H-1->L+1 (39%) HOMO->LUMO (22%)
7	25756.7	388.25	3.194	3.0008	Singlet-B _{2u}	B _y	H-2->L+3 (12%) H-1->LUMO (38%) HOMO->L+1 (43%)
PZn₃							
1	12788.8	781.93	1.586	1.5359	Singlet-B _{3u}	Q _x	H-1->L+1 (10%) HOMO->LUMO (71%)
2	16067.5	622.38	1.992	0	Singlet-A _g	TPA	H-3->L+4 (12%) H-2->L+3 (14%) H-1->LUMO (25%) H-1->L+5 (10%) HOMO->L+1 (28%)
3	16080.4	621.88	1.994	0.0007	Singlet-B _{2u}	Q _y	H-4->LUMO (39%) H-4->L+5 (11%) HOMO->L+2 (31%)
5	16683.7	599.39	2.069	0.001	Singlet-B _{2u}	Q _y	H-3->L+1 (24%) H-2->LUMO (16%) H-2->L+5 (11%) H-1->L+3 (22%)

							HOMO->L+4 (16%)
7	23195.9	431.11	2.876	4.4294	Singlet-B _{3u}	B _x	H-4->L+2 (36%) H-4->L+4 (14%) H-3->L+3 (15%) HOMO->LUMO (14%)
11	25531.7	391.67	3.166	3.8597	Singlet-B _{2u}	B _y	H-3->L+1 (17%) H-2->LUMO (24%) H-1->L+3 (17%) HOMO->L+2 (18%) HOMO->L+4 (13%)
PZn₅							
1	11189.4	893.70	1.387	3.6625	Singlet-B _{3u}	Q _x	H-1->L+1 (16%) HOMO->LUMO (60%)
2	13034.8	767.18	1.616	0	Singlet-A _g	TPA	H-1->LUMO (30%) HOMO->L+1 (34%)
3	15094.0	662.52	1.872	0.1425	Singlet-B _{3u}	Q _x	H-2->LUMO (19%) H-1->L+1 (17%) HOMO->L+2 (22%)
4	15940.9	627.32	1.977	0.0229	Singlet-B _{2u}	Q _y	H-5->LUMO (27%) HOMO->L+3 (22%)
6	16030.4	623.82	1.988	0.0009	Singlet-B _{2u}	Q _y	H-7->LUMO (27%) H-6->L+1 (11%) HOMO->L+5 (18%)
9	16729.7	597.74	2.074	0	Singlet-A _g	TPA	H-4->L+8 (11%) H-3->L+7 (12%) HOMO->L+6 (12%)
11	22199.0	450.47	2.753	7.4188	Singlet-B _{3u}	B _x	H-7->L+5 (23%) H-6->L+4 (20%) H-5->L+3 (26%)
16	23120.0	432.53	2.867	3.8396	Singlet-B _{2u}	B _{y,1}	H-5->LUMO (25%) HOMO->L+3 (31%)
18	23927.4	417.93	2.967	4.4806	Singlet-B _{2u}	B _{y,2}	H-4->L+1 (14%) H-3->L+2 (12%) H-2->L+8 (12%) H-1->L+7 (16%)

(* Oscillator strength)

Correlations of these computational data with parameters from the experimental spectra permit an extension of Gouterman's four-orbital model to these multiporphyrin arrays.^{43,97} For **PZn₂₋₅**, the x-polarized (x taken as the highly conjugated axis) Q transition (Q_x) is 60-70% comprised of a HOMO→LUMO configuration (Table 3), and the x-polarized B transitions (B_x) are composed of a larger number of one-electron excitations spanning the range of the bonding-character orbital bands. Gouterman's model draws a linear correlation between the energetic degeneracy of the tetrapyrrole frontier orbitals and the fraction of visible oscillator strength allocated to the Q-transitions. For **PZn_n** compounds, the widths of the bonding-character orbital bands are the equivalents to Gouterman's deviation from degeneracy of monomeric porphyrin frontier orbitals; plotting the dependence of Q oscillator strength over the total visible oscillator strength gives a linear fit (data not shown). Because these frontier bands have widths that are correlated with the strength of interporphyrin electronic communication, this linear dependence connects the Q-band strength directly with porphyrin linkage motif.

3.2.3 Comparative TPA properties of the benchmark porphyrin monomers and PZn₂

For unmodified porphyrin monomers, σ_2 values were known to be insignificant for both the Soret and the Q-band transition regions. In previous works on porphyrin monomers' TPA cross-sections, σ_2 values in the Q-band region were measured <10 GM.⁷⁰⁻⁷¹ We observed the maximum experimental TPA value for **ZnTPP** is 7.7 GM at 1100 nm (Figure 13), consistent with the previous reports on porphyrin monomers. It is worth noting that the selection rule of electronic transitions for centrosymmetric chromophores

maintains mutual exclusivity for OPA (one-photon absorption) and TPA; OPA is allowed for transitions between antisymmetric states whereas TPA is allowed for transitions between symmetric (initial and final) states. Figure 14 shows possible transitions for **ZnTPP** from HOMOs to LUMOs are only antisymmetric, consistent with Gouterman four-orbital model,⁴³⁻⁴⁴ which correspond to OPA-allowed but TPA-forbidden from calculated energy diagram. However, **ZnTPP** (D_{4h} point group) shows overlapping OPA and TPA spectral peaks in the Q-band region experimentally (Figure 13), in apparent violation of this basic selection rule. The coincidence of these TPA peaks with $Q_{1,0}$ and $Q_{2,0}$ bands (594 and 555 nm) has been explained in the context of symmetry breaking by *meso*-phenyl ring librations and/or the mixing of vibronic and electronic wavefunctions.⁷⁰ Another monomer, **EPZnE**, whose *meso*-ethyne groups extend the π -conjugation and lower the symmetry with respect to **ZnTPP**, exhibits similarly weak TPA in this energy range (13 GM at 1120 nm, Figure 13) implying that simple extension of π -conjugation along a molecular axis has little effect on the magnitude of TPA for porphyrin monomers.

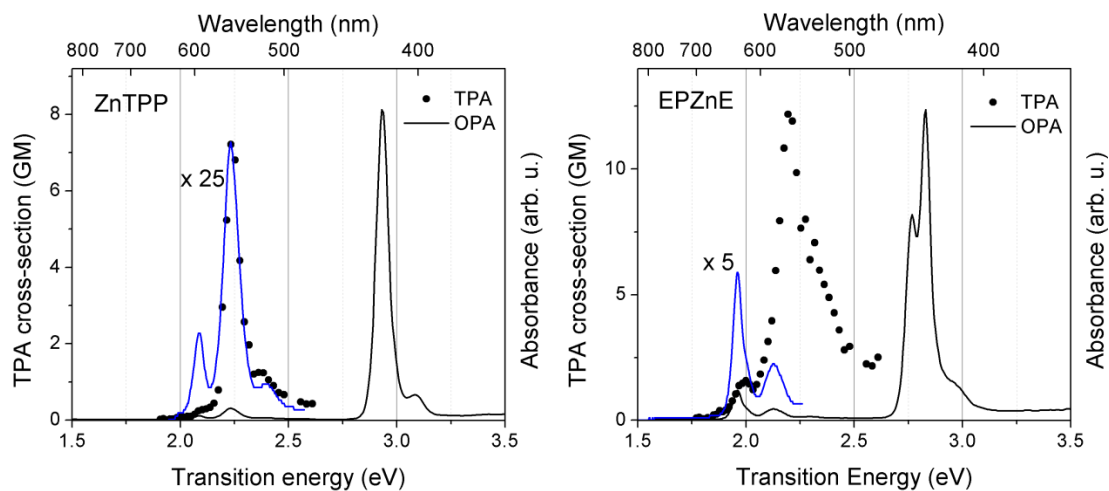


Figure 13. One- (solid line) and two-photon (black dot) absorption spectra of ZnTPP and EPZnE in THF [including magnified linear absorption spectra (blue lines) in the Q-band regions]. TPA spectra are plotted with doubled laser excitation energy for direct comparison with one-photon absorption spectra.

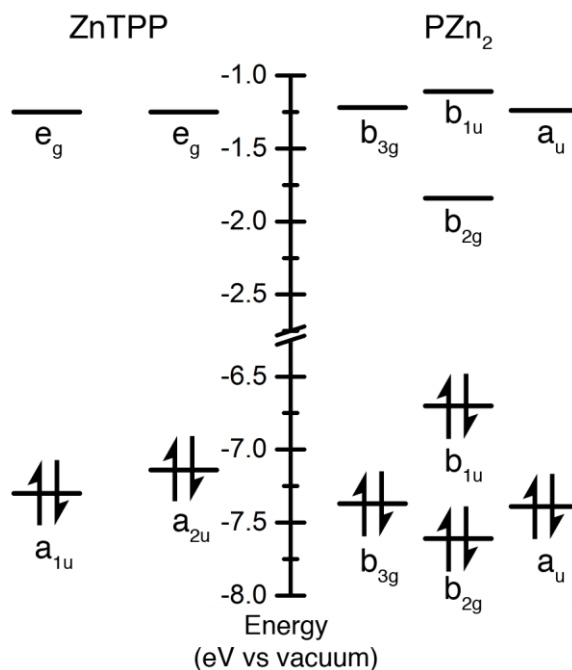


Figure 14. Energy diagram of ZnTPP and PZn₂ comparing their frontier orbital energies. Computational data obtained using PCM solvation model (THF) and M11/6-311g(2d).

The linkage of two monomer units through effective π -conjugated connectivity turns these poor TPA chromophores into a potent two-photon absorber. **PZn₂** exhibits a maximum TPA cross-section of 1300 GM at 1030 nm (Table 2 and Figure 15), ~170 times larger than that of **ZnTPP**, and consistent with measurements of a similar ethyne-bridged porphyrin dimer in benzene by Rebane and coworkers (~1000 GM at 1030 nm).⁷⁹ The intensity of this TPA peak, as well as the fact that it lies at an energy that is nonresonant with OPA, signifies a TPA-allowed, one-photon forbidden state that is not present in monomeric porphyrins. Note that prior studies have more extensively explored TPA at Soret-resonant energies for similar *meso*-ethyne and butadiyne dimers, reporting $\sigma_{2,\max} \sim 7000$ GM at 830 nm for an ethyne-bridged dimer and $\sigma_{2,\max} \sim 6000$ GM at 840 nm for the corresponding related butadiyne-bridged dimer.⁷⁵⁻⁷⁶ Our recent work involving extraction of pure TPA cross-sections using pulse train shaping methods that suppress linear contributions to the fluorescence derived from hot-band OPA contributions reveals a cross-section $\sigma_2 = 2100$ GM for **PZn₂** at 800 nm.⁸⁰

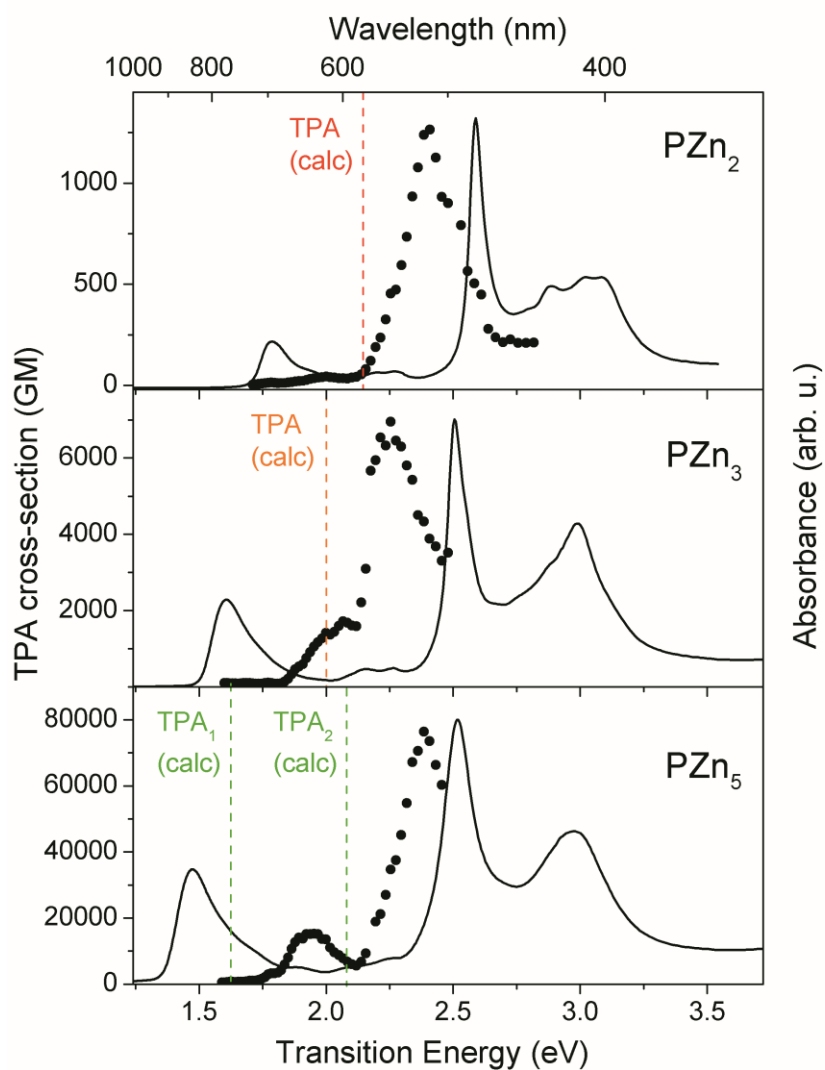


Figure 15. One- (solid line) and two-photon (black dot) absorption spectra of PZn_n in THF, with calculated energies for TPA states depicted as colored dotted lines. TPA spectra are plotted with doubled laser excitation energy for direct comparison with one-photon absorption spectra; computational data obtained using PCM solvation model (THF) and M11/6-311g(2d).

For conjugated porphyrin dimers (e.g. para-phenylene-bridged porphyrin dimers,⁷⁹ strapped *meso-meso* linked diporphyrins,⁹⁸ and doubly β -to- β butadiyne-bridged diporphyrins⁹⁹), it has been common to observe σ_2 values that are two orders of

magnitude larger than those for monomers and several theoretical approaches have been focused to understand the enhancement in context of cooperative enhancement and an essential three state model. Note that, however, most TPA values reported for porphyrin dimers have been limited to two-photon states lying above the S_2 band, falling into the energy range accessible by laser excitation under the conventional imaging window (700–1000 nm); in those cases, the TPA transitions were assigned to A_{1g} state excitations (S_{TPA}) above the lowest energy Soret-manifold state, substantially higher energies (23000–25000 cm^{-1} ; 2.85–3.10 eV)^{75-76, 100} than are observed here for ethyne-bridged compounds (1.94–2.41 eV).

For **PZn₂**, our TDDFT calculations using M11 functional predict a similar two-photon allowed A_{1g} excited state at 2.16 eV, below the lowest energy Soret-manifold state, congruent with the experimentally observed S_{TPA} at 2.41 eV (Table 2 and Figure 15). In similar fashion to previous models, the S_{TPA} derives from the in-phase and out-of-phase combinations of monomer-derived orbitals, and this state is thus nonexistent for single porphyrin chromophores. The calculated S_{TPA} is characterized mainly by *gerade-gerade* ($H-3 \rightarrow L$ and $H-2 \rightarrow L+1$) and *ungerade-ungerade* ($H-1 \rightarrow L+2$ and $H \rightarrow L+3$) configurations (Figure 14). **ZnTPP** and related monomeric porphyrins have only *ungerade* states, excitations from *ungerade* to *gerade* orbitals (Figure 14), available within the energy range relevant to the promising window for *in vivo* imaging (1.84–2.48 eV; laser excitation wavelength of 1000–1350 nm).

3.2.4 Extremely large TPA cross-sections of PZn_n in the NIR-II window

The experimental two-photon absorption cross-sections of longer PZn_n arrays are shown in Figure 15 and summarized in Table 2. From dimer (PZn_2) to trimer (PZn_3), the experimental TPA cross-section is increased from 1300 GM at 1030 nm to 7000 GM at 1100 nm, which is a 5-fold intensity enhancement accompanied by a slightly red-shifted TPA peak wavelength. The largest TPA cross-section of 76000 GM at 1040 nm was found for PZn_5 , which is 1 order of magnitude larger than that of PZn_3 and ~50 fold larger than that of PZn_2 . Interestingly, while one-photon allowed Q_x transition energies of PZn_n decrease with increasing oligomer length, the major TPA transition energies do not show length dependence. Rather the TPA transition energies remain in the similar energies (2.41 eV, 2.25 eV and 2.38 eV for PZn_2 , PZn_3 , and PZn_5 , respectively). In addition, secondary TPA peaks become more evident as π -conjugation length increases; we observed a small additional transition ($\sigma_2 = 43$ GM at 1240 nm, Figure 15) from PZn_2 far below major TPA peak at 1030 nm. Similar second TPA peaks, but more vivid, were manifested by $\sigma_2 = \sim 1300$ GM at 1240 nm and $\sigma_2 = 12000$ GM at 1280 nm for PZn_3 and PZn_5 , respectively (Figure 15). (We will discuss TPA trends of PZn_n with TDDFT calculation later.)

These large values of TPA cross-sections of PZn_n at 1000 – 1350 nm excitation window (NIR-II) are rare. There are several chromophoric systems that displayed impressive TPA cross-section at $\lambda_{\text{ex}} = 1000 - 1500$ nm; meso- β doubly linked Ni(II) porphyrin dimer ($\sigma_{2,\text{max}} = 8000$ GM at 1400 nm),⁷⁷ quadruply azulene-fused porphyrin

($\sigma_{2,\max} = 7200$ GM at 1380 nm),¹⁰¹ hexaphyrin ($\sigma_{2,\max} = 9890$ GM at 1200 nm)¹⁰², extended bis(donor) squaraines ($\sigma_2 = 33000$ GM at 1050 nm),¹⁰³ and double-strand ladder complexes of butadiyne-linked porphyrin array ($\sigma_{2,\max} = 115000$ GM at 1325 nm)¹⁰⁴. The common feature of those systems is extended π -conjugation throughout the entire chromophores. However most of the systems suffer from the low quantum yield or high two-photon absorptivity only under a self-assembled structure, thus are not viable candidates for emissive two-photon imaging applications *in vivo*.¹⁰⁴⁻¹⁰⁶ A more direct figure of merit for MPM is the two-photon action cross-section ($\sigma_2\phi$) which accounts for fluorescence quantum yield along with two-photon absorption cross-section. **PZn5** displays two-photon action cross-section of 10000 GM at 1040 nm, which is comparable to ~47000 GM at 700–1000 nm of CdSe-ZnS quantum dot, the brightest inorganic single emissive unit. Also **PZn5**'s two-photon action cross-section of 2000 GM at 1280 nm is an unprecedentedly large value at that wavelength region, even higher than ZnS quantum dot ($\sigma_2\phi = 280$ GM at 1180 nm) and fluorescent proteins (e.g. tdTomato, $\sigma_2\phi = 200$ GM at 1050 nm) for NIR-II window.^{19, 107}

The TPA transitions studied in this work are non-resonant transitions reaching to one-photon forbidden but purely two-photon allowed states via intervening virtual states. A previously reported large value of σ_2 in the phenylene-vinylene polymer is transitions to the S_2 state with the aid of S_1 state as an intermediate state.¹⁰⁸ In contrast, TPA states populated by excitation of **PZn_n** at 1130–1100 nm are one-photon forbidden but two-photon allowed states (S_{TPA}) lying below S_2 and above S_1 states, a characteristic

of centrosymmetric chromophores. We find no corresponding one-photon transitions of **PZn_n** at this energy range (2.25–2.41 eV, Figure 9).

The advantage of this multiporphyrin for MPM can be visualized compared with a commercially available two-photon dye suitable for the conventional imaging window, e.g. R6G. The relative brightness under two-photon excitation is directly determined by two-photon action cross-section ($\sigma_2\phi$). The quantum yields for R6G and **PZn₃** are 0.92 (in MeOH) and 0.22 (in THF), respectively, producing ~30 times larger two-photon brightness of **PZn₃** than R6G ($\sigma_2\phi_{\text{R6G}} = 46 \text{ GM}$ at 800 nm; $\sigma_2\phi_{\text{PZn}_3} = 1400 \text{ GM}$ at 1100 nm). Additionally, the maximum σ_2 excitation wavelengths of **PZn₃** and R6G were used to estimate the maximum imaging depth that might be achieved with each, under a scattering condition in a 20% intralipid tissue phantom sample, this estimates ~1.8 times deeper imaging depth for **PZn₃**.¹⁰⁹ Thus, the use of **PZn₃** (λ_{ex} : 1100 nm) would extend the limit of imaging depth to approximately double, providing ~30 times more fluorescent signal than R6G (λ_{ex} : 800 nm) under the same power excitation.

These porphyrin arrays do not dissolve in aqueous medium as other simple porphyrins. However, our group has demonstrated that these oligomeric porphyrin arrays are readily incorporated into polymersomes in aqueous medium to create a targetable imaging platform with the potential to perform drug delivery functions.^{58-62, 110-118} These extremely large NIR TPA cross-sections of **PZn_n** add multimodal imaging via multi-photon microscopy to this list of capacities.

3.2.5 Theoretical interpretation based on the three essential state model

Although most TPA events are based on simultaneous absorption of two photons mediated by virtual states, it has been known that TPA transitions can be typically described in the context of three essential states utilizing spectroscopic information of real states;⁸¹

$$\sigma_2 = \frac{\mu_{mf}^2 \mu_{im}^2}{\Delta^2}$$

where i (S_i) the initial state, m (S_m) the one-photon allowed intermediate state, f (S_{TPA}) the final two-photon active state, $\Delta = |S_m - S_{TPA}/2|$ the detuning energy, and μ the transition dipole moment. Note that the detuning energy Δ is inversely proportional to the TPA efficiency. For **PZn_n** (D_{2h}) compounds, S_m corresponds with the long-axis polarized Q_x state, and S_{TPA} has A_{1g} symmetry.

The degree of TPA cross section increase with **PZn_n** repeat units can be rationalized by the facts that: i) increasing transition oscillator strength due to largely delocalized π -electron systems, and ii) detuning energies that decrease with oligomer length. These points may be elaborated as follows: i) The ground (S_0) and S_1 states in **PZn_n** compounds have been shown to evince delocalization lengths that are atypical of conventional conjugated materials. The general proportionality between transition dipole moments and π -system length offers one explanation for the enormous TPA cross sections observed in ethyne-bridged multiporphyrins. ii) Within this series of compounds, the TPA absorption energies depend upon molecular length much less than

do the one-photon Q_x energies. This shifting of the Q_x energies with PZn_n length thus effectively decreases the detuning energy (Δ), bringing the TPA events closer to resonance for the longest of these oligomers (Figure 16).

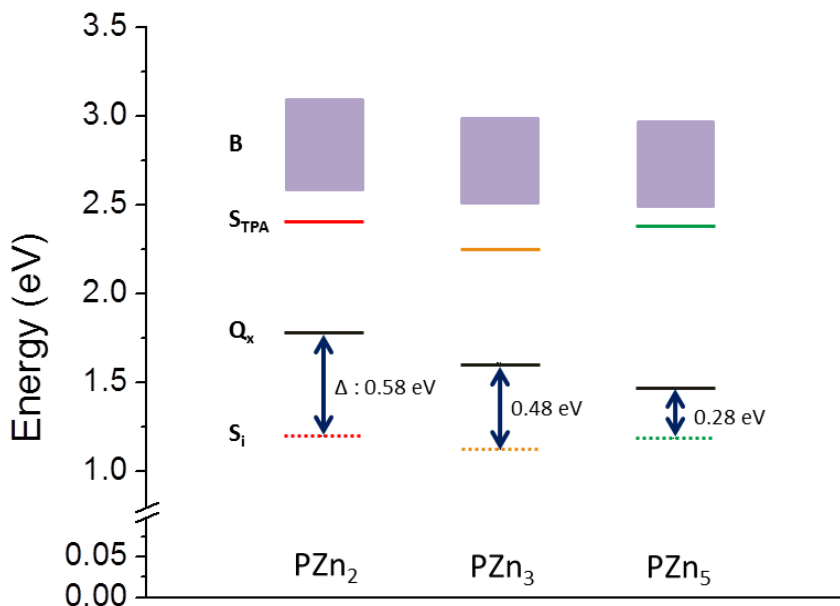


Figure 16. States diagram of PZn_n from linear (Q_x and B) and two-photon absorption (S_i and S_{TPA}) spectrum measured in THF; S_i is the intermediate state, Q_x is the x-polarized Q-state, S_{TPA} and the final two-photon active state, and B is the Soret state. The widths of B-band were calculated from the difference of the highest- and the lowest-energy Soret peaks in the linear absorption spectra.

3.2.6 TPA trends evident for PZn_n fluorophores

On the basis of these experimental and computational results, several trends are evident in these PZn_n two-photon absorption spectra.

Firstly, $\lambda_{TPA,max}$ of PZn_n is not coupled with molecular length, in contrast to the trend observed for phenylene-butadienylene oligomers¹⁰⁸, and oligomeric alkenes¹¹⁹⁻¹²⁰.

This feature suggests that the gap of frontier orbitals responsible for two-photon absorption in PZn_n is less affected by the degree of conjugation, unlike the case of $\lambda_{TPA,max}$

of phenylene-butadienylene oligomer and oligomeric alkenes, and the Q_x band (linear absorption) of PZn_n . A possible cause for the decoupling of $\lambda_{TPA,max}$ from the conjugation length of PZn_n is more involvement of non-bonding character orbitals in the corresponding excited state wavefunctions (Table 3). For the Q_x transition of PZn_2 , DFT calculations indicate that the major contribution is HOMO (bonding-character) – LUMO (bonding-character) transition (69 %) which shows systematic decrease of HOMO-LUMO gap as the conjugation degree increase. Similarly, HOMO-LUMO transitions are dominant portions for Q_x of PZn_3 (71 %) and PZn_5 (60 %) as well. In contrast, the TPA allowed transitions evince greater contributions from excitations between nonbonding-character orbitals; the TDDFT-calculated TPA-active state for PZn_2 displays approximately 45 % of excitations between nonbonding-character orbitals ($H-2 \rightarrow L+1$ and $H-1 \rightarrow L+2$, Table 3). Also it was found that ~ 26 % ($H-3 \rightarrow L+4$ and $H-2 \rightarrow L+3$) and ~ 23 % ($H-4 \rightarrow L+8$ and $H-3 \rightarrow L+7$) of two-photon allowed states of PZn_3 and PZn_5 , respectively, are derived from excitations between the nonbonding-character orbitals. This observation provides insight into an important factor that serves to decouple $\lambda_{TPA,max}$ and $\sigma_{2,max}$ by controlling molecular length of macrocyclic chromophore connected through efficient π -electron bridges because of the generation of isoenergetic molecular orbitals with monomeric character by poor wavefunction overlap between macrocyclic units.

Secondly, the FWHM of the TPA manifolds for these PZn_n fluorophores is independent of molecular length as well. Figure 17 depicts the single and multi

Gaussian fits to two-photon absorption spectra of **PZn_n**. While Q_x (linear absorption) of **PZn_n** display progressively broadened FWHM (1085 cm⁻¹, 1380 cm⁻¹, and 1563 cm⁻¹)⁴⁷ as the oligomer length increases, mainly due to augmented conformational heterogeneity, the FWHM of the two-photon absorption bands remain in a similar range (**PZn₂** : 2260 cm⁻¹; **PZn₃** : 2187 cm⁻¹; **PZn₅** : 2077 cm⁻¹) which is independent to the oligomer length. Rather, FWHMs of **PZn_n**'s two-photon absorption band seem slightly reduced, counter to the intuition from the linear absorption spectra. This observation suggests that the energies of S_{TPA} for these chromophores are less sensitive to conformeric librations, such as changes in the angles between porphyrin consensus planes, than are their one-photon allowed Q and Soret-manifold states. This might be interpreted as a result of the abovementioned contribution to S_{TPA} of orbitals from the nonbonding band, whose energies are similarly independent of intermacrocycle angle. Alternatively, it may be that only a subset of **PZn_n** conformers, such as those with maximal wavefunction delocalization, contributes significantly to TPA. One result which may support the latter view is that of Anderson and coworkers, who found for a similar butadiyne-bridged porphyrin octamer that TPA of ~50000 GM could be observed at ~1300 nm only upon formation of double-stranded ladders, an assembly process known to enhance porphyrin coplanarity.¹⁰⁴

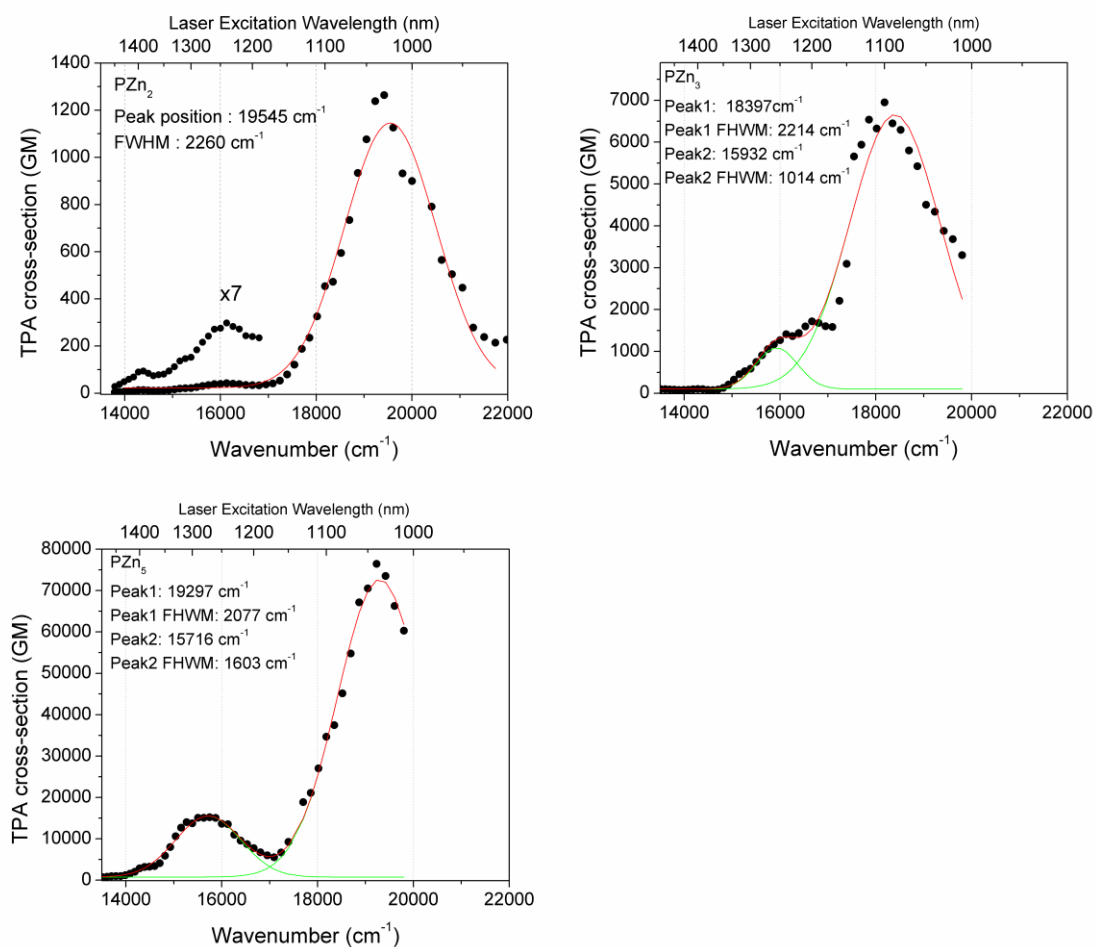


Figure 17. Single and multiple Gaussian fits to the two-photon absorption spectra of PZn_n in THF. TPA spectra are plotted with doubled laser excitation energy (bottom x-axis) to clarify the final two-photon accessible states.

Lastly, we found that the increase of $\sigma_{2,max}$ of PZn_n shows clear correlation to molecular length (or the number of π -electrons). For highly conjugated chromophores, σ_2 is predicted to be proportional to the fourth power the number of π -electrons (N_e)¹⁰⁴ and apparently to molecular length (L) as well, since the number of π -electrons is directly correlated with a molecular length in highly conjugated systems. Congruent with this prediction, PZn_n agree well with N_e^4 and L^4 dependence of TPA cross-section

due to extensive π -conjugation through entire chromophores (Figure 18). To estimate N_e dependence, the number of π -electrons of monomeric porphyrin unit and ethyne-bridge were considered to be 18 and 2, respectively, that yield relative N_e^4 of 1, 5.4 and 44, normalized by **PZn₂**. Because porphyrin is the macrocyclic structure, the molecular lengths was calculated by considering porphyrin as a hemisphere (10 bonds per monomeric porphyrin unit). This assumption produced the effective molecular length of **PZn_n** to be 32.12, 50.28, and 85.60 Å (relative L^4 of 1, 6.0, and 52 normalized by that of **PZn₂**, as well). The experimental TPA cross-sections were used from the maximum peak values (1300 GM, 7000 GM, and 76000 GM) to give relative TPA cross-sections of 5.0 and 55 of **PZn₃** and **PZn₅** normalized by σ_2 of **PZn₂**.

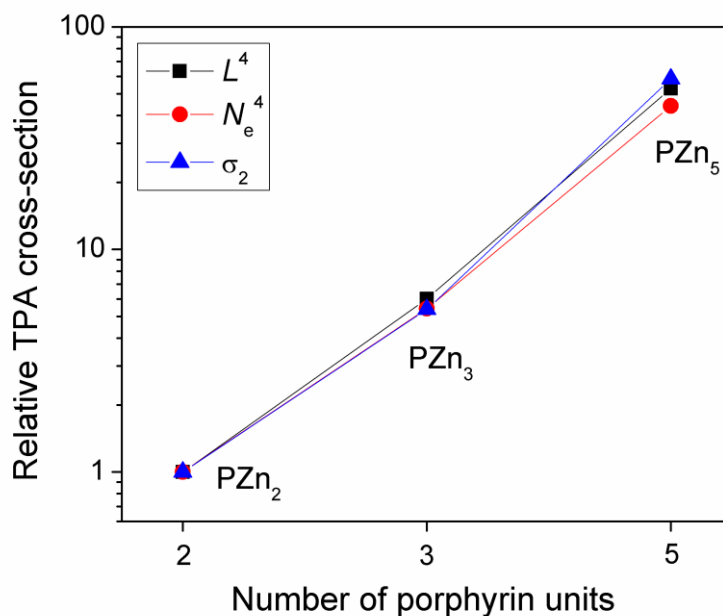


Figure 18. Plot of calculated relative molecular length (L) and number of π -electron (N_e) dependence of σ_2 and experimental σ_2 of **PZn_n**.

3.3 Conclusion

In this work we discovered exceptionally large TPA cross-sections of highly π -conjugated ethyne-bridged multiporphyrin arrays at wavelength range of 1000–1350 nm, NIR-II. This finding is significant because maximizing the efficacy of MPM requires brighter chromophores under long wavelength (particularly, NIR-II for tissue imaging) two-photon excitation. While porphyrin monomers exhibit small σ_2 values targeting S_1 state via two-photon transition, *meso-to-meso* ethyne-bridged multiporphyrins possess exceptionally large two photon cross-sections in the excitation range of 1000–1350 nm ($\sigma_{2,\text{max}}$ of dimer, trimer and pentamer measured 1300, 7000 and 76000 GM, respectively). The ethyne connectivity between porphyrin units plays crucial role in achieving good two-photon chromophores at long wavelengths by generating unoccupied and occupied orbitals of the same symmetry (gerade or ungerade). Calculations using the range-separated M11 functional provided an unprecedentedly accurate electronic structure model for these **PZn_n** compounds, including the four-band description of porphyrin oligomers and prediction of TPA allowed states. The large TPA cross-sections of these porphyrin arrays provide not only an opportunity to utilize long wavelength excitation for two-photon imaging, but also insight to designing super chromophores for enhanced two-photon absorption at desired wavelength range.

3.4 Experimental

3.4.1 Materials

The synthesis and characterization of **PZn_n** have been reported previously.^{47, 52} Sample solutions of **PZn_n** were prepared at concentrations of < 10 μ M in THF to avoid aggregation effects.

3.4.2 Instrumentation

Electronic spectra were recorded on an absorption spectrometer (Shimadzu, PharmaSpec UV1700) and an emission spectrophotometer (Edinburgh, FLSP920) in 10 mm quartz optical cells.

3.4.3 Two-photon absorption cross-section measurement

Two-photon absorption cross-section spectra were measured using standard TPEF (two-photon excited fluorescence) method.⁵ Excitation laser pulses were generated using a tunable optical parametrical amplifier (OPA; Light Conversion, TOPAS-C) with pulse widths of typically 100-120 fs. For excitation, a 1 cm-path-length quartz cell was placed in a weakly focused beam (12 mrad divergence angle) using a lens with 300 mm focal length. Loosely focused beam was used to avoid linear contribution from off-focus region.⁸⁰ Typical excitation power was kept below ~5 mW. Emission was collected at 90° with an amplified photodiode (Thorlabs, PDA36A) through an appropriate set of short-pass filters to reject scattered excitation light. A lock-in amplifier (Stanford Research Systems, SR830) was used to selectively measure the emission. Styryl 9M (Sigma-Aldrich) in chloroform was used as a standard in the wavelength range of 900 – 1500

nm.⁷ The emission intensity of porphyrin arrays as a function of excitation power was acquired to confirm quadratic dependence. We obtained the two-photon absorption cross section of chromophores relative to the standard Styryl 9M (taking into account the differences in the detection efficiency) using

$$\sigma_{2, sample} = \frac{[C]_{S9M} \eta_{S9M} \phi_{S9M} n_{S9M} \langle F \rangle_{sample}}{[C]_{sample} \eta_{sample} \phi_{sample} n_{sample} \langle F \rangle_{S9M}} \sigma_{2, S9M}$$

where $[C]$ is the concentration, η the collection efficiency of the system, ϕ the fluorescence quantum yield, n the refractive index and $\langle F \rangle$ the intensity of the detected fluorescence.

3.4.4 Computational methods

For the purpose of quantum chemical calculations, **PZn_n** were approximated as planar D_{2h}-symmetric structures, and alkoxyaryl groups were contracted to phenyl rings. Comparison of TDDFT calculations on the planar **PZn_n** with similar calculations on a twisted, approximately D_{2d} structure revealed that these apparently severe approximations are of surprisingly little consequence. Structures were optimized using the B3LYP global hybrid functional, the 6-311g(2d) basis set, and ief-pcm (tetrahydrofuran) solvation model as implemented in Gaussian09. TDDFT calculations reported in the main text were performed using the M11 functional, 6-311g(2d) basis sets, and ief-pcm (tetrahydrofuran) solvation model to obtain orbital energies, oscillator strengths of allowed transitions, and energies of one-photon forbidden states that contribute to two-photon absorption.

4. Nano-vesicular Two-photon in vivo Imaging Agent with Super-brightness for NIR-II Wavelength Excitation

4.1 Introduction

Two-photon fluorescence microscopy (TPM) has become a crucial optical imaging technique for highly scattering biological tissues providing high resolution structural information non-invasively.⁴ In the early stages of this technique, most applications were performed by excitation in the traditional near-infrared (NIR) biological imaging window (700–1000 nm, NIR-I), which is accessible *via* a Ti:Sapphire (Ti:S) laser.²⁹ Recently, the advancement of laser technology has enabled facile access to longer wavelengths, particularly in the second NIR tissue imaging window (NIR-II, 1000–1350 nm).²² These longer wavelengths enable deeper tissue imaging at high resolution, as light scattering is inversely proportional to wavelength; in addition, the absence of autofluorescence from endogenous chromophores at these wavelengths vastly improves signal-to-background ratio (SBR). Recently Kobat et al. demonstrated imaging depths up to 1.6 mm in murine cortical vasculature (1280 nm excitation with Alexa680-dextran as an exogenous marker).²⁴ In addition, work utilizing the intrinsic linear (one photon excitation) fluorescence of single wall carbon nanotubes in the NIR-II spectral region to image at anatomical resolution in whole mice emphasizes the importance of the NIR-II window in deep tissue imaging beyond the depth and SBR limit of NIR-I.^{64, 121}

The SBR of TPM depends largely on the brightness of the exogenous chromophore upon two-photon excitation, quantified by the two-photon action cross-

section $\sigma_2\phi$ (where σ_2 is the two-photon absorption cross section, and ϕ is the fluorescence quantum yield). Higher SBR improves the maximum possible imaging depth and lowers the input laser dose required, resulting in higher viability of living cells under laser excitation. While the majority of intrinsic and extrinsic two-photon fluorophores possess small σ_2 of <100 GM [GM : Goeppert-Mayer, 1 GM = 1×10^{-50} cm⁴ s photon⁻¹. (e.g. Rhodamine 6G, a “good” two-photon fluorophore, shows $\sigma_2 = 65$ GM at 800 nm)], a few chromophores have been reported with two-photon absorption cross-sections in excess of ~10,000 GM.^{77, 98, 103-104, 122-124} Most of these compounds with exceptional σ_2 , however, are poorly emissive or barely soluble in aqueous media and thus have limited application for TPM *in vivo*. Although Collins et al. demonstrated *in vivo* blood-vessel closure utilizing a butadiyne-bridged porphyrin dimer ($\sigma_2 = 17000$ GM at 916 nm) as a photo-sensitizer to generate singlet oxygen via two-photon excitation,¹²⁵ it has been limited to the conventional NIR-I excitation window. CdSe-ZnS core-shell quantum dots possess enormous two-photon action cross-sections of up to $\sigma_2\phi \sim 47000$ GM at $\lambda_{ex} = 700\text{--}1000$ nm, which are expected to remain large in the NIR-II region,³⁰ however their safety for *in vivo* applications is still in debate due to toxic elements.^{7, 47, 126-}

129

Thus, one of the current limiting factors for further utility of TPM *in vivo* is the lack of biocompatible fluorescent markers with large two-photon action cross-sections at long excitation wavelengths (NIR-II).

Meso-to-meso ethyne-bridged oligo(porphinato)zinc(II)-based supermolecules (**PZn_n**) define a family of near-infrared fluorophores (NIRFs) that exhibit substantial molar absorptivities throughout the visible and NIR regions,^{47-48, 51-52, 86} large NIR fluorescence quantum yields ($\phi = 14\text{--}22\%$)⁴⁷, and no chemical or photo-induced *in vitro* toxicity.¹³⁰ Recently we have observed that **PZn_n** display exceptionally large two-photon action cross-sections ($\sigma_2\phi$) ranging 210–11000 GM under NIR-II excitation wavelengths (Chapter 3). Through co-operative self-assembly with amphiphilic diblock copolymers, **PZn_n** NIRFs can be dispersed in aqueous media at high concentrations (up to 10 mol%) within the thick synthetic membranes of polymersomes (50 nm to 50 μm diameter polymer vesicles; Scheme 2).^{55, 57-61, 111, 131} The compartmental nature of these polymersomes (surface functionalization, membrane polymer composition, membrane and lumen encapsulants) allows rational tailoring of vesicle properties such as biodegradability,^{61, 132-133} membrane toughness,¹³⁴ specific adhesiveness,^{118, 135-136} pharmacokinetics and environmental responsiveness⁶¹ for a wide range of applications in *in vitro* and *in vivo* diagnostic imaging⁵⁸ and therapeutic delivery.^{57, 61} Polymersomes are chemically and structurally stable in physiological environments,⁵⁸ and the poly(ethylene oxide) surface of polymersomes confers a stealth-like character to prolong circulation times *in vivo*.¹³⁷

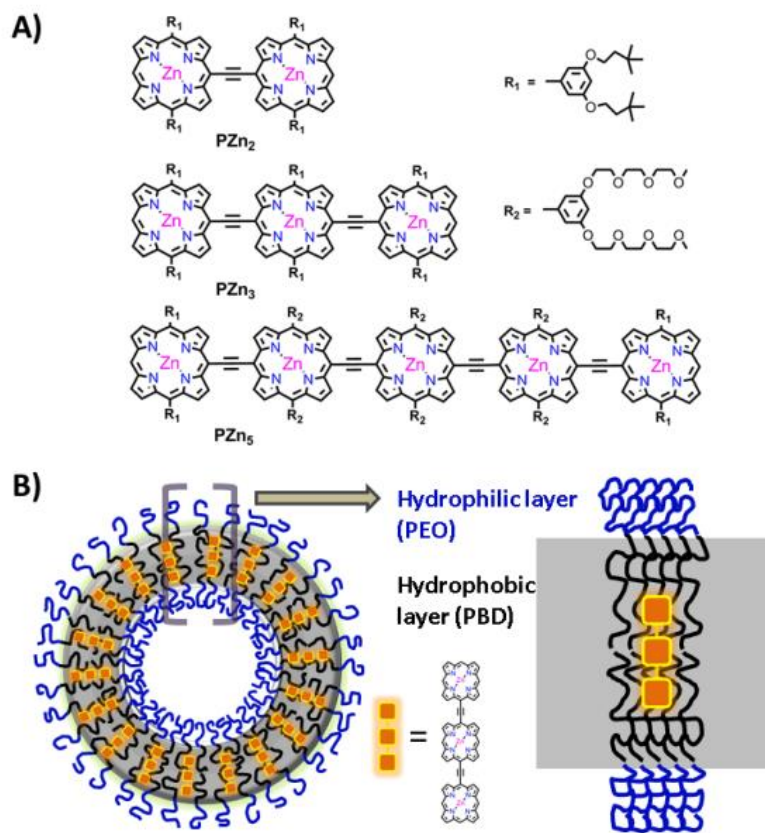
Here we explore the two-photon absorption of **PZn_n**-dispersed in the bilayer membrane of polymersomes and demonstrate the ability of the emissive polymersome as an *in vivo* two-photon imaging agent to visualize vasculature and localized cancer *via*

the enhanced permeability and retention (EPR) effect¹³⁸ in a mouse model. We prepared emissive polymersomes with **PZn₂**, **PZn₃**, and **PZn₅** and showed with fs-pulsed laser excitation, **PZn_n**-based polymersomes possess two-photon absorption (TPA) cross-sections of up to $\sim 10^8$ GM per vesicle at $\lambda_{\text{ex}} = 1050\text{--}1100$ nm. This nano-sized soft material with versatile functionality provides super-brightness (up to $\sigma_2\phi \sim 1.4 \times 10^7$ GM per vesicle) under NIR-II excitation, making it ideal for *in vivo* imaging applications.

4.2 Result and discussions

4.2.1 Sample characterization and optimization of **PZn_n-polymersome**

While polymersomes are able to stably incorporate up to 10 mol% **PZn_n**,^{60, 110-111} we have previously determined that the total integrated emission on a per nanoparticle basis is maximized at 5 mol% **PZn_n** in poly(ethylene oxide)-b-poly(1,2-butadiene) (PEO₈₀-b-PBD₁₂₅, denoted OB18), reflecting a trade-off between a greater number of fluorophores per vesicle, while minimizing intermolecular energy transfer within the membrane that leads to emission quenching.¹¹¹ Further studies revealed that **PZn₂** and **PZn₃** bearing 3',5'-di(3,3-dimethyl-1-butyloxy)phenyl *meso*-side chains [3,5-alk-**PZn₂** and 3,5-alk-**PZn₃** respectively; Scheme 2(A)] dispersed in OB18 showed augmented fluorescence over **PZn₂₋₃** possessing another ancillary group substituents due to favorable polymer-fluorophore interactions and a reduced inter-porphyrin torsional angle distribution.⁶⁰ Accordingly, we studied two-photon absorption of 3,5-alk-**PZn₂** and 3,5-alk-**PZn₃** and **PZn₅** in OB18 with a 5 mol% fluorophore concentration in this work.



Scheme 2. (A) Molecular structure of bis-, tris-, and pentakis(porphinato)zinc(II) (PZn_n) arrays. (B) Schematic structure of an emissive polymersome

NIR-emissive polymersomes (**PZn_n**-based polymersome), depicted schematically in Scheme 2(B), were formed as described previously *via* self-assembly by aqueous hydration of dry, uniform thin films of amphiphilic polymer and fluorophore deposited in prescribed molar ratios on roughened Teflon surfaces (see Experimental). Cryogenic transmission electron microscopy (cryo-TEM) confirmed vesicle morphology for all three samples (Figure 19); manual particle sizing gave average diameters of 137.6 ± 50.5 nm for **PZn₂**-based polymersome, 108.1 ± 38.1 nm for **PZn₃**-based polymersome, and 131.8 ± 68.3 nm for **PZn₅**-based polymersome.

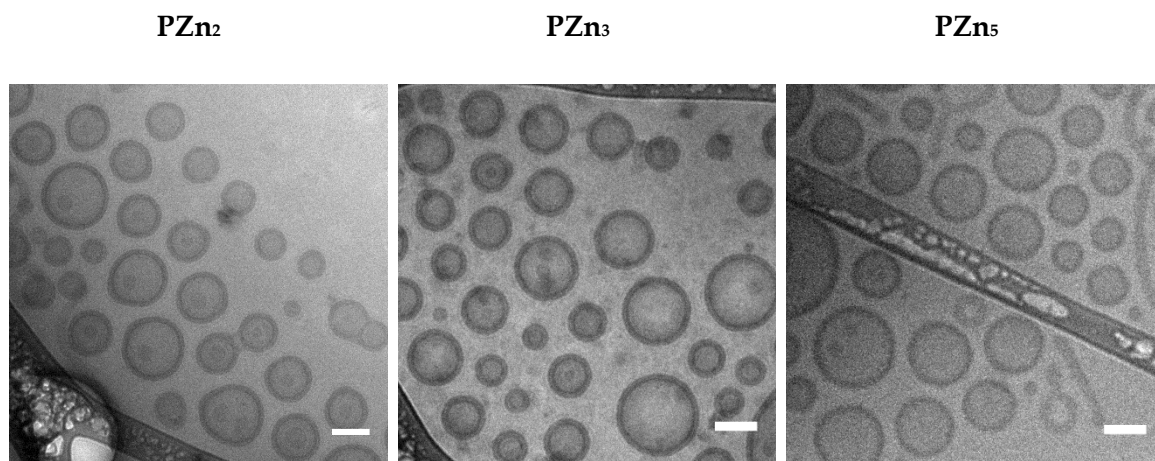


Figure 19. Cryogenic transmission electron microscopy (cryo-TEM) images of nano-sized PZn_n-based polymersomes. (In all three images, scale bar = 100 nm.)

4.2.2 Linear absorption and emission of PZn_n in PEO-PBD

Congruent with previous works,^{59, 111} PZn_n -based polymersomes manifest electronic absorption and emission features (Figure 20) that are similar to those in organic solvents⁴⁷⁻⁴⁸ with a broad S_2 band (~400–500 nm) and an intensified S_1 band (~700–900 nm) that progressively shifts to longer wavelengths as the conjugation length increases⁴⁷, reflecting well dispersed fluorophores in the bilayer membrane. Absorption of PZn_n -based polymersome reflect red-shifted peaks [20 nm (PZn_2), 33 nm (PZn_3), and 30 nm (PZn_5)] in comparison to those of PZn_n in THF while maintaining the signature of ethynyl-bridged multiporphyrins which is the characteristics of PZn_n bearing 3',5'-di(3,3-dimethyl-1-butyloxy)phenyl *meso*-side chains.⁵⁹ Their NIR emission appears at longer wavelength at the range of 726–906 nm which is 15 nm (PZn_2), 14 nm (PZn_3), and 23 nm (PZn_5) red-shifted from corresponding emission in THF. Red-shifted absorption and emission peaks reflect enhanced population of porphyrin arrays adopting more planarized structure in the hydrophobic bilayer. Fluorescence quantum yields of PZn_n dispersed in OB18 (6.0%, 6.9% and 2.0% for PZn_2 , PZn_3 , and PZn_5 , respectively, Table 4) are smaller than in THF (16%, 22% and 14% for PZn_{2-5} , respectively⁴⁷) mainly due to energy transfer dynamics between porphyrin units dispersed in the bilayer membrane.¹¹¹

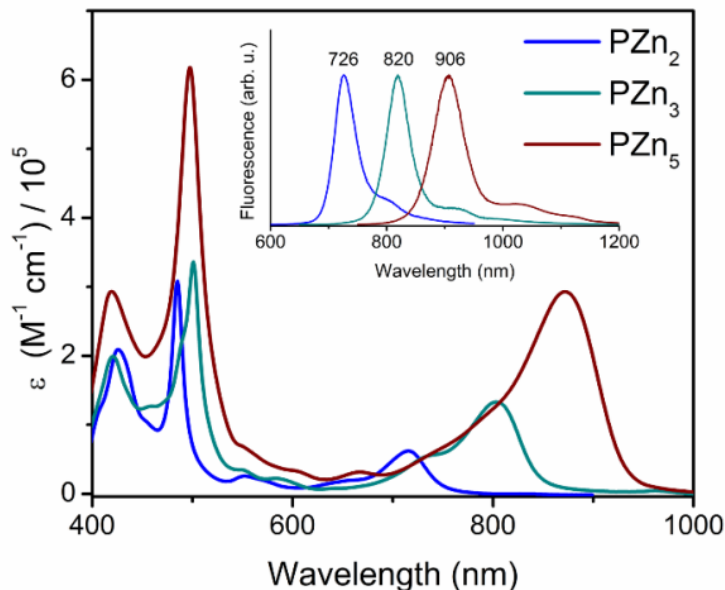


Figure 20. Extinction coefficient and emission spectra of PZn_n-based polymersomes dissolved in deionized water (DIW).

Table 4. Summary of linear and nonlinear spectroscopic parameters of meso-to-meso ethyne-bridged (porphinato)zinc(II) oligomers incorporated into aqueous dispersed OB18 polymersome (ϕ : fluorescence quantum yield and σ_2 : two-photon absorption cross-section)

	λ_{abs} /nm ^a	ϵ /M ⁻¹ cm ⁻¹ ^b	λ_{emi} /nm ^a	ϕ^c	σ_2 / GM per chromophores basis	σ_2 / GM per vesicle basis
PZn ₂ - OB18	715 (+20)	62 200 (51 400)	726 (+15)	0.060 (0.16)	2400	(2400×5500=) 13 200 000
PZn ₃ - OB18	803 (+33)	133 000 (116 000)	820 (+14)	0.069 (0.23)	8800	(8800×3000=) 26 400 000
PZn ₅ - OB18	872 (+30)	293 000 (230 000)	906 (+23)	0.020 (0.14)	143 000	(143000×5000=) 715 000 000

(^aNumbers in parentheses are the shift of wavelength compared to the respective transitions measured in THF in units of nm. ^bNumbers in parentheses are corresponding extinction coefficients in THF. ^cQuantum yields were measured using an integrating sphere and numbers in parentheses are corresponding ϕ in THF.)

4.2.3 Two-photon absorption of PZn_n in PEO-PBD

In a previous study (Chapter 3), we observed large TPA cross-sections from PZn_n in THF [$\sigma_2 = 1300$ GM (PZn_2); $\sigma_2 = 7000$ GM (PZn_3); $\sigma_2 = 76000$ GM (PZn_5)] under an excitation wavelength range of 1000–1350 nm (Table 4). Reflecting the similarity in the absorption and emission characteristics of PZn_n dispersed in polymersomes to that in bulk THF, the two-photon absorption cross-sections of PZn_n dispersed in polymersomes were observed to be similar in magnitude [$\sigma_2 = 2400$ GM at 1060 nm for PZn_2 , 8800 GM at 1100 nm for PZn_3 and 143000 GM at 1050 nm for PZn_5 (Figure 21)] peaking at 1050–1100 nm. A slight enhancement of TPA cross-section of PZn_n dispersed in polymersome compared to those in THF was noted; this could be potentially attributed to enhanced coplanarity of PZn_n and reduced detuning energy (the energetic difference between the first virtual state and the two-photon intermediate state) within the polymer membrane.⁸¹ Additional secondary TPA transitions of PZn_n peaked at ~1300 nm are still observed in polymersome as well which could be useful for longer wavelength excitation (i.e. ~1300 nm where local minimum of the water absorption exist) to image deeper by trading off relative two-photon brightness compared to maximum σ_2 of PZn_n with 1050–1100 nm excitation.

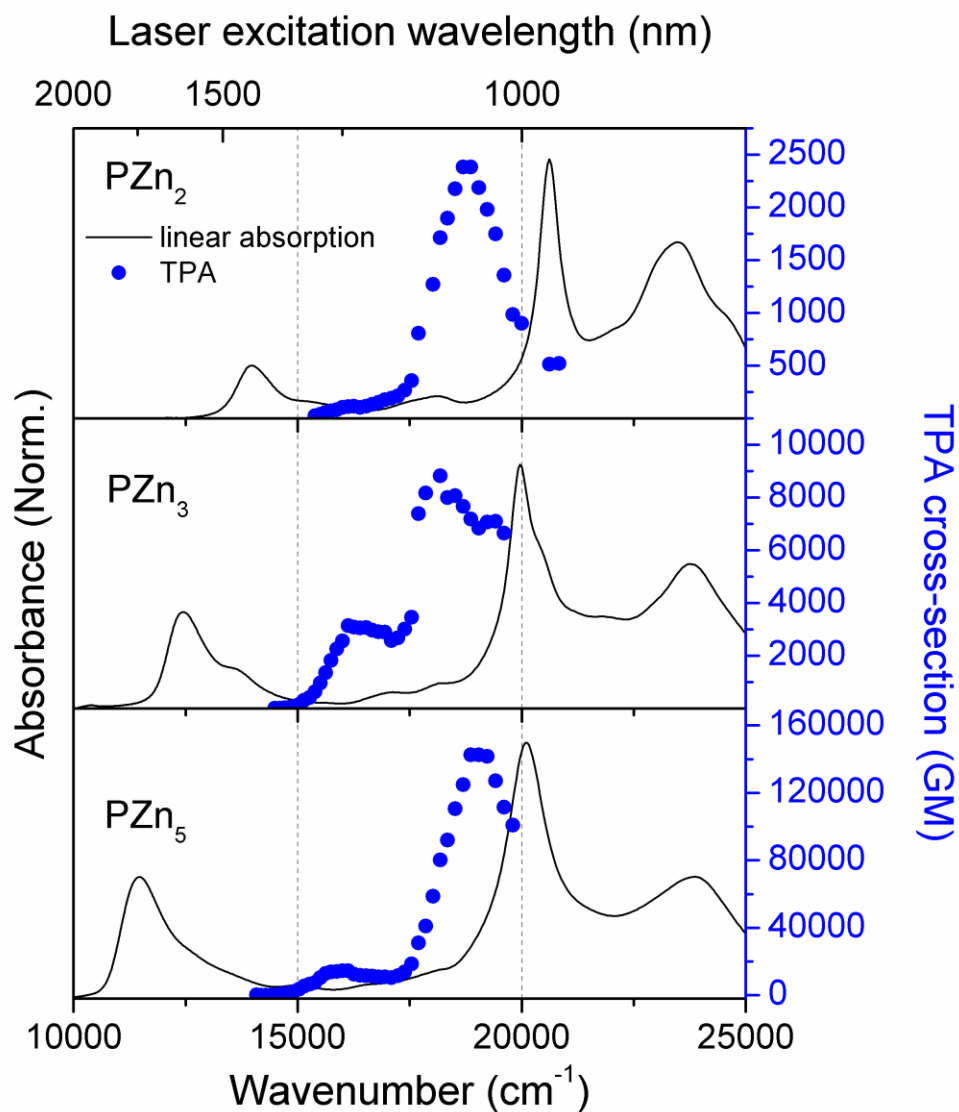


Figure 21. Two-photon absorption cross-sections of PZn_n-based polymersomes on a per chromophore basis in DIW. Power studies were performed to confirm quadratic dependence of fluorescence signal.

One of the benefits of incorporating **PZn_n** NIRFs into the hydrophobic layer of the polymersome is the distribution of NIRFs localized into a small volume defined by the polymersome bilayer. One polymersome containing thousands of porphyrins possess a typical diameter (~100–150 nm) smaller than the diffraction limit of a typical laser beam employed for TPM. For example, the diffraction-limited spot size diameter from $\lambda = 800$ nm light focused by a 1.3 NA objective is $d = \lambda/(2 \text{ NA}) = 310$ nm, and even larger using longer wavelengths (e.g. $d = 420$ nm for $\lambda = 1100$ nm). For this reason, considering TPA cross-section on a per vesicle basis is a valid benchmark for comparison of emissive polymersomes against other emissive entities for two-photon fluorescence applications. TEM images gave mean diameters of 138 nm for **PZn₂**-, 108 nm for **PZn₃**-, and 132 nm for **PZn₅**-based polymersomes (Figure 19 and Table 5), which at a 5 mol% NIRF loading corresponds to 5500, 3000 and 5000 copies of emitter, respectively, within a single polymersome (Table 5).

Table 5. PZn_n copy number per vesicle as a function of vesicle size for a 5 mol% membrane loading.

	Average size (diameter)	Number of emitters ^a
PZn₂	137.6 ± 50.5 nm	5500
PZn₃	108.1 ± 38.1 nm	3000
PZn₅	131.8 ± 68.3 nm	5000

[^aComputations assume a 1-nm² projected area per PBD block composing the polymersome's bilayer membrane.¹³⁹ Average sizes were measured by cryo-TEM images (> 150 vesicles).]

Multiplication of these values by the per chromophore TPA cross-sections, allows TPA cross-sections on a per vesicle basis to be estimated at $\sigma_2 = 1.32 \times 10^7$ GM

(**PZn₂**), 2.64×10^8 GM (**PZn₃**), and 7.15×10^9 GM (**PZn₅**) (Table 4). Despite fluorescence quantum yields of **PZn_n** within the polymersomes membrane being less than 10%, the corresponding two-photon action cross-sections ($\sigma_2\phi$; direct indicator of chromophores' brightness by two-photon excitation) of **PZn_n**-polymersome of 7.92×10^5 GM (**PZn₂**), 1.82×10^6 GM (**PZn₃**), and 1.43×10^7 GM (**PZn₅**) are 1-3 orders of magnitude larger than record-high TPA action cross-section of water soluble QD per particle basis ($\sigma_2\phi \sim 47000$ GM at 700–1000 nm).³⁰ Note again that the typical laser beam used for TPM does not distinguish between single emissive polymersomes (~100 nm in diameter) and single inorganic nano-particles (tens of nm in diameter), thus establishing NIR-emissive polymersomes as a promising two-photon imaging platform that provides unprecedented brightness, chemical stability, excitation and emission wavelength tenability in addition to biocompatibility and biodegradability.

4.2.4 Verification of two-photon excited fluorescence of nano-sized emissive polymersomes under imaging conditions

In our previous work, we studied the effect of laser repetition rate and excitation geometry to two-photon excited fluorescence detection.⁸⁰ While an amplified laser (kHz) is typically employed to characterize TPA cross-section due to its high pulse energy easily achieving high enough intensity to generate two-photon absorption, a Ti:S laser (MHz) is utilized for TPM for fast scanning over large area of specimens. It was discovered that even when linear absorption of chromophores for two-photon excitation at long wavelength is seemingly negligible, linear absorption from thermally excited vibronic state (hot-band absorption) can add a significant linear contribution to the

fluorescence signal under tight-focusing geometry using an objective lens typically employed for microscopy. The observation indicates that even if a pure two-photon signal is confirmed by quadratic power scaling measuring TPA cross-sections using a kHz laser, this does not guarantee the same nonlinearity under a microscope employing a MHz laser. To confirm pure two-photon excited fluorescence under imaging conditions (MHz laser source coupled with objective lenses), we recorded the fluorescence signal of nano-sized **PZn₃**- and **PZn₅**-based polymersomes in a 1 mm cuvette by microscope using 80 MHz laser and 10×/0.25 dry objective lens. We selected $\lambda_{\text{ex}} = 1100$ nm and 1300 nm as excitation wavelengths because the **PZn_n**-based polymersomes' σ_2 maxima at approximately 1100 nm and 1300 nm coincide with two water absorption minima in the NIR-II imaging window.¹⁴⁰

PZn₃-based polymersomes displayed pure two-photon excited fluorescence (confirmed by quadratic power scaling) under 1100 nm excitation providing clear localization of vesicles in the cuvette from the z-depth profile with negligible background signal [Figure 22(A)]. **PZn₅**-based polymersomes, however, showed significant linear background signal of constant magnitude from hot-band linear absorption, independent of sample z position [Figure 22(B)]. Accordingly, despite **PZn₅**-based polymersomes possessing the largest σ_2 among the studied NIR-emissive polymersomes, it is not suitable for two-photon imaging at the ~1100 nm excitation. Another factor to consider is the efficiency of our detection system. The PMT response in our current setup is limited beyond 800 nm, hampering the utility of **PZn₅** that displays

NIR emission peaking at 906 nm. We therefore chose to focus on **PZn₃**-based polymersomes for *in vivo* applications for the next section. Although **PZn₅**-based polymersomes are not a main target for two-photon imaging in this work, the utility of **PZn₅** is still open for future applications with longer wavelength excitation ($\sim 1250\text{--}1300$ nm) targeted to the second TPA peak (1.45×10^6 GM at $\lambda_{\text{ex}} = 1250$ nm), where clean two-photon fluorescence is displayed under imaging conditions (data not shown), circumventing the linear background issue under 1100 nm excitation. In addition, use of a NIR-PMT would improve the two-photon fluorescence detection efficiency of **PZn₅**-based polymersomes ($\lambda_{\text{em}} = 906$ nm) in future work.

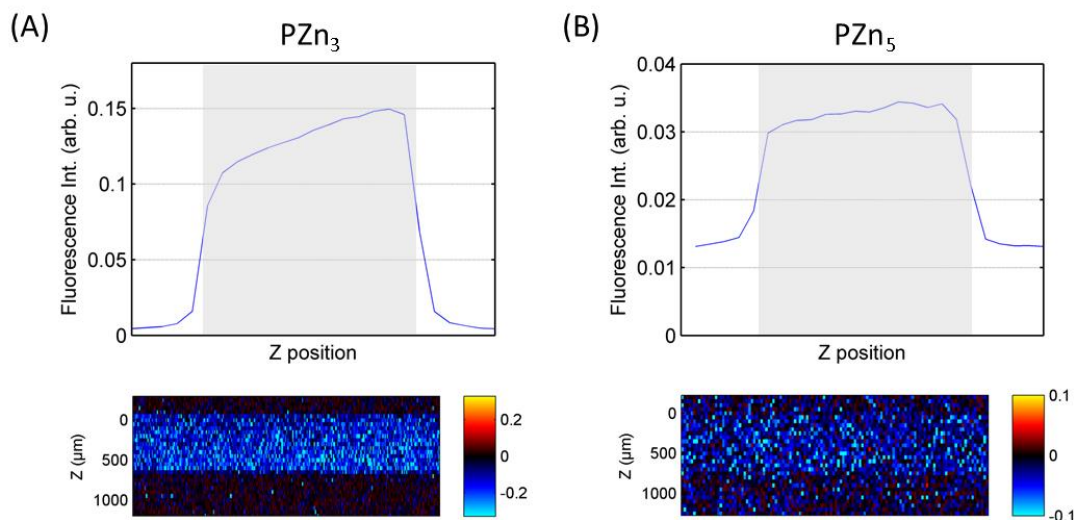


Figure 22. Depth profile of two-photon excited fluorescence of nano-sized 5 mol% (A) PZn₃- and (B) PZn₅-based polymersomes in 1 mm cuvette under a microscope using 10x objective ($\lambda_{\text{ex}} = 1100$ nm, input power = 4 mW for PZn₃-based polymersome and 8 mW for PZn₅-based polymersome, respectively). A z-independent offset observed in PZn₅-based polymersome, which we attribute to linear-excited fluorescence. The power scaling of PZn₅-based polymersomes display a slope of ~ 1.4 while PZn₃-based polymersomes display quadratic dependence to excitation power.

4.2.5 Blood vessel visualization in a window chamber mouse model

The large two-photon action cross-section of nano-sized **PZn_n**-based polymersomes at long NIR wavelengths suggests utility of **PZn_n**-based polymersomes as a two-photon *in vivo* imaging agent in the NIR-II imaging window. Of the **PZn_n** NIRFs studied, **PZn₃**-based polymersomes displayed a brighter two-photon fluorescence than **PZn₂**-based polymersomes, without the linear background problems that **PZn₅**-based polymersome introduced. Therefore, we selected **PZn₃**-based polymersomes for an *in vivo* imaging demonstration. We prepared dorsal window chamber mouse models to demonstrate two-photon *in vivo* application of **PZn₃**-based polymersomes. Window chambers provide a platform to enable acquisition of high-resolution images in animals while maintaining the native tissue environment, and are suitable for direct usage in TPM.¹⁴¹⁻¹⁴² Excitation wavelength of 1100 nm was selected where **PZn₃**-based polymersome exhibit the maximum σ_2 and where one of water absorption local minima (1060–1070 nm)¹⁴³ in NIR-II wavelengths is nearby.

Figure 23 summarizes the results of the dorsal window chamber experiment of a normal mouse injected with **PZn₃**-based polymersomes. A mouse was imaged before and after injection of 140 μ L of **PZn₃**-based polymersome (membrane loaded at 5 mol%) in sterilized PBS at a 5.0 mg/mL polymer concentration (corresponding to 3.4 nmol **PZn₃**) *via* intravenous (i.v) tail vein injection. The mouse was anesthetized and imaged on a home-made window chamber imaging stage coupled with a heating pad to maintain body temperature. Bright field images clearly show vasculatures [Figure

23(A)]. Before polymersome injection we did not detect any structural features in the two-photon fluorescence PMT channel (Figure 24). However, after injection of **PZn3**-based polymersomes, blood vessels became vividly discernible, providing detailed structural and depth information of mouse blood vessels at $\sim 200 \mu\text{m}$ depth from the dorsal skin [Figure 23(B) and Figure 24]. The identical vessel structure observed by bright field imaging can also be found in the two-photon excited fluorescence mode. A more detailed structure of blood vessels can be seen at higher magnifications using a 40 \times water objective with input power of 7.6 mW [Figure 23(C)]. Reconstructed 3-dimensional structures from a set of z-stack images provides a clear view of the location and network of individual vasculature $\sim 200\text{-}\mu\text{m}$ deep from the skin surface [Figure 23(D)].

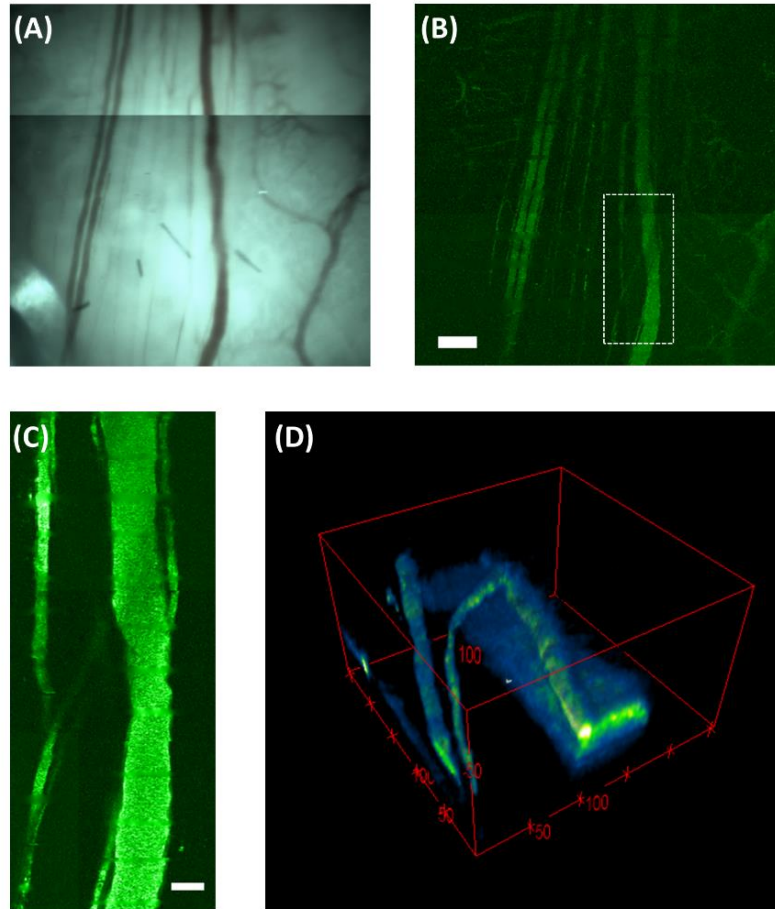


Figure 23. Blood vessel imaging 2 hrs after tail vein injection of PZn₃-based polymersomes. (A) Stitched bright field microscopy images of a part of the dorsal window chamber. (B) Stitched two-photon excited fluorescence images of the corresponding area using low magnitude objective (10×/0.25) under 1100 nm excitation. Scale bar = 200 μm. Input power = 12.8 mW. (C) Stitched two-photon excited fluorescence images using an objective of high magnification (40×/0.8W) for the region marked with a white box in (B). Scale bar = 50 μm. Input power = 7.6 mW. The depth of the imaged region is ~200 μm from the surface. (D) Reconstructed 3D view of blood vessels from individual z-stack images sampled every 2 μm (40×/0.8W objective). Images were acquired at 256×256 or 512×512 pixel size. Two-photon excited fluorescence images were post-processed to reduce the stripe artifacts from mouse breathing (see Experimental section).

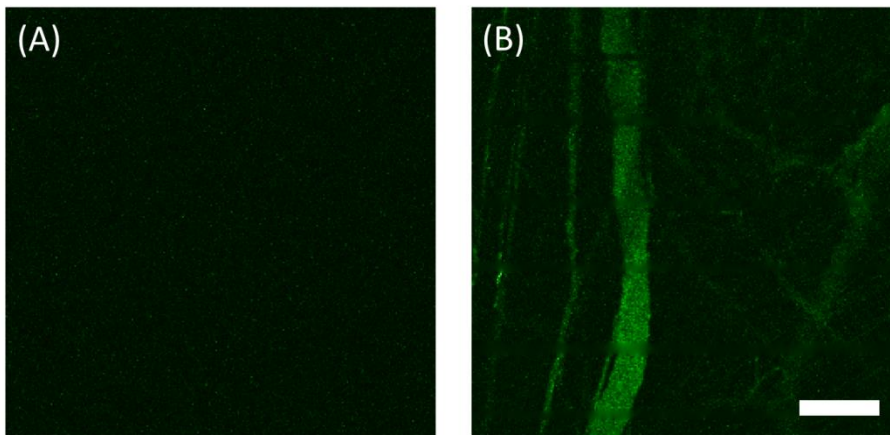


Figure 24. Comparison of two-photon excited fluorescence images ($\lambda_{\text{ex}} = 1100 \text{ nm}$, $P_{\text{in}} = 12.7 \text{ mW}$) from dorsal window chamber of a control mouse before (A) and 2 hrs after (B) tail vein injection of PZn₃-based polymersomes. The identical intensity scale was applied for two images. Scale bar = 200 μm . Post processing was applied for (B) to lessen stripe artifacts from mouse breathing.

The same mouse was imaged again 24 hrs after PZn₃-based polymersome injection, and showed that most of the signal had disappeared this time (Figure 25). To compare the decrease in signal level over time, SBR was calculated by measuring the signal in two regions (marked by white rectangular boxes in Figure 25) representing blood vessel and background from two images obtained 2-hr and 24-hr time points. SBR at 2 hrs after PZn₃-based polymersome injection was 13.0 dB, which dropped to 5.36 dB at 24 hr post-injection corresponding to an approximate 5-fold signal decrease.

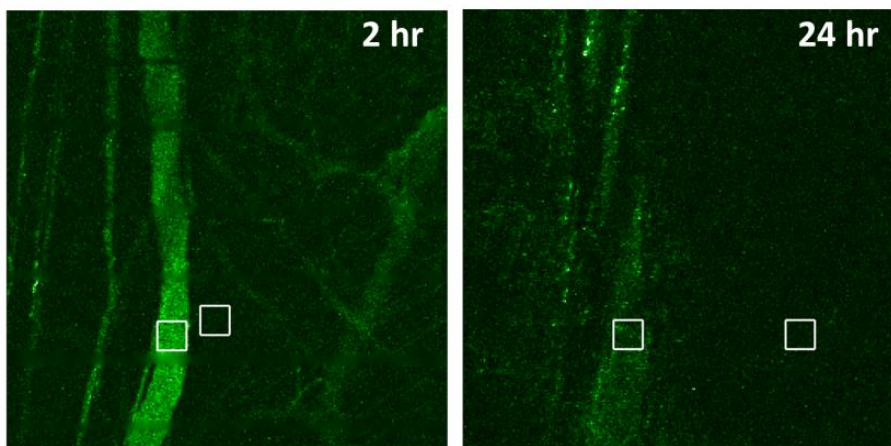


Figure 25. Comparison of two-photon excited fluorescence images from a dorsal window chamber in a control mouse over time. Blood vessel images were obtained at 2 hr and 24 hr time points after PZn₃-based polymersome injection. Input power was 12.8 mW through a 10×/0.25 objective lens. The depth of the imaged region is ~200 μm from the surface. Images were acquired at a 256×256 pixel size. Two white rectangular boxes indicate the regions selected to calculate signal-to-background ratio. We applied post processing for two-photon excited fluorescence images to lessen the stripe artifacts arising from mouse breathing.

Previously, it has been shown that PEO-based polymersomes are cleared from blood circulation by the spleen and liver.¹⁴⁴ To locate cleared **PZn3**-based polymersomes, the mouse was sacrificed 26-hr after polymersome injection, and the spleen, liver and kidneys were collected in PBS. The intact organs were imaged at 1100 nm excitation (Figure 26). Most of polymersome signal was observed in the spleen and liver (input power was 12.8 mW with a 10× objective and 7.6 mW for 40× objective, respectively at specimen) while little signal was detected in the kidneys, consistent with the previous finding.¹⁴⁴ We hypothesize that the localization of the particles in the spleen was mostly present in the red pulp of the organ that also contains a large population of red blood

cells. In the liver, however, the particles presented a sparse localization across the parenchymal cells of the liver.

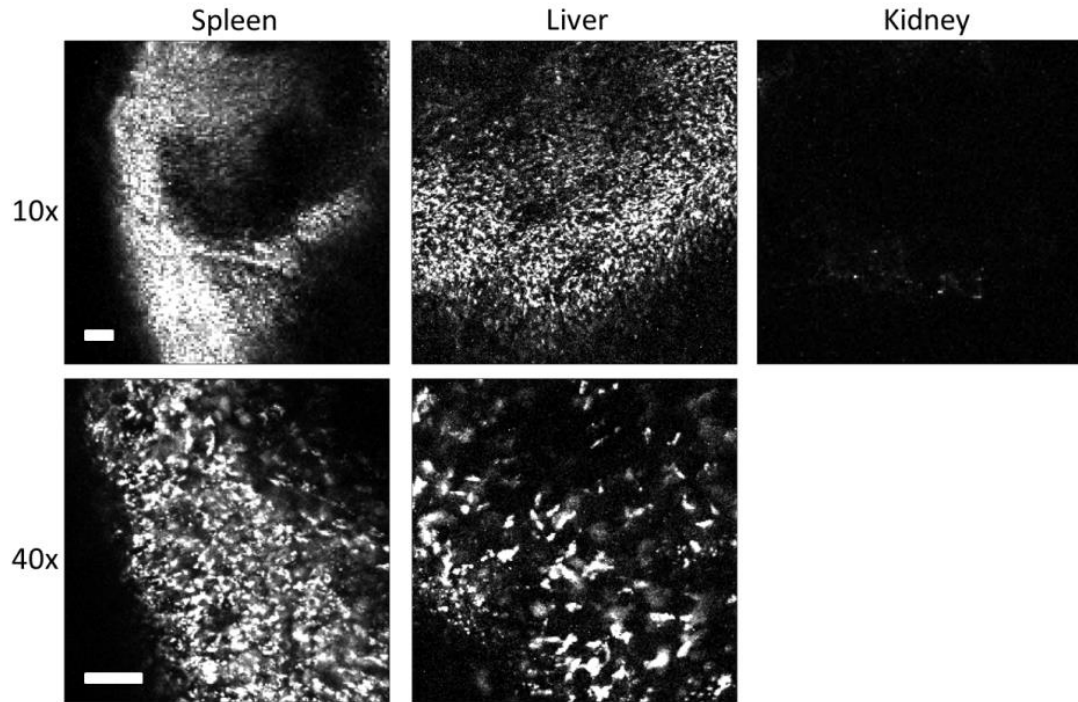


Figure 26. Two-photon excited fluorescence images of excised spleen, liver, and kidney using 1100 nm excitation. The organs were excised 26 hr after PZn₃-based polymersome injection. The top images were obtained using 10×/0.25 objective (scale bar = 100 μ m) and the bottom images were obtained using 40×/0.8W objective (scale bar = 50 μ m). The same intensity scale was used for 10× liver and 10× kidney images for direct comparison of the signal from PZn₃-based polymersomes. Input power was 12.8 mw for 10× objective and 7.6 mW for 40× objective.

4.2.6 4T1 tumor detection via the EPR effect

One possible application of nanosized NIR-fluorescent polymersomes is in cancer diagnosis, by harnessing the EPR effect for passive accumulation in tumor tissue.¹³⁸ To demonstrate this, we prepared a 4T1 breast cancer model in mice ($N = 2$) with a dorsal window chamber, by injecting 10 μL of 4T1 cells in the window chamber. Once tumors were palpable, after 4–5 days, **PZn₃**-based polymersomes (membrane loaded at 5 mol%) were administered by tail vein injection (140 μL , corresponding to 3.4 nmol **PZn₃**) and the mice were imaged at 7-hr and 36-hr time points (Figure 27). Analogous to the control mice, blood vessels were observed clearly at 7 hrs post-injection (data not shown), but after 36 hrs, the signal was greatly diminished as the polymersomes were cleared from circulation. The tumor region, identifiable in bright field images by abnormally shaped blood vessels, could be observed in the two-photon fluorescence channel after 36 hrs due to passive accumulation of **PZn₃**-based polymersomes. Crucially, throughout all experiments, mice did not show any abnormal changes in feeding and behavioral habits up to 2 weeks after polymersome injection. The bright fluorescence signal from **PZn₃**-based polymersomes excited at 1100 nm using both high and low NA objectives demonstrates the potential of TPM using a **PZn_n**-based polymersome imaging platform for not only the detailed visualization of vasculatures or individual tumors, but for a high resolution assessment of a tumor profile over large areas.

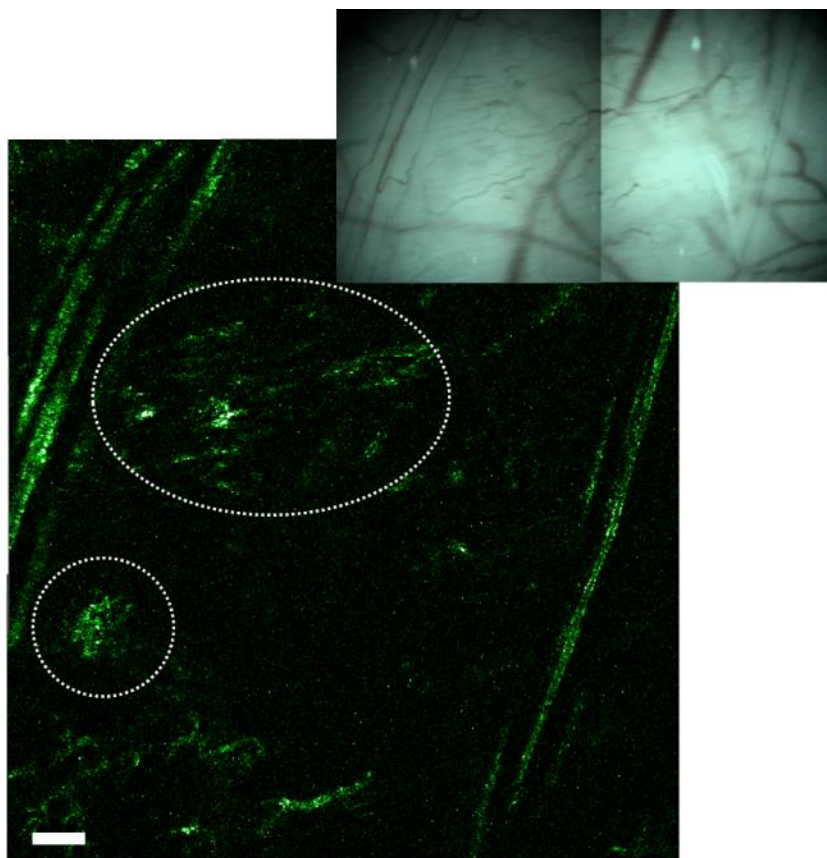


Figure 27. Stitched bright-field and two-photon excited fluorescence images (10×/0.25 objective) of the dorsal window chamber in a tumor-bearing mouse 36 hrs after PZn₃-based polymersome injection. Tumor regions highlighted by accumulated PZn₃-based polymersomes are indicated by dotted circles. Input power was 12.7 mW. Scale bar = 200 μm.

4.3 Conclusion

NIR-emissive polymersomes incorporating *meso*-to-*meso* ethyne-bridged (porphinato)zinc(II) oligomers (PZn_n) are nanometer-sized soft materials for diagnostic and therapeutic applications. We have characterized the quantum yields and TPA cross-sections of PZn_n in OB18 polymersomes and determined them to be the brightest entities (up to $\sigma_2\phi = 1.43 \times 10^7$ GM) in the NIR-II wavelength region reported to date; 2-3 orders of magnitude higher than that of semiconductor quantum dots. We demonstrated key

proof-of-principle experiments using **PZn₃**-based polymersomes for *in vivo* two-photon excited fluorescence imaging in mice, allowing visualization of blood vessel structure at cellular resolution, and identification of tumor tissue *via* the EPR effect. Our study complements previous work demonstrating the utility of emissive polymersomes by one-photon excitation (*e.g.* drug delivery and dendritic cell targeting); the superb two-photon excited brightness per single particle ($\sigma_2\phi \sim 10^5\text{--}10^7$ GM) under NIR-II wavelength range excitation shows these materials are ideal for *in vivo* imaging applications. The synthetic nature of polymersomes enables us to formulate fully biodegradable, non-toxic and surface-functionalized polymersomes of varying diameters, making them a promising and fully customizable multimodal diagnostic nano-structured soft-material for deep tissue imaging at high resolutions.

4.4 Experimental

4.4.1 Materials

Poly(ethylene oxide)-block-poly(butadiene) co-polymer (PEO₈₀-PBD₁₂₅, denoted OB18) was purchased from Polymer Source, Inc. (Montreal, Quebec, Canada). Ethyne-bridged bis-, tris-, and pentakis(porphinato)zinc(II) (**PZn₂**, **PZn₃**, and **PZn₅**, respectively) arrays were synthesized and characterized as described previously.^{47, 52} Phosphate buffered saline (PBS) tablets were purchased from Sigma Aldrich (St. Louis, MO) and made up as per the instructions in MilliQ water. Chloroform (HPLC grade) was purchased from Fisher Chemicals (Pittsburgh, PA).

4.4.2 Polymersome synthesis

Polymersome synthesis was carried out using the thin-film hydration method as previously described.⁵⁸ A CHCl₃ solution of OB18 and **PZn**, NIRF at a 100:5 molar ratio was spotted onto a roughened Teflon plate and allowed to evaporate to form a uniformly coated surface. After residual solvent removal under high vacuum for >24h, 1X PBS buffer (285 mOsm, pH 7.40) or MilliQ water was added to form a final polymersome concentration of 12.5 mg/mL polymer. The films were incubated at 60 °C for 24 h, followed by 90 minutes of sonication in a bath sonicator. Nanoscale, unilamellar polymersomes were obtained by carrying out ten freeze-thaw cycles, by alternatively placing the samples in liquid N₂, followed by a 5 minute sonication in a water bath at 60 °C; further extrusion steps were not required. Polymersome morphology was characterized by cryogenic transmission electron microscopy and dynamic light scattering techniques. For in vivo studies, the polymersomes were sterilized by extrusion through a 0.2 μm filter at 60 °C.

4.4.3 Cryogenic Transmission Electron Microscopy (Cryo-TEM)

3 μL of sample was deposited on a 300 mesh Lacey Carbon copper grid (average grid hole size 63 μm, Ted Pella, Inc.), blotted with filter paper set at a -3 mm offset for 3 seconds, before immediate vitrification in liquid ethane using a Vitrobot (FEI company, Netherlands). Frozen grids were transferred to an FEI Tecnai G² Twin transmission electron microscope using a Gatan 626 cryo-holder. Images were recorded at an accelerating voltage of 80 kV using a Gatan 724 multiscan digital camera. The average

polymersome diameter and size distribution was subsequently measured manually using the measuring tool in ImageJ. Particle diameters are quoted as a mean of a minimum of 150 measurements plus or minus the standard deviation.

4.4.4 Dynamic Light Scattering

Dynamic light scattering was performed using a DynaPro Titan (Wyatt Technology Inc.) using a vertically polarized laser at 829 nm. Samples were prepared to a 0.01–0.05 mg/mL concentration in MilliQ water or isotonic buffer (750 μ L) and measured at 298 K over 20 scans at 5 seconds each. Data was analyzed using the inbuilt DYNAMICS software.

4.4.5 Linear and nonlinear optical property characterization

Electronic linear absorption spectra were recorded on a spectrophotometer (Shimadzu, PharmaSpec UV1700) in 1 cm quartz optical cells. Emission spectra were recorded on a fluorescence spectrophotometer (Edinburgh, FLSP920).

Two-photon absorption cross-section spectra were measured using standard TPEF (two-photon excited fluorescence) method.⁵ Excitation laser pulses were generated using a tunable optical parametrical amplifier (OPA; Light Conversion, TOPAS-C) with pulse widths of typically 100–120 fs. For excitation, a 1 cm path length quartz cell was placed in a weakly focused beam (12 mrad divergence angle) using a lens with 300 mm focal length. A loosely focused beam was used to avoid linear contribution from the out-of-focus region.⁸⁰ Typical excitation power was kept below ~5 mW. Emission was collected at 90° with an amplified photodiode (Thorlabs, PDA36A) through an

appropriate set of short-pass filters to reject scattered excitation light. A lock-in amplifier (Stanford Research Systems, SR830) was used to measure the fluorescence intensity. We obtained the two-photon absorption cross section (σ_2) of chromophores relative to the standard Styryl 9M (Sigma-Aldrich) in chloroform in the wavelength range of 900 – 1500 nm using^{5, 7}

$$\sigma_{2, sample} = \frac{[C]_{S9M} \eta_{S9M} \phi_{S9M} n_{S9M} \langle F \rangle_{sample}}{[C]_{sample} \eta_{sample} \phi_{sample} n_{sample} \langle F \rangle_{S9M}} \sigma_{2, S9M}$$

where $[C]$ is the concentration, η the collection efficiency of the system, ϕ the fluorescence quantum yield, n the refractive index of the solvents and $\langle F \rangle$ the intensity of the detected fluorescence. The emission intensity of the polymersomes as a function of excitation power was acquired to confirm quadratic dependence.

4.4.6 Skinfold window chamber and cancer model

Murine mammary carcinoma cells 4T1 were cultured in RPMI 1640 supplemented with 10% fetal bovine serum (FBS) and 1% antibiotic/antimycotic. Cells were harvested using 0.25% Trypsin EDTA solution, rinsed 3 times with sterile PBS and resuspended in serum-free RPMI 1640. The mice were implanted with dorsal skinfold window chambers (APJ Trading Company, Inc., Ventura, CA) as described elsewhere.¹⁴² Briefly, the mice (~12 weeks of age; 22-30 g) were anesthetized by intraperitoneal injection of ketamine (100 mg/kg) and xylazine (10 mg/kg). The dorsal skin was perforated in three locations to accommodate the screws of the titanium chamber. A circular region of ~8-10 mm of the facing skin was excised for further placement of the

window glass. The front and rear pieces of the dorsal chamber were screwed together from the opposite sides of the skin. A sterile circular cover glass was placed over the window and kept in place with a retaining ring. Sterile saline solution was used to avoid bubble formation between the skin where the cells were injected and the glass slide. All *in vivo* procedures were conducted under a protocol approved by the Duke Institutional Animal Care and Use Committee.

4.4.7 Two-photon imaging

Two-photon excitation microscopy was performed with a custom-built laser scanning microscope equipped to detect traditional multiphoton signals and confocal reflectance. A Ti:Sapphire mode-locked laser (Coherent, Chameleon) operating at a repetition rate of 80 MHz, with a wavelength in the near-IR and pulse duration of roughly 150 fs, was used to pump an optical parametric oscillator (Coherent, MIRA-OPO), with an output in the near-IR of a similar pulse duration. The beams were focused into the specimen by a microscope objective (Olympus 10×/0.25 or Olympus 40×/0.8W) and collected by the same objective. Fluorescence light was reflected by a dichroic mirror (Thorlabs, DMLP900 long pass) and detected with a photomultiplier tube (Hamamatsu, R3896), filtered with a filter set (Thorlabs, FEL0600 and FES0950) to reject residual excitation light. The photomultiplier current was amplified with a transimpedance amplifier (Terahertz Technologies Inc., PDA 700) and recorded using a data acquisition (DAQ) board (National Instruments, PXI-6259). Reflected light, passed back through the dichroic mirror, was descanned by the galvos, reflected by a glass

coverslip, focused by a 30-cm lens into a confocal iris, and detected with an amplified silicon photodiode (Thorlabs, PDA100A). Images were typically acquired at 256×256 or 512×512 pixel resolution with pixel dwell time of ~50–200 μ s. Optical power through the objective was estimated by measuring with a power meter before the entrance to the objective and multiplying by the transmissivity of the objective at the desired wavelength.

4.4.8 Image analysis

The acquired images exhibited periodic dark horizontal stripes as an artifact from the breathing motion of the mouse under anesthesia. For z-stacks, this artifact was removed by using ImageJ to perform an isotropic 3D median filter, with a radius of two pixels. For individual frames, the stripes were removed by using MATLAB to identify the affected rows in a semi-automated fashion and to inpaint those rows with the *roifill* function.

5. Femtosecond Pulse Train Shaping Improves Two-photon Excited Fluorescence Measurements

5.1 Introduction

Two-photon excited fluorescence (TPF) microscopy has become an extraordinarily valuable tool to extend the utility of optical imaging, especially in biomedical applications.^{3-4, 21, 24, 30, 63, 145} It takes advantage of intrinsic three-dimensional localization (since the signal is predominantly produced at the focus), and the deeper penetration depths and lower photo-induced damage associated with near-infrared (NIR) excitation (as opposed to single-photon UV excitation). However, a major challenge faced by this technique is that most molecules produce very little TPF.^{30, 68} Typical two-photon absorption (TPA) cross-sections of “good” two-photon absorbers are typically 10-100 GM (Goeppert-Mayer, 1 GM = 1×10^{-50} cm⁴ s photon⁻¹). At the intensities suitable for *in vivo* imaging, this implies that only about one photon in a million is taken up by the desired nonlinear process.

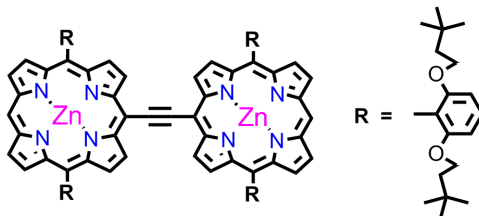
This challenge motivates the development of novel chromophores with large NIR TPA cross-sections, typically from strong π -conjugation and enhanced transition dipole strength. Multiple examples of NIR fluorophores having TPA cross-sections exceeding 10³ GM have now been reported.^{75-76, 79, 81, 108, 146-148} Highly conjugated, *meso*-to-*meso* ethyne- and butadiyne-bridged (porphinato)zinc(II) oligomers are promising NIR two-photon imaging agents due to their outstanding chemical and photochemical stabilities, excellent biocompatibility, and high fluorescence quantum yields.^{47-52, 58-59, 83-86,}

^{104, 149} These chromophores manifest exceptional electronic structural characteristics that include low energy π - π^* excited-states that are polarized exclusively along the long molecular axis, intensely absorbing $S_0 \rightarrow S_1$ (Q-state) and $S_1 \rightarrow S_n$ transitions that extend deep into the NIR spectral region, and unusually large polarizabilities. The $S_0 \rightarrow S_2$ (Soret, B-state) absorption manifold of *meso-to-meso* ethyne-bridged (porphinato)zinc(II) oligomers spans a broad spectral domain (~360-550 nm) and possesses absorption extinction coefficients that exceed $10^5 \text{ M}^{-1}\text{cm}^{-1}$; the full-widths at half-maximum (FWHM) of this manifold increase with increasing conjugation length, and range over 3000-5500 cm^{-1} .^{48-49, 51-52, 58-59, 83-84, 86} In addition, other types of modified porphyrin monomers and oligomeric porphyrins, and their self-assembled structures, have been noted to possess large TPA cross-sections.^{72, 106, 124, 150}

While the TPA cross-section can be measured directly,¹⁵¹⁻¹⁵³ for applications of TPF microscopy the appropriate figure of merit is TPA times the quantum yield, which is commonly measured by direct observation of the fluorescence.⁵ Spectroscopic characterization of TPA cross-sections has most commonly been performed using low-repetition rate amplified laser systems (kHz). However, for the ultimate application (imaging), unamplified modelocked lasers with roughly 100 MHz repetition rate are preferred in order to scan large spatial regions in a reasonable time. A modelocked laser was used directly to evaluate the TPA cross-sections of several monomeric (porphinato)zinc(II) fluorophores and multiple, exemplary oligomeric *meso-to-meso*

ethyne- and butadiyne-bridged (porphinato)zinc(II) chromophores, but the TPA signal was overwhelmed by one-photon fluorescence.⁸²

In this study, we measure the laser-induced fluorescence of a meso-to-meso ethyne-bridged (porphinato)zinc(II) dimer, bis[(5,5'-10,20-bis[3,5-bis(3,3-dimethyl-1-butyloxy)phenyl]porphinato)zinc(II)]ethyne (DD, Scheme 3), using both a regenerative amplifier (1 kHz repetition rate) and a modelocked oscillator (76 MHz) at $\lambda=800$ nm. We compare the effect of repetition rate, excitation geometry, and excitation intensity on multiphoton fluorescence measurements. The absorption spectrum, shown in Figure 28, suggests that one-photon absorption should be negligible at this wavelength – yet we find a linear contribution to DD's fluorescence and substantial differences in the fluorescence power scaling between low- and high-repetition rate excitation (Figure 29).



Scheme 3. Molecular structure of DD

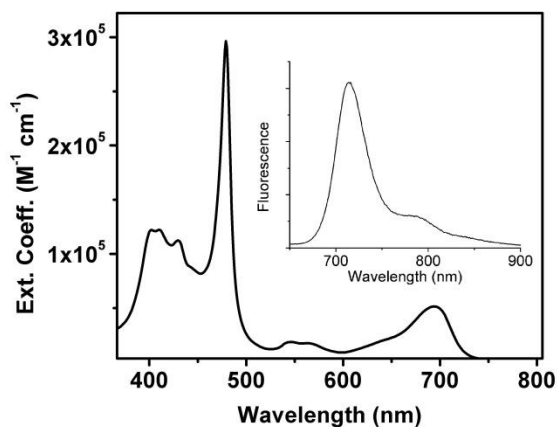


Figure 28. Linear electronic absorption and emission (inset) spectra of DD in THF solvent.

For 1 kHz excitation, DD shows a linear intensity scaling (a slope of 1 in the log-log plot) for low excitation intensities ($\leq 10^{27}$ photons $\text{cm}^{-2} \text{s}^{-1}$), increasing to 1.8 in the range of $\sim 10^{29}$ photons $\text{cm}^{-2} \text{s}^{-1}$ (Figure 29). Intensities higher than $\sim 10^{30}$ photons $\text{cm}^{-2} \text{s}^{-1}$ could not be used as such intensities marked the onset of white light generation. For 76 MHz excitation at 800 nm, DD fluorescence emission displays an almost linear response over the entire intensity range, even at intensities higher than the 1 kHz white light generation threshold. In contrast, Rhodamine 6G (R6G) displays only two-photon absorption at $\lambda=800$ nm in the range of powers ($10^{27} - 10^{30}$ photons $\text{cm}^{-2} \text{s}^{-1}$) we studied; however, at $\lambda=630$ nm (still far to the red of its linear absorption peak) again significant deviations from intensity-squared scaling are observed with modelocked lasers. These data highlight that even though 76 MHz excitation better replicates the experimental conditions of the ultimate imaging application, the possibility of signal contamination

due to confounding linear fluorescence contributions should always be considered when high-repetition rate lasers are utilized in TPA cross-section determinations.

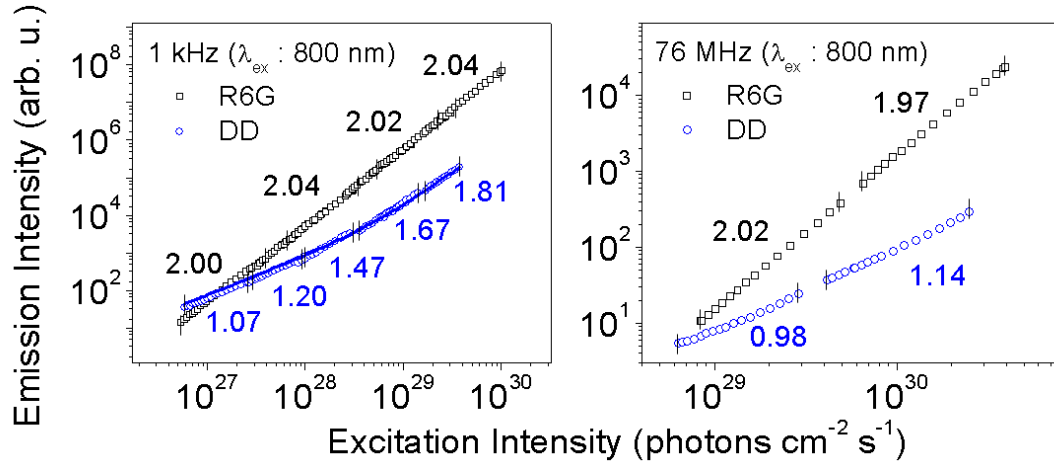


Figure 29. Logarithmic plots of the emission intensity of DD and R6G as a function of peak excitation intensity, $I_{\text{peak}} = \left(2 / \pi w_0^2\right) \left(P_{\text{avg}} / \sqrt{\pi} \tau_p f_p\right) (1 / h\nu)$ where w_0 is the beam waist, P_{avg} is the average power (in W), τ_p is the pulse duration (at 1/e of the temporal intensity), and f_p is the repetition rate; for comparison, 10^{28} photons $\text{cm}^{-2} \text{s}^{-1}$ at $\lambda=800$ nm corresponds to $2.5 \times 10^9 \text{ W cm}^{-2}$. The numbers in the plots indicate the local power scaling within the indicated range (the slope in the log-log plot). The symbols are measured data; the solid blue line in the left panel is a nonlinear least-squares fit to the sum of a linear and a quadratic component.

We show that the different fluorescence power scaling of DD for 1 kHz and 76 MHz excitation arises from the significantly different focusing geometries of the two excitation laser systems: the modelocked system employs a tight focus (and subsequent divergence of the beam) to achieve large enough ($> 10^{25}$ photons $\text{cm}^{-2} \text{s}^{-1}$) peak intensities, while with the kHz system employs a very weak focus (a 140 μm beam diameter at the sample position, contrasting the 2.0 μm focal point beam diameter for 76 MHz excitation). We then introduce a novel pulse train shaping method which attenuates the

linear fluorescence contribution. As a result, fast repetition rate laser excitation sources can be used to determine TPA cross-sections under conditions identical to that used for TPF microscopy.

5.2 Result and discussions

5.2.1 Absorption and emission spectra of DD

DD manifests a $S_0 \rightarrow S_1$ (x-polarized Q-state) absorption maximum at 695 nm ($\epsilon \sim 5.0 \times 10^4 \text{ M}^{-1} \text{ cm}^{-1}$) and $S_0 \rightarrow S_2$ manifold absorption maxima at 401 nm ($\epsilon \sim 1.3 \times 10^5 \text{ M}^{-1} \text{ cm}^{-1}$) and 479 nm ($\epsilon \sim 3.0 \times 10^5 \text{ M}^{-1} \text{ cm}^{-1}$) (Figure 28); its fluorescence emission band maximum is centered at 713 nm, and its fluorescence quantum yield was determined to be identical to that previously reported ($\phi_F = 16\%$ in THF solvent).⁷⁵ Two-photon excitation at 1000 nm and one-photon excitation at 510 nm yield identical fluorescence spectra despite fundamentally different selection rules for one- and two-photon absorption, confirming that the final emissive state of DD is the low lying S_1 state regardless of excitation conditions.^{50, 84}

5.2.2 Conventional multiphoton emission measurements

The dissimilarity of the observed slopes of DD emission intensity upon excitation intensity as a function of these 1 kHz and 76 MHz excitation sources (Figure 29) can be explained by differences in the excitation geometry. The loosely focused beam ($z_R \geq l$ where z_R is the Rayleigh range and l is the optical path length of the sample; in our 1 kHz excitation condition $z_R = 1.8 \text{ cm}$ and $l = 1 \text{ cm}$) in the 1 kHz setup leads to a nearly uniform (high intensity) excitation distribution along the 1 cm cuvette. On the other

hand, tight focusing ($z_R \ll l$; in our 76 MHz excitation condition $z_R = 4.1 \mu\text{m}$ and $l = 1 \text{ cm}$) provided by the 76 MHz setup generates intensities high enough for nonlinear excitation only at a small focal volume ($\sim 26 \mu\text{m}^3$), while the lower intensities in the out-of-focus regions still contribute to one-photon absorption. This behavior was confirmed by a confocal-type measurement (Figure 30) in which the fluorescence is focused through an iris placed between the sample and the detector (partial rejection of out-of-focus light increased the slope from 1.18 to 1.41 in the log-log plot of emission intensity vs. excitation intensity in the range of $\sim 10^{30}$ photons $\text{cm}^{-2} \text{s}^{-1}$). Note that the slope is still not quadratic because the apertured detection range is still much larger than the Rayleigh length in the cuvette.

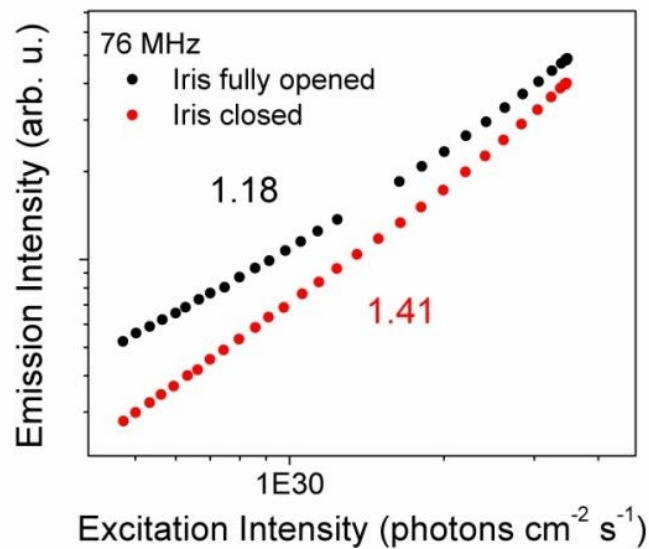


Figure 30. Logarithmic plot of the emission intensity of DD as a function of excitation intensity with a confocal-type measurement (black dots : iris fully opened, red dots : iris closed) using the 76 MHz setup ($\lambda_{\text{ex}} = 800 \text{ nm}$). The respective power scaling is indicated in the graph.

5.2.3 Estimation of relative linear and nonlinear fluorescence for weak and strong focusing

We further estimated the ratio between one- and two-photon contributions for the different focusing geometries used in the 1 kHz and 76 MHz case. We assume that the spatial dependence of one- and two-photon fluorescence is described by

$$F(\vec{r}) = a_1 I(\vec{r}) + a_2 I(\vec{r})^2, \text{ where } a_1 \text{ and } a_2 \text{ are sample-dependent constants. Integrating}$$

the linear term over the length of the cuvette yields a total fluorescence of

$$F_{\text{lin}} = \frac{\pi}{2} a_1 I_0 w_0^2 L, \text{ where } I_0 \text{ is peak intensity, } w_0 \text{ the focal radius, and } L \text{ the cuvette}$$

length. The quadratic contribution is $F_{\text{quadr, kHz}} = \frac{\pi}{2} a_2 I_0^2 w_0^2 L$ if the Rayleigh length z_R is

much longer than the cuvette length (weak focus), or $F_{\text{quadr, MHz}} = \frac{\pi^2}{4} a_2 I_0^2 w_0^2 z_R$ in the

opposite case (strong focus). For weak focusing the intensity where one- and two-photon

events contribute equally is $I_{\text{bal}} = a_1/a_2$, which we estimate from the kHz data in Fig. 2 to

$I_{\text{bal}} = 6.4 \times 10^{28}$ photons $\text{cm}^{-2} \text{s}^{-1}$ [where a slope of 1.5 is manifest in the logarithmic plot of

the emission intensity as a function of peak excitation intensity; Figure 29 (left)] by

nonlinear least-squares fitting to the sum of a linear and a quadratic component. For the

strong focusing case $I_{\text{bal}} = (a_1/a_2)L/(\pi/2 z_R)$. For a Rayleigh length of 4 μm in the MHz case

we expect a shift of I_{bal} by a factor of about 1,600 to $I_{\text{bal}} \approx 1.0 \times 10^{32}$ photons $\text{cm}^{-2} \text{s}^{-1}$, a

number consistent with our data (even though we could not measure at such a high

intensity).

5.2.4 Hot-band model of linear absorption

With excitation at 800 nm and fluorescence shortpass filters at 700 nm, linear absorption from the electronic-vibronic ground state cannot produce a detectable emission signal. For a related conjugated multiporphyrin dimer it was noted that absorption from hot vibronic states (hot-band absorption) could contribute to linear absorption.^{74, 100} We confirmed this effect to be the cause of the one-photon absorptive contribution evident in the log-log plots of DD emission intensity vs. excitation intensity (Figure 29) by cooling down our sample to 77 K (Figure 31). The left panel of Figure 31 compares the power scaling for DD at room temperature and at 77 K measured with the 1 kHz setup. While at room temperature we observed a combination of linear and nonlinear absorption, at 77 K a purely quadratic dependence was observed. For low excitation intensities the hot-band contributions dominate over the quadratic contributions at room temperature. In contrast, at low temperature the hot-band contributions are strongly suppressed and the quadratic contributions remain. At higher excitation intensities, the emission intensity at 77 K is slightly higher than at room temperature; we attribute this to reduced nonradiative decay process at the low temperature. With the high-repetition rate setup, power scaling study at 77 K [Figure 31 (right)] also shows a strong suppression of the hot-band absorption contributions, yet some linear contributions still remain. These residual linear contributions could originate from light-induced local heating in the solid phase.

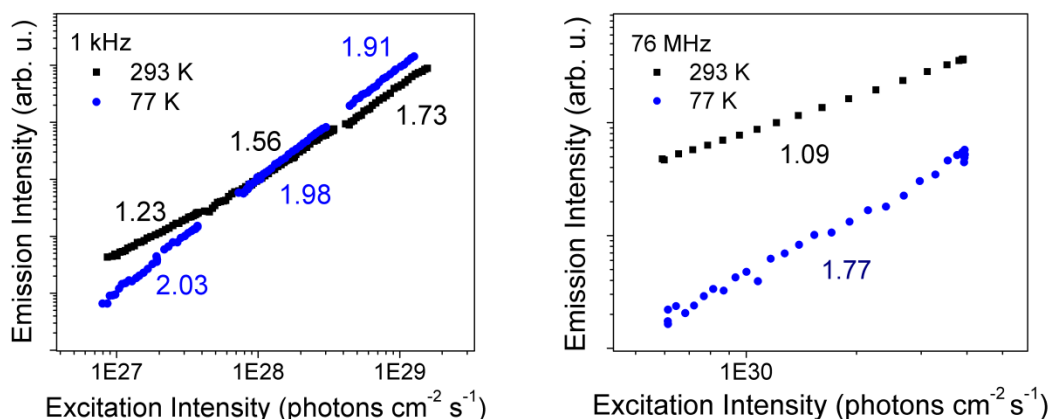


Figure 31. Logarithmic plot of the emission intensity of DD as a function of excitation intensity with the 1 kHz setup (left) and 76 MHz setup (right) at room temperature and 77 K ($\lambda_{\text{ex}} = 800$ nm). The numbers on each data set indicate the local power scaling (the slope in the log-log plot).

Hot-band absorption can be reduced by moving the excitation wavelength further away from one-photon resonance. To probe the balance between linear and nonlinear contributions as a function of excitation wavelength, we performed power studies on DD with longer wavelengths (840 – 960 nm) with the 80 MHz setup and 950 nm with the 1 kHz setup. For longer wavelength excitation the balance shifts more towards nonlinear fluorescence. While purely quadratic dependence was observed in DD at 950 nm excitation with 1 kHz setup, even for 960 nm excitation a linear contribution remains (slope of 1.6) with the 80 MHz setup. That is due to the fact that while the hot-band one-photon transition probability decreases by about 3 orders of magnitude when tuning from 800 nm to 900 nm, the two-photon cross-sections also decreases from ~ 2000 GM to a few tens of GM. For MHz setup, interestingly, neither cooling nor excitation further from resonance (> 250 nm detuning from the $S_0 \rightarrow S_1$

absorption band maximum at 695 nm) could eliminate the one-photon absorptive contribution to DD emission intensity observed as a function of increasing excitation intensity. These temperature- and wavelength-dependent power studies clearly indicate that hot-band absorption adds a significant linear contribution to the fluorescence signal.^{5, 74, 100} This effect is especially pronounced at room temperature for strong focusing geometries (NA 0.25 objective lens in our experiment) — conditions typically encountered in conventional multiphoton fluorescence imaging.

Even in R6G dominant linear emission can be generated when the excitation wavelength is tuned closer to the linear absorption peak. For 630 nm excitation, which is far from the linear absorption peak (Figure 32), an essentially linear intensity scaling is observed for the intensity range of ($10^{28} - 10^{29}$) photons $\text{cm}^{-2} \text{s}^{-1}$ with the 80 MHz setup (Figure 33). It is worth recalling that R6G lases as much as 80 nm to the blue of this point, consistent with very weak absorption. The linear intensity scaling in this common two-photon chromophore suggests that the competition between hot-band one-photon absorption and two-photon absorption under strong focusing geometry is universal for chromophores. Accordingly, a low-repetition rate laser (i.e. employing weak focusing geometry) is better suited for TPEF characterization of a broad range of chromophores since it avoids undesirable linear emission contribution under the conventional excitation condition.

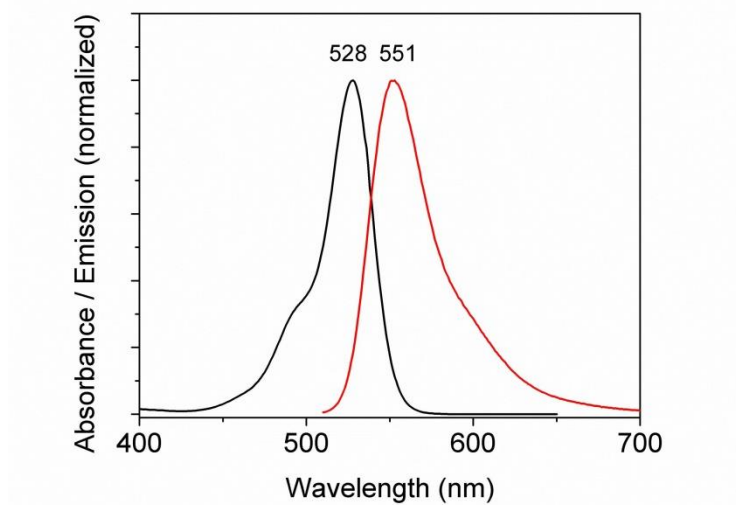


Figure 32. Linear absorption and emission spectra of R6G in methanol (λ_{ex} was 500 nm for the emission spectrum).

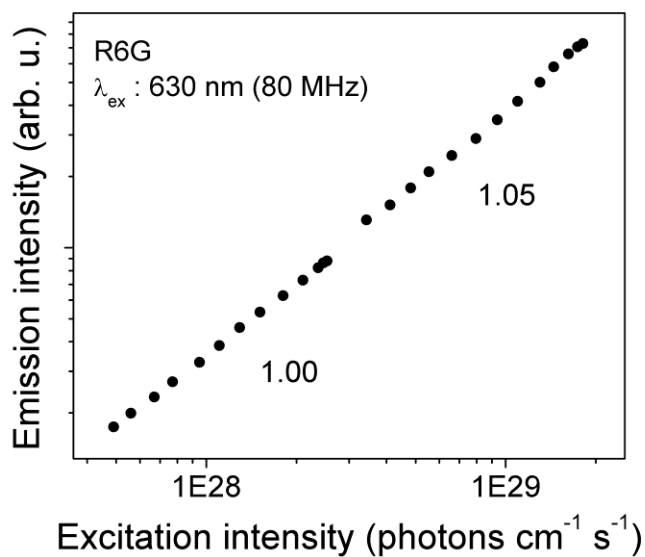


Figure 33. Logarithmic plot of the emission intensity of R6G as a function of excitation intensity with the 76 MHz setup at room temperature (λ_{ex} : 630 nm). The numbers on each data set indicate the local power scaling (the slope in the log-log plot).

5.2.5 Pulse train shaping technique

Pulse shaping (either of individual pulses¹⁵⁴, or of the pulse train itself¹⁵³) offers new ways to sensitively measure nonlinear properties, such as nonlinear absorption or nonlinear refraction. For example, nonlinear absorption cross sections were measured by analyzing the electronic spectrum of an amplitude-modulated pulse train transmitted through a sample.¹⁵³ In practice, the drawback of this method is that it requires very clean sinusoidal modulation, which is difficult to achieve with high modulation depth. Here we describe a more robust pulse train shaping method that allows for the selective recording of nonlinear fluorescence signals. The key concept of this method is illustrated in Figure 34. The first half of an optical excitation pulse sequence of period T consists of a stable pulse train with pulses of fixed pulse energy, while the second half is divided up into N on-off cycles of duration t (with $t \ll T$), switching between periods when the pulse energy is twice as large and when the light is off. The detected fluorescence signal is analyzed with a lock-in amplifier at the fundamental frequency $f = 1/T$. In the case of linear fluorescence, the averaged fluorescence energy in the first half and the second half of the sequence are identical, and no signal variation at the fundamental frequency f is recorded. For two-photon fluorescence the intensity-squared scaling leads to an average fluorescence in the second half that is twice as large as in the first half, leading to a detectable signal at the frequency f .

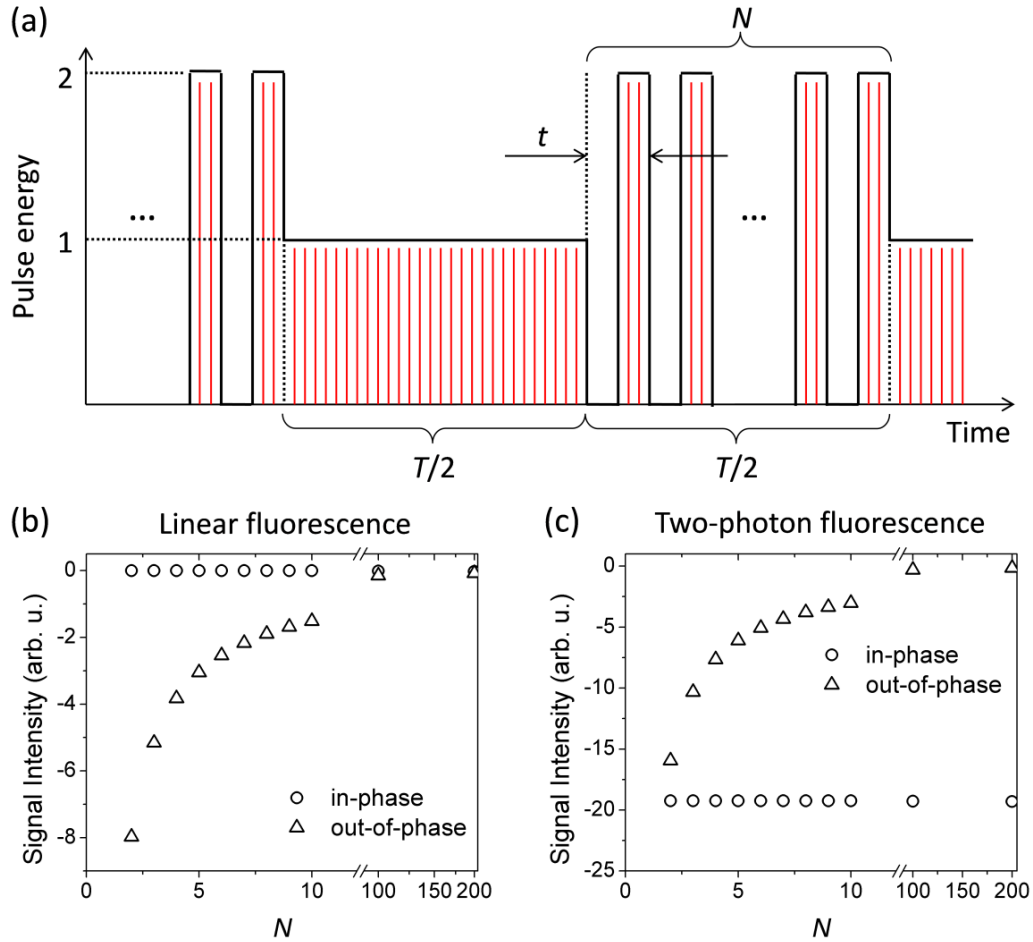


Figure 34. (a) Schematic of the pulse train shaping technique where T is the total period of the pulse train, t is the duration of one on-off cycle, and N is the number of on-off cycles. Red lines represent individual pulses of a high-repetition rate laser (not to scale). Calculated “in-phase” and “out-of-phase” components of a lock-in amplifier’s signal as a function of N at frequency $f=1/T$ for the case of linear fluorescence (b) and two-photon fluorescence (c).

In practice, since lock-in amplifiers separate the signal into in-phase (

$\int_0^T s(N, T) \sin(\omega t) dt$ where $s(N, T)$ is the fluorescence signal function and $\omega = 2 \pi/T$) and

out-of-phase ($\int_0^T s(N, T) \cos(\omega t) dt$) components, each component must be considered.

Figure 34(b) and Figure 34(c) show the calculated components of the signal that are in-

phase and out-of-phase with the pulse sequence as a function of the number of on-off cycles (N).

The in-phase component can be divided into a positive contribution

$\int_0^{T/2} s(N, T) \sin(\omega t) dt$ from the stable pulse train part and a negative contribution

$\int_{T/2}^T s(N, T) \sin(\omega t) dt$ from the N on-off cycle parts. For the linear fluorescence case the

positive contribution and the negative contribution are equal, canceling the signal for all

N . For two-photon fluorescence, however, the negative contribution is always larger

than the positive contribution, producing a non-zero signal which is independent of N

as the cancelation of the positive and negative contribution no longer remains. The out-

of-phase components for both linear and two-photon fluorescence are not zero due to

the asymmetric character of $\int_0^{T/2} s(N, T) \cos(\omega t) dt$ and $\int_{T/2}^T s(N, T) \cos(\omega t) dt$ at low N

but eventually zero out at high N . Thus, the detection of the in-phase component at large

N enables us to single out two-photon fluorescence from the significant linear

fluorescence contamination.

The robustness arises from relative ease of adjustment. If the amplitude in the

second half of the train is not exactly equal to the amplitude in the first half, there will be

a residual in-phase component, both in the linear fluorescence and more importantly in

the laser amplitude itself. So the laser output can be directly measured, and the

amplitude of this component nulled, to calibrate the system and eliminate one-photon

fluorescence contributions.

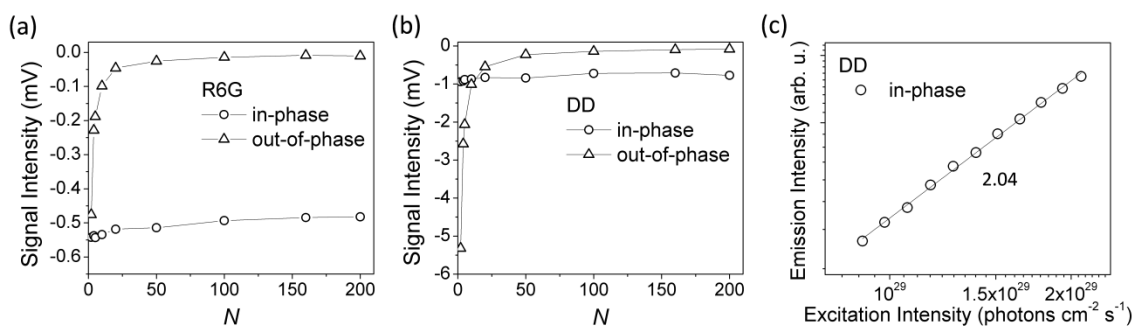


Figure 35. In-phase and out-of-phase components of pulse train shaping fluorescence signals in (a) R6G and (b) DD as a function of N (the number of on-off cycles). Measurements were performed with the 76 MHz system at $\lambda_{\text{ex}} = 800$ nm and $T = 2$ ms. (c) Logarithmic plot of the in-phase component of the emission intensity of DD as a function of excitation intensity at $N = 200$ and $T = 2$ ms; the power scaling is indicated in the graph.

Figure 35 shows the in-phase and out-of-phase components of the measured fluorescence intensity in experiments that utilized the pulse train shaping for 800 nm excitation of DD and R6G chromophores at $T = 2$ ms as a function of the number of on-off cycles in the waveform. Note that R6G only exhibits two-photon fluorescence, with the Figure 35(a) traces reproducing the computationally predicted behavior for the in-phase and out-of-phase components of the two-photon fluorescence signal at frequency $f=1/T$ [Figure 34(c)]. In contrast, the analogous experiment carried out for DD [Figure 35(b)] reveals a mixture of linear and nonlinear fluorescence under these conditions. To demonstrate the suppression of the linear fluorescence contribution, we performed a power study using the measured in-phase fluorescence signal intensity acquired for $N = 200$ at excitation intensities of about 10^{29} photons $\text{cm}^{-2} \text{s}^{-1}$ [the lowest intensity used in Figure 29 (right)]. Whereas the conventional measurement demonstrates that the one-

photon-absorptive contribution plays the dominant role in determining the magnitude of the measured fluorescence signal [i.e., the slope of the log-log plot of emission intensity vs. excitation intensity is close to one, Figure 29 (right)], a similar analysis of the in-phase fluorescence component obtained in the pulse train shaping experiments demonstrates suppression of the linear contribution, [evidenced by a slope of 2 in the log-log plot of emission intensity vs. excitation intensity, Figure 35(c)]. In addition, Figure 36 indicates that clear N -dependence of the in-phase component of DD while R6G only exhibits two-photon fluorescence.

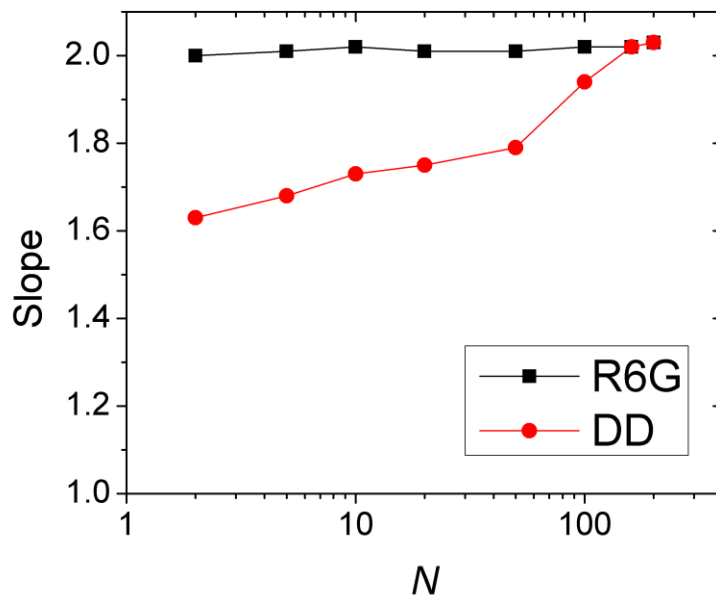


Figure 36. The detection of the in-phase component of R6G and DD as a function of N (the number of on-off cycles). Measurements were performed with the 76 MHz system at $\lambda_{\text{ex}} = 800 \text{ nm}$ and $T = 2 \text{ ms}$.

5.2.6 Estimation of two-photon absorption cross section of DD

Here we proceed to estimate the TPA cross section of DD from the two measurement methods: 1) from the pulse train shaping technique data, $\sigma_{2,DD}$ is determined by direct comparison with the TPA cross section of a reference standard (in this case R6G), and 2) from conventional measurements in which $\sigma_{2,DD}$ is determined by comparison with its linear cross section through its intensity-dependent power scaling.

Because our pulse train shaping method inherently suppresses linear contributions we directly obtain the two-photon cross section relative to the standard R6G (taking into account the differences in the detection efficiency) using

$$\sigma_{2,DD} = \frac{[C]_{R6G} \phi_{R6G} \eta_{R6G} \langle F \rangle_{DD}}{[C]_{DD} \phi_{DD} \eta_{DD} \langle F \rangle_{R6G}} \sigma_{2,R6G}$$

where $[C]$ is the concentration, ϕ the fluorescence quantum yield, η the collection efficiency of the system, and $\langle F \rangle$ the in-phase component of the detected fluorescence.

The relative collection efficiency is determined by the radiant sensitivity of the PMT and the transmittance through the fluorescence filter set over the spectral shape of the sample fluorescence. We performed measurements at 800 nm with an intensity of $I = 7.2 \times 10^{27}$ photons $\text{cm}^{-2} \text{s}^{-1}$ and a pulse sequence of $N = 200$ with a 2.76 μM sample of DD, and a 10 μM sample of R6G ($\pm 5\%$). The fluorescence signal ratio of R6G over DD was measured to be 1.06 with an error of $\sim 5\%$ for each of the measurements. The ratio of the detection efficiencies for our setup was determined to be 2.4 ± 0.3 (based on the PMT specifications and measured filter transmission). The quantum yields for R6G and DD were taken as 0.92 and 0.16, respectively, each with an estimated error of 10%. Using a

reference value of $\sigma_{R6G} = 65 \text{ GM}$,⁷ we obtain a TPA cross section for DD of $\sigma_{DD} = (2300 \pm 500) \text{ GM}$; however this value does not include the error of the reference value.⁷

From the conventional fluorescence measurements we estimate the two-photon absorption cross section of DD by comparison with its one-photon absorption cross section. Because this procedure determines the balance between linear and nonlinear contributions, only the 1 kHz experimental data is suitable (the high-repetition rate data does not show enough nonlinear contribution for reliable extraction). The linear absorptive cross section determination needs to take into account hot-band absorption and excitation geometry effects. In order to obtain an estimate of the linear cross section σ_{DD} without the need for a detailed calibration of absolute detection efficiencies we estimated σ_{DD} in turn by comparison with the known two-photon fluorescence properties of R6G using the same detection arrangement. By comparing the relative fluorescence at an excitation intensity below $10^{27} \text{ photons cm}^{-2} \text{ s}^{-1}$ (the linear region for DD and quadratic region for R6G) and correcting for relative differences in the detection efficiencies (the filter and PMT response) we estimate the effective linear cross section as $\sigma_{DD} = 1.2 \times 10^{-19} \text{ cm}^2$ for 800 nm excitation at room temperature. In order to compare linear and nonlinear contributions, we then write the measured time-averaged fluorescence as the sum of the one-photon contribution

$\langle F_1 \rangle = \varphi_1 \eta_1 [C]_{DD} \sigma_1 I_{\text{peak}} \langle f(t) \rangle \int S(\vec{r})$ (the angle brackets denote a temporal average and the integration extends over the sample volume) and two-photon contribution

$\langle F_2 \rangle = \frac{1}{2} \phi_2 \eta_2 [C]_{DD} \sigma_2 I_{\text{peak}}^2 \langle f(t)^2 \rangle \int S(\vec{r})^2$, where f and S are the temporal and spatial

parts of the light intensity $I(\vec{r}, t) = I_{\text{peak}} \cdot f(t) \cdot S(\vec{r})$, respectively.⁵ These contributions

are equal at $I_{\text{bal}} = 2 \frac{\sigma_1 \langle f(t) \rangle}{\sigma_2 \langle f(t)^2 \rangle} \cdot \frac{\int S(\vec{r})}{\int S(\vec{r})^2}$. For a Gaussian pulse in time the temporal ratio

in this expression is $\langle f(t) \rangle / \langle f(t)^2 \rangle = \sqrt{2}$. In our weak (or loose) focusing ($z_R \geq l$) case,

the spatial factor can be approximated as $\int S(\vec{r}) / \int S(\vec{r})^2 = 2$ for a collimated beam. We

extracted the peak intensity where one- and two-photon contributions balance from a

least-squares fit to the data in Figure 29 (left) as $I_{\text{bal}} = 6.4 \times 10^{28}$ photons $\text{cm}^{-2} \text{s}^{-1}$. Using

these values we obtain a TPA cross section estimated by conventional measurement

methods for DD at 800 nm of $\sigma = 1100$ GM. Because of the large uncertainties in the

determination of the hot-band linear cross section no error estimate is provided.

The conventional measurement followed by analytical model fitting that we used to determine σ of DD at 800 nm relies on the comparison with the linear cross section and hence requires tedious calibration of parameters affecting the relative fluorescence contributions (linear vs. nonlinear excitation volume, linear cross section at the appropriate excitation condition). In contrast, our pulse train shaping method suppresses linear contributions and allows for comparison with a known two-photon reference with only small corrections for the wavelength-dependent detection sensitivity. Currently the two methods produce TPA values that agree within a factor of two, but a careful absolute calibration of the detection system would improve precision

(especially for the conventional method by eliminating the need to compare with a nonlinear reference standard). We would also like to point out that the results of both measurements provide TPA cross-section values that are substantially larger than that determined earlier for high repetition rate excitation of DD over the 750-960 nm wavelength domain,⁸² where hot-band absorption and excitation geometry effects were underestimated.

5.2.7 Other effects potentially influencing multiphoton emission measurements

Since hot-band population depends on temperature, linear and nonlinear light absorption could affect steady-state emission measurements. However, using two- and three-dimensional heat dissipation models,¹⁵⁵ we estimate the steady-state temperature increase by linear absorption for 5 μM DD to be below 0.01°C for 76 MHz excitation at an average incident power of 50 mW (corresponding to a peak intensity of 1.0×10^{30} photons $\text{cm}^{-2} \text{s}^{-1}$), which does not significantly change the hot-band population. Under the same conditions the temperature increase at the focus, induced by two-photon absorption (with a two-photon absorption cross-section of 2300 GM at 800 nm) is estimated as ~ 1 °C.¹⁵⁶ This is much larger than for one-photon absorption but still generates only a $\sim 0.7\%$ change in hot band population.¹⁵⁵ Thus, we conclude that the dominant one-photon absorption we observed was not caused by absorption-induced local heating.

Triplet state accumulation by pulse pileup is a well-known effect that can lead to unexpected results in excited state measurements. In order to rule out any influence of

these effects on our power studies, we performed a series of tests. Firstly, nanosecond pump-probe transient absorption spectroscopic experiments determined the triplet state lifetime of DD in THF (aerated) with excitation at 550 nm (Figure S5). These spectra were acquired utilizing a flash photolysis spectrometer (Edinburgh Instruments, LP920). Pump pulses of ~5 ns duration were generated from a Q-switched Nd:YAG laser (Quantel, Brilliant) and a dual-crystal OPO (OPOTEK, Vibrant LDII). A Xe flash-lamp was used as a white light probe source. Samples were prepared in 1 cm quartz cells under aerated condition. Time constant at 480 nm (GSA: ground state bleaching) and 510 nm (ESA: excited state absorption) were measured as 247 ± 7 ns and 242 ± 11 ns, respectively. This triplet lifetime indicates that 1 kHz excitation does not provide fast enough pulse repetition to induce significant triplet state accumulation that could give rise to linear fluorescence contributions.

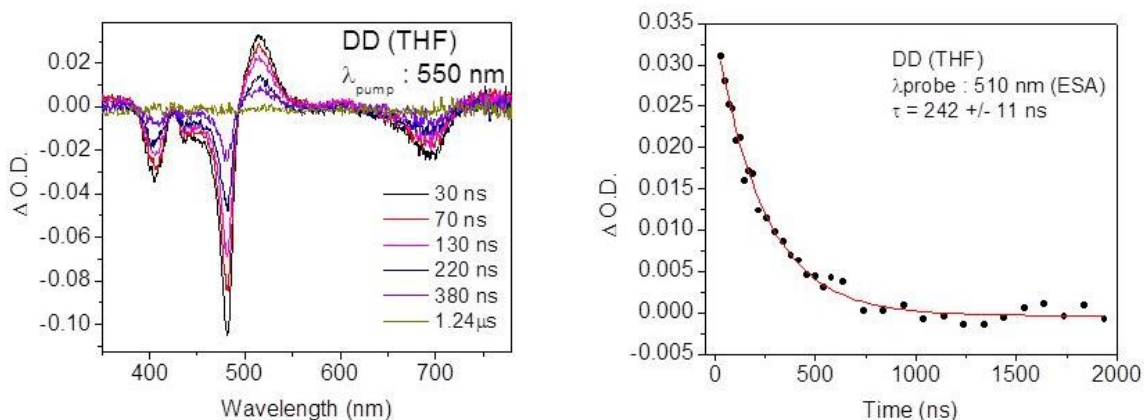


Figure 37. (a) Transient absorption spectra of DD in THF under aerated condition. Delay times are at 30, 70, 130, 220, 380 and 1240 ns ($\lambda_{ex} = 550$ nm). (b) Decay profiles of the excited state at 510 nm.

Secondly, we performed frequency-domain lifetime measurements for DD (Figure 38) with 76 MHz excitation using R6G as a reference. Phase-domain lifetime

measurements were performed with a widely tunable Ti:sapphire laser (Coherent, Chameleon, 80 MHz repetition rate) as an excitation source and the pulse train was intensity-modulated by an acousto optic modulator. With modulation frequencies from 0.7 MHz to 20 MHz, a lifetime of $\tau = 1.85$ ns was obtained (previously $\tau = 1.05$ ns was measured with time-domain methods).⁴⁷ Accordingly, we find that triplet states do not contribute to linear response at 800 nm excitation even at 76 MHz repetition rate.

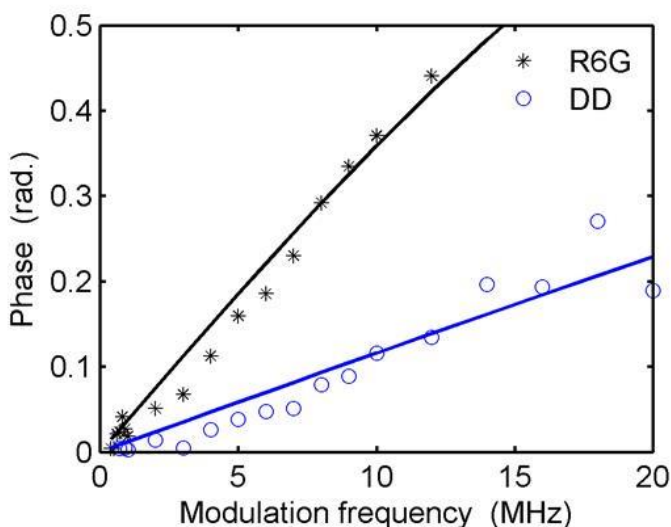


Figure 38. Frequency responses of R6G and DD under 80 MHz laser excitation. Experimental data and theoretical fitting line are represented by dots and solid lines, respectively ($\lambda_{\text{ex}} = 800$ nm). Lifetimes were fitted as 5.9 ns and 1.85 ns for R6G and DD, respectively.

5.3 Conclusion

With ever increasing attention to multiphoton imaging and broad biomedical applications using exogenous fluorophores, comprehensive insight into the nature of chromophoric linear and nonlinear responses requires significantly improved optical characterization methods. For the *meso-to-meso* ethyne-bridged bis[(porphinato)zinc(II)] fluorophore (DD), we have shown that for 800 nm excitation, this chromophore exhibits

concomitant linear hot-band absorption, and much more substantially under high-repetition rate excitation conditions. In conventional two-photon absorptive cross-section measurements, the relative contribution of linear and nonlinear fluorescence to the total measured signal is a function of the focusing geometry. Tight focusing, typically used in high-repetition rate systems, can result in a large linear fluorescence through hot-band absorption in out-of-focus regions, which can be problematic for TPA characterization especially in wavelength regions close to one-photon absorption bands (even in spectral regions with seemingly negligible linear absorption). Here we demonstrated key proof-of-principle experiments that show that appropriate pulse train shaping methods that suppress linear contributions to the fluorescence allow for extraction of pure nonlinear absorption cross sections, even in the presence of strong confounding linear fluorescence. Because our pulse train shaping method inherently suppresses any linear absorptive contribution to the fluorescence, this technique enables the use of high repetition rate laser excitation sources for determining TPA cross-sections under conditions identical to that used for TPF microscopy. Moreover, because this method should also be insensitive to linear fluorescence contributions in an imaging environment, it dramatically extends the excitable wavelength range of multi-photon contrast agents that can be used for tissue imaging applications.

5.4 Experimental

5.4.1 Materials

The reference compound, R6G, was purchased from Exciton, Inc. R6G samples were prepared at concentrations of 10 μM in methanol for all measurements. Synthesis and characterization for the compound DD in this study is described elsewhere.^{48, 52} Sample solutions of DD were prepared at concentrations of $< 10 \mu\text{M}$ in THF to avoid aggregation effects.

5.4.2 1 kHz power study

The emission intensity as a function of excitation power was acquired using a 1 kHz regenerative amplifier (Spectra Physics, Spitfire), producing 150 fs pulses (FWHM) at 800 nm. Excitation powers were varied over a range of ($10^{27} - 10^{30}$) photons $\text{cm}^{-2} \text{s}^{-1}$. Other wavelengths in the range of 500-1100 nm were obtained from an optical parametrical amplifier (OPA; Light Conversion, TOPAS-C) with pulse widths of typically 100-120 fs. For excitation, a 1 cm-path-length quartz cell was placed at the focal point of a weakly focused beam (with $f=+700$ mm lens producing 70 μm beam radius at the sample position). Emission was collected at 90° with a PMT (Hamamatsu, R3896) through a set of short-pass filters (Thorlabs, FES0700 and FES0750) to reject scattered excitation light. The PMT signal was amplified (Stanford Research Systems, SR445) and averaged with a gated integrator (Stanford Research Systems, SR250) for 10 s.

5.4.3 76 MHz power study

The emission intensity as a function of excitation power at 800 nm was acquired using a modelocked Ti:Sapphire laser (Spectra Physics, Tsunami, 76 MHz repetition rate) as the excitation source. Excitation powers were varied over a range of $(10^{28} - 10^{30})$ photons $\text{cm}^{-2} \text{s}^{-1}$. The beam was focused in the center of a 1 cm quartz cuvette using a 10x/NA 0.25 objective lens producing a beam radius of 1.0 μm at the focus. The detection optics were similar to the 1 kHz setup, but here a transimpedance amplifier (TTI PDA-700) and an oscilloscope measured the PMT signal. For other wavelengths, a widely tunable Ti:Sapphire laser (Coherent, Chameleon, 80 MHz repetition rate) was used as an excitation source. For confocal measurements, an iris was placed between the collection lens and the PMT.

5.4.4 Pulse shaping technique

A modelocked Ti:Sapphire laser (Spectra Physics, Tsunami, 76 MHz repetition rate) was used as the excitation source at 800 nm. To generate the desired intensity waveform the beam was focused into an acousto-optic modulator, whose drive signal was adjusted with an arbitrary function generator (LeCroy, LW420A). The beam was then focused in the center of a 1 cm quartz cuvette using a 10x/NA 0.25 objective lens. The detection was similar to the 76 MHz power study setup described above, with the oscilloscope replaced by a lock-in amplifier (Stanford Research Systems, SR830). The lock-in amplifier's reference signal was an on/off pulse sequence of period T derived from the second channel of the arbitrary function generator.

6. Two-photon Absorption of Various NIR-Emissive Porphyrin Arrays under NIR-II Wavelength Excitation

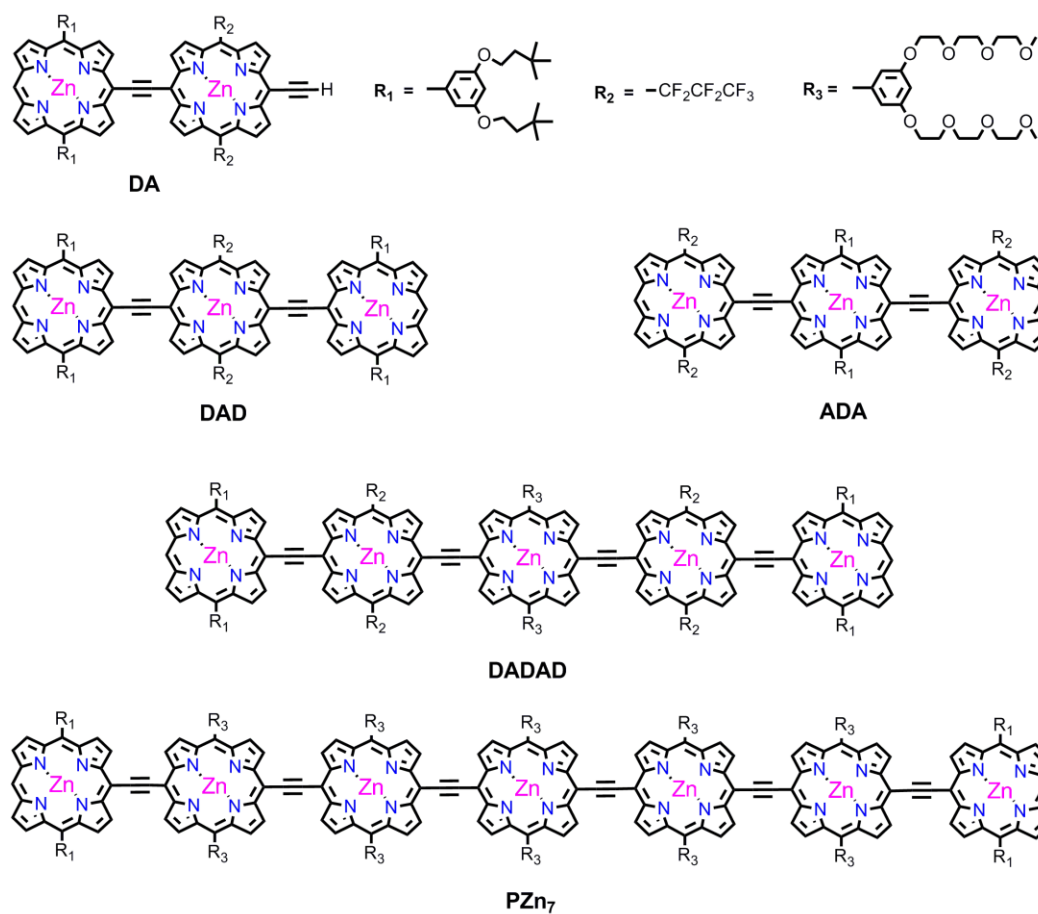
6.1 Introduction

Two-photon fluorescence microscopy (TPM) is often used in deep tissue imaging *in vivo* to provide subcellular structural and functional information.^{13, 16, 63} In particular, using long near infrared (NIR) wavelength (1000–1350 nm, NIR-II) excitation beyond the conventional tissue imaging window (700–1000 nm, NIR-I) and exogenous NIR-emissive markers have advantages that include negligible autofluorescence, improved imaging depth, and reduced photo-induced damage.²² In this context, there are two fundamental requirements for a NIR-emissive two-photon fluorophore for *in vivo* use: i) highly emissive in NIR region under NIR-II wavelength two-photon excitation, and ii) safe to use. Meeting these two conditions is not trivial. Firstly, fluorescence quantum yields in the NIR are restricted by the energy gap law, which dictates that the nonradiative decay rates are increased with smaller energy gaps due to enhanced overlap between vibronic wavefunctions of a ground state and an excited state.¹⁵⁷ This law accounts for the gradual decline of quantum yields of Alexa dyes from 0.92 to 0.12 from Alexa488 through Alexa750 (the numbers in their names refers to the approximate absorption maxima of each dye) in aqueous solution.¹⁵⁸ Secondly, most NIR fluorophores suffer from biocompatibility issues for *in vivo* applications. Although Alexa and cyanine dyes have shown two-photon absorption (TPA) cross-sections of $\sigma_2 = 1\text{--}70$ GM (Goeppert-Mayer, $1 \text{ GM} = 1 \times 10^{-50} \text{ cm}^4 \text{ s photon}^{-1}$) at 1000–1350 nm excitation wavelengths,²¹ the safety of these two dye series has not been proven. Other NIR fluorophores, such as

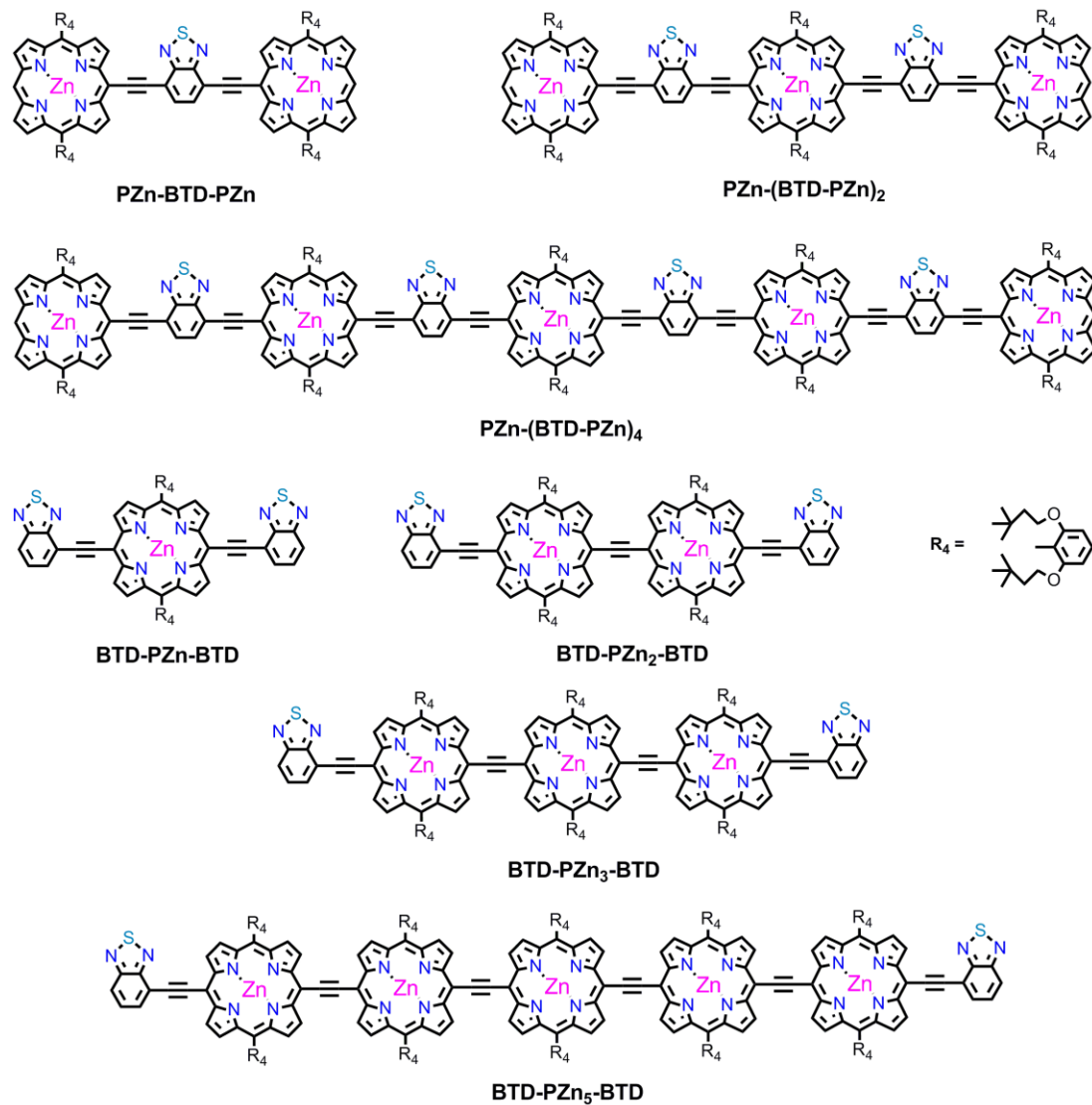
borondipyrromethane (BODIPY) and squaraine analogues, have been limited by the same problem.¹⁵⁹⁻¹⁶² Indocyanine green (ICG) is the only NIR-emissive fluorophore FDA-approved for human use; for this fluorophore, the emissive quantum yield in dimethyl sulfoxide (DMSO) is 0.11.¹⁶³ However, its low quantum yield in water, propensity for aggregation, and poor photostability are significant drawbacks to its used as a NIR dye for *in vivo* applications. Accordingly, although a great deal of effort has been made toward efficient and biocompatible NIR two-photon fluorophores, no satisfactory candidates for *in vivo* use are currently available.¹¹²

We recently discovered that highly conjugated *meso*-to-*meso* ethyne-bridged porphyrin arrays^{47-48, 50-52, 83-86, 164-166} manifest exceptionally large TPA cross-sections with high NIR-fluorescence quantum yields (Chapter 3). The *meso*-to-*meso* ethyne connectivity is of particular importance to achieve efficient two-photon fluorophores due to the generation of two-photon allowed states in the NIR-II wavelength window. More specifically, the generation of occupied and unoccupied orbitals of the same symmetries that results from *meso*-to-*meso* ethyne and butadiyne porphyrin connectivity is the fundamental origin of the two-photon allowed states. In addition, the inherent biocompatibility of porphyrins lends them promise as systems meeting the requirements for NIR-emissive two-photon fluorescent markers *in vivo*.^{35, 130} Although the poor solubility of porphyrin arrays in aqueous environments may appear to be an obstacle for their biological application, polymersomes can solve this problem by dispersing porphyrins in their hydrophobic bilayer in aqueous medium.^{57, 61, 110-112, 130, 133, 165-167}

Here we investigate the two-photon absorption of series of NIR-emissive porphyrin arrays inspired by the previous two-photon study on *meso*-to-*meso* ethyne-bridged bis-, tris-, and pentakis(porphinato)zinc(II) arrays (**PZn_n**; *n* = 2, 3, and 5) that were discussed in Chapter 3. The first class of compounds are donor-acceptor type *meso*-to-*meso* ethyne-bridged porphyrin arrays (**DA**, **DAD**, **ADA**, and **DADAD**; **DA**-derived porphyrin arrays)^{47-48, 84} which feature alternating electron-rich and electron-poor **PZn** and the *meso*-to-*meso* ethyne-bridged porphyrin heptamer (**PZn₇**) (Scheme 4). The second class of compounds are benzothiadiazole (BTD)-conjugated porphyrin oligomers (Scheme 5): these arrays consist of a BTD spacer between porphyrin units, **PZn-(BTD-PZn)_n**, and porphyrin arrays with BTD-groups conjugated at their terminal *meso*-positions, **BTD-PZn_n-BTD**. Notably, BTD-porphyrin oligomers exhibit large fluorescence quantum yields ($\phi = 13\text{--}36\%$ in toluene) in the NIR range (spanning a wavelength range of $\sim 700\text{--}1000$ nm). The interrogation of two-photon excited fluorescence reveals that these porphyrin oligomers possess large TPA cross-sections of up to ~ 40000 GM in the NIR-II excitation window with strong NIR-emission ($\phi = 0.09\text{--}0.36$). This work confirms that the design motif of connecting porphyrins *via* efficient π -conjugated bridge proposed in Chapter 3 is a promising strategy to prepare two-photon fluorophores that achieves strong NIR-emission under NIR-II excitation.



Scheme 4. Molecular structures of studied donor-acceptor type *meso-to-meso* ethyne-bridged porphyrin arrays and *meso-to-meso* ethyne-bridged porphyrin heptamer (PZn₇)



Scheme 5. Molecular structures of studied benzothiadiazole (BTD)-conjugated porphyrin arrays

6.2 Result and Discussions

6.2.1 Linear optical properties of highly conjugated porphyrins

6.2.1.1 Linear optical properties of meso-to-meso ethyne-bridged porphyrin arrays (DA-derived porphyrin arrays and PZn_n)

Porphyrin arrays featuring *meso-to-meso* ethyne linkage manifest broad Soret manifolds (S₂) due to exciton coupling and strongly allowed Q-state derived $\pi-\pi^*$ excited states (S₁).^{47-48, 50-52, 84, 168} Donor-acceptor type ethyne-bridged porphyrin arrays (i.e. DA-derived ethyne-bridged porphyrin arrays) inherit the broad Soret manifolds and strongly allowed Q-state derived $\pi-\pi^*$ excited states that progressively red-shift with increasing number of the oligomer units (Figure 39 and Table 6): S₂ band spanning ~360–550 nm and $\epsilon(S_1) = 34\,000\text{ M}^{-1}\text{cm}^{-1}$ (DA) – $176\,000\text{ M}^{-1}\text{cm}^{-1}$ (DADAD). While the red-shifts of the Q-derived $\pi-\pi^*$ states are observed in both PZn_n and DA-derived ethyne-bridged arrays, those of the DA-derived porphyrin arrays are less substantial than those of their PZn_n counterparts: e.g. $\lambda_{S_1, \max}(\text{PZn}_3) = 770\text{ nm} > \lambda_{S_1, \max}(\text{ADA}) = 760\text{ nm} > \lambda_{S_1, \max}(\text{DAD}) = 738\text{ nm}$ in THF (Table 6). This trend may indicate that the degree of conjugation strength is dependent upon frontier orbital wavefunction distribution among the porphyrin arrays of same molecular length. Congruent with PZn_n, DA-derived porphyrin arrays display strong NIR-emission ($\lambda_{\text{emi}, \max} = 786\text{--}840\text{ nm}$, $\phi = 0.17\text{--}0.19$) save for DA (Figure 40 and Table 6). The weak fluorescence of DA ($\phi = 0.063$) compared to relatively strong NIR fluorescence of PZn_n ($\phi = 0.14\text{--}0.22$) and other DA-derived porphyrin arrays ($\phi = 0.17\text{--}0.19$) has been ascribed to fast solvent relaxation processes that augment excited-state polarization and reduce concomitantly the S₁→S₀ oscillator strength.⁸⁴ Congruent with

the trend for PZn_n ($n = 2, 3, \text{ and } 5$), PZn_7 , the longest ethyne-bridged porphyrin array among available PZn_n displays NIR-absorption and emission peaked at 864 nm and 903 nm, respectively, with a modest fluorescence quantum yield of 0.089 (Figure 39, Figure 40, and Table 6).

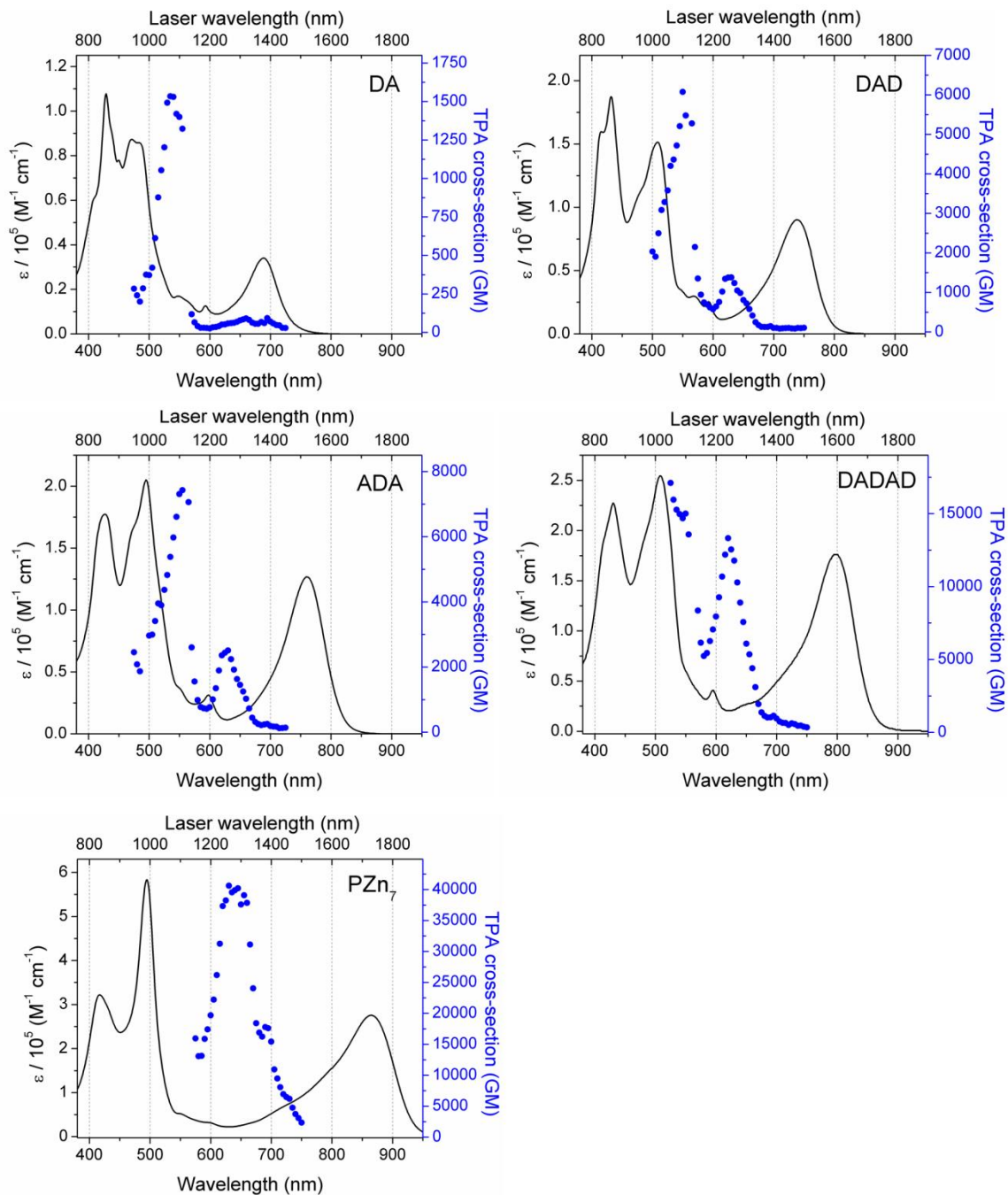


Figure 39. One- (solid line) and two-photon (blue dot) absorption spectra of donor-acceptor type *meso-to-meso* ethyne-bridged porphyrins arrays and *meso-to-meso* ethyne-bridged porphyrin heptamer in THF. While TPA spectra are plotted with doubled laser excitation wavelengths (bottom axis) for direct comparison with one-photon absorption spectra, original laser excitation wavelengths for TPA spectra are indicated at top axis.

Table 6. Summary of Spectroscopic Parameters of Studied Oligomeric Porphyrins

Compound	λ_{\max} (S ₀ →S ₁) /nm	ϵ^a (S ₁) /M ⁻¹ cm ⁻¹	λ_{\max} (S ₁ →S ₀) /nm	ϕ^b	σ_2 /GM	$\lambda_{\text{TPA,max}}$ (S ₀ →S _{TPA}) /nm	$\sigma_2\phi^c$ /GM
Ethyne-bridged porphyrins ^d							
DA	689	34 000 ^e	750	0.063 ^e	1500	1080	97
DAD	738	84 000 ^e	786	0.17 ^e	6100	1100	1000
ADA	760	127 000	810	0.17	7400	1110	1200
DADAD	798	176 000 ^e	840	0.19 ^e	13000	1240	2500
PZn ₂ ^f	690	51 400	711	0.16 ^e	1300	1030	210
PZn ₃ ^f	770	116 000	806	0.22 ^e	7000	1100	1400
PZn ₅ ^f	842	230 000	883	0.14 ^e	76000 15000	1040 1280	11000 2100
PZn ₇	864	276 000	903	0.089	40000	1280	3600
BTD-porphyrins ^g							
PZn-BTD- PZn	667	117 000	688 756	0.32 ^h (0.31) ⁱ	2500	1040	800
PZn-(BTD- PZn) ₂	718	103 000	736	0.36 ^h (0.36) ⁱ	5000	1080	1800
PZn-(BTD- PZn) ₄	745	105 000	763	0.26 ^h (0.29) ⁱ	7800	1100	2000
BTD-PZn- BTD	660	69 000	668 733	0.14 ^h (0.13) ⁱ	19.5	1210	2.7
BTD-PZn ₂ - BTD	736	99 000	697 762	0.29 ^h (0.30) ⁱ	3800	1080	1100
BTD-PZn ₃ - BTD	770	79 000	811	0.33 ^h (0.29) ⁱ	4000	1150	1300
BTD-PZn ₅ - BTD	799	81 000	840	0.33 ^h (0.28) ⁱ	6500	1210	2200

(^aMolar extinction coefficient. ^bFluorescence quantum yield. ^cTwo-photon action cross-section. ^dMeasured in THF. ^eData from T. Duncan et al. (2006)⁴⁷ /^fPreviously measured linear and nonlinear optical parameters of **PZn₂**, **PZn₃**, and **PZn₅** are also summarized in this table for comparison. ^gMeasured in Toluene. ^hMeasured by an integrating sphere upon S₁ band excitation. ⁱMeasured by Ian Stanton upon S₂ band excitation)

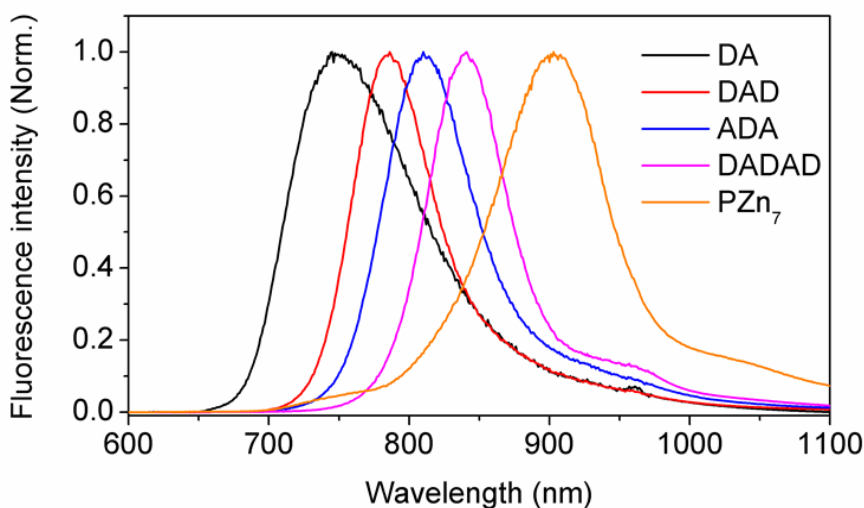


Figure 40. Normalized emission spectra of donor-acceptor type *meso-to-meso* ethyne-bridged porphyrin arrays and *meso-to-meso* ethyne-bridged porphyrin heptamer (PZn_7) measured by 480 nm excitation in THF.

6.2.1.2 Linear optical properties of BTD-conjugated porphyrin arrays

Over the last decades, the Therien lab has developed unique *meso*-ethynyl-bridged porphyrin oligomers (PZn_n) that directly link juxtaposed (porphinato)zinc(II) (PZn) moieties.^{48, 50-52, 84, 86, 164, 168} Such connectivity engenders strong π -conjugation through the entire chromophores and creates large dipole strength emissions that penetrate into the NIR range (over 800 nm). As an extended endeavor to manipulate the electronic energy gap and emission characteristics, various PZn -spacer- PZn supramolecules have been synthesized.¹⁶⁸ The spacers include 4,7-diethynylbenzo[c][1,2,5]thiadiazole (**E-BTD-E**), 6,13-diethynylpentacene (**E-PC-E**), 4,9-diethynyl-6,7-dimethyl[1,2,5]thiadiazolo[3,4-g]quinoxaline (**E-TDQ-E**), and 4,8-diethynylbenzo[1,2-c:4,5-c']bis([1,2,5]thiadiazole) (**E-BBTD-E**). Among these, the $PZnE$ -**BTD-EPZn** (or PZn -**BTD-PZn** in this dissertation for simplicity) compound exhibited a

high fluorescence quantum yield of 31% (in toluene). Based upon this observation, the Therien lab has recently developed new classes of benzothiadiazole (BTD)-conjugated porphyrin oligomers (Scheme 5). These classes consist of extended oligomers that feature a BTD spacer between each porphyrin unit, such as **(PZn-(BTD-PZn))_n**, and porphyrin arrays with BTD groups conjugated at two terminal *meso*-positions, **(BTD-(PZn)_n-BTD)**.

The linear absorption spectra of these porphyrin series are shown in Figure 41 and summarized in Table 6. While the B_x-state (x axis congruent with the long molecular axis) is dominant in magnitude for **BTD-PZn_n-BTD**, in resemblance to the absorption spectra of **PZn_n**, the B_y-state is dominant for **PZn-(BTD-PZn)_n** indicating a lower degree of conjugation via BTD-linkage between **PZn** units than ethyne-linkage. Nonetheless, all of these BTD-conjugated porphyrin oligomers manifest broad Soret-bands whose spectral domains span a wide ~380–550 nm wavelength window. Another feature of the absorption spectra of BTD-porphyrin oligomers are strong Q-derived π - π^* absorptions that red-shift with increasing molecular length, in common with highly conjugated porphyrin arrays. While the absorption peak of **PZn-BTD-PZn** appears at 667 nm, that of **BTD-PZn₂-BTD** lies at 736 nm, lower in energy than that of **PZn₂** ($\lambda_{\text{max}} = 694$ nm) indicating effective π -conjugation in **BTD-PZn₂-BTD**. Apparently, the more porphyrin units connected through linkers, the longer maximum absorption wavelength up to 799 nm (**BTD-PZn₅-BTD**). Interestingly, the degree of the red-shift in **BTD-PZn_n-BTD** as a function of **PZn** repeat units is saturated more readily than for **PZn_n**: the

difference between absorption peak maxima of **BTD-PZn₂-BTD** ($\lambda_{\text{max}} = 736$ nm) and **BTD-PZn₅-BTD** ($\lambda_{\text{max}} = 799$ nm) [1071 cm⁻¹] is much smaller than that of **PZn₂** ($\lambda_{\text{max}} = 694$ nm) and **PZn₅** ($\lambda_{\text{max}} = 842$ nm) [2532 cm⁻¹]. While several factors may contribute to this, including solvation (**BTD-PZn_n-BTD** in toluene and **PZn_n** in THF) and slightly broader full width at half-maximums of **BTD-PZn_n-BTD** than **PZn_n**, the origin of this early saturation of the red-shifted absorption in **BTD-PZn_n-BTD** compared to **PZn_n** is not definitely known.

Notably, these supermolecules have exhibited large fluorescence quantum yields of 13–36% in the NIR range (spanning 700–1000 nm), measured in toluene under both S₂ and S₁ band excitation (Table 6). The emissive quantum yields of **PZn-(BTD-PZn)_n** and **BTD-(PZn)_n-BTD** were measured using an integrating sphere and are summarized in Table 1. That the fluorescence quantum yields are similarly large whether exciting in the Soret region (483 nm) or S₁ region (Table 6) indicates that there are no additional photo-induced processes during the internal conversion S₂→S₁. Congruent with the trend in absorption spectra, emission peak maxima red-shift with increasing oligomeric lengths, spanning a wavelength range of 668–840 nm (**BTD-PZn_n-BTD**) and 688–756 nm [**PZn-(BTD-PZn)_n**].

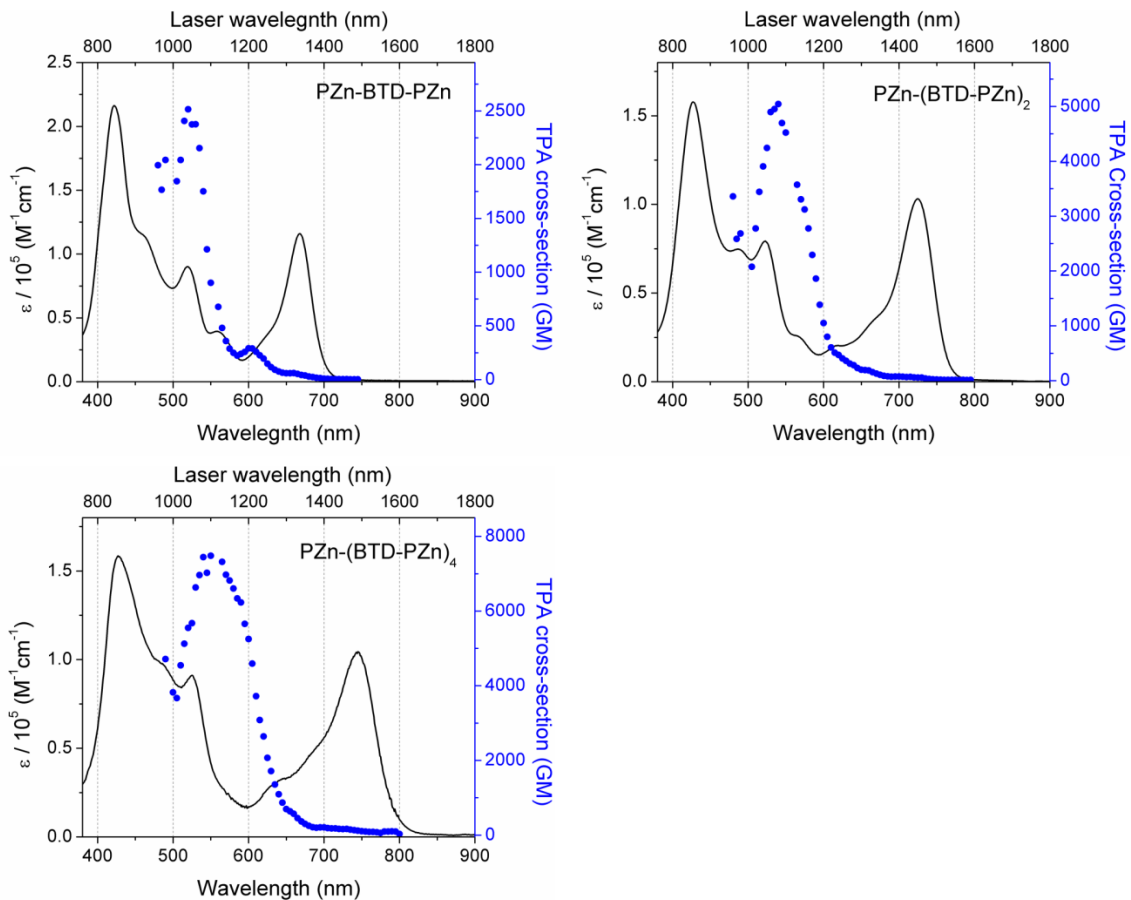


Figure 41. One- (solid line) and two-photon (blue dot) absorption spectra of $\text{PZn}-(\text{BTD-PZn})_n$ in toluene. While TPA spectra are plotted with doubled laser excitation wavelengths (bottom axis) for direct comparison with one-photon absorption spectra, original laser excitation wavelengths for TPA spectra are indicated at top axis.

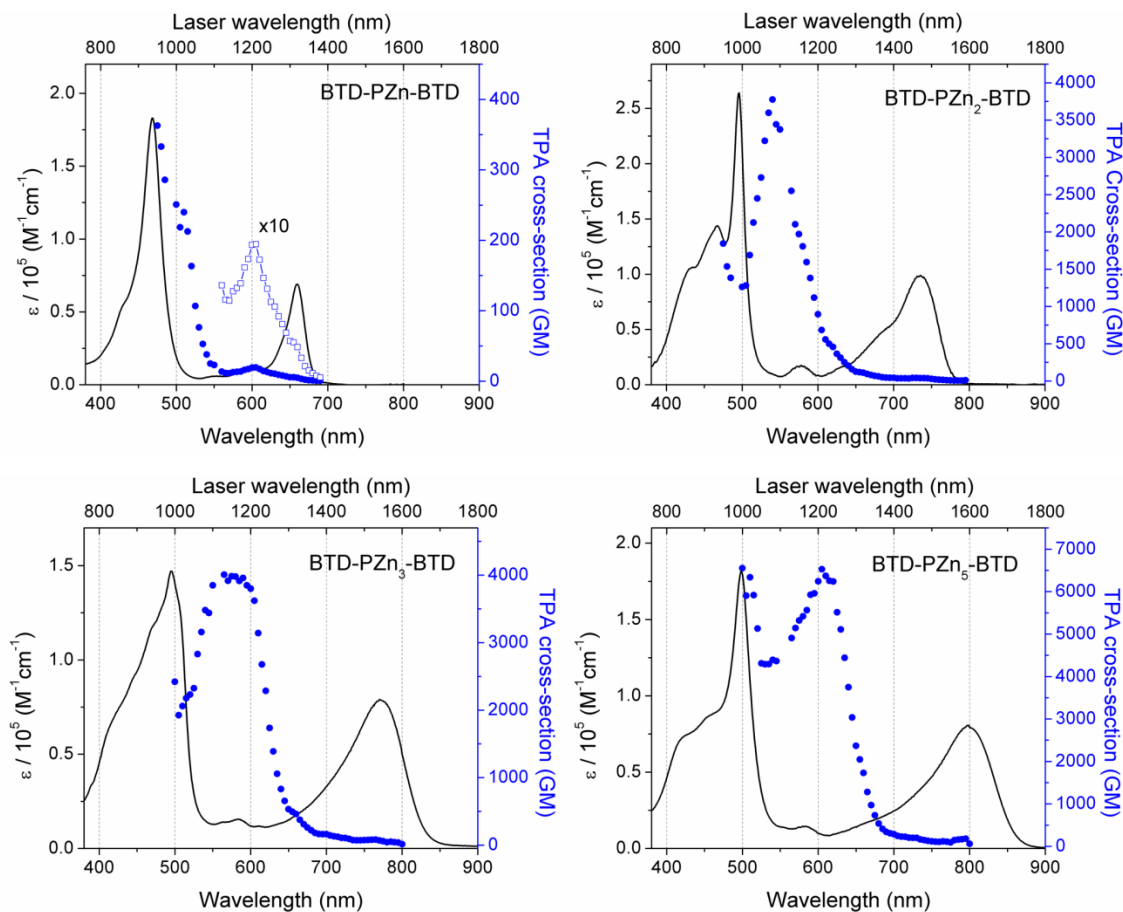


Figure 42. One- (solid line) and two-photon (blue dot) absorption spectra of BTD-PZn_n-BTD in THF [including magnified two-photon absorption spectra of BTD-PZn-BTD for clarity]. While TPA spectra are plotted with doubled laser excitation wavelength (bottom axis) for direct comparison with one-photon absorption spectra, original laser excitation wavelength for TPA spectra are indicated at top axis.

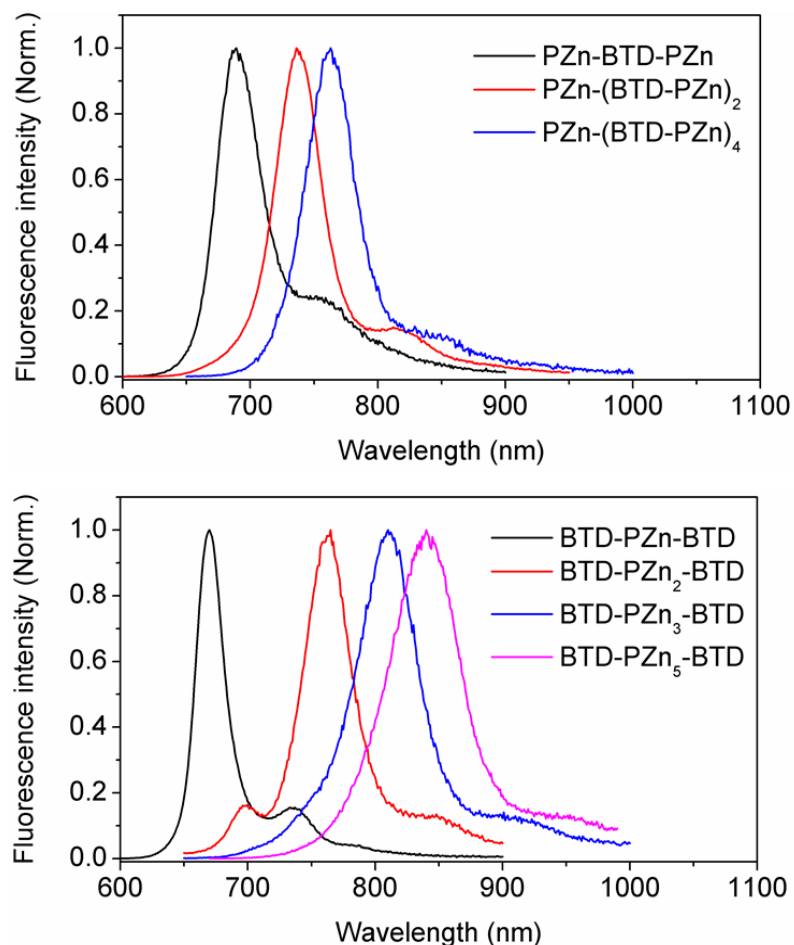


Figure 43. Emission spectra of $\text{PZn}-(\text{BTD-PZn})_n$ and $\text{BTD-PZn}_n\text{-BTD}$ measured in toluene.

6.2.2 Two-photon absorption of highly conjugated porphyrin arrays

6.2.2.1 Two-photon absorption of meso-to-meso ethyne-bridged porphyrin arrays (DA-derived porphyrin arrays and PZn)

Our previous study (described in Chapter 3) on *meso-to-meso* ethyne-bridged porphyrins (PZn_{2-5}) showed that ethyne connectivity via *meso*-positions between PZn units render the multimeric porphyrins strong two-photon absorbers. Not only the impressive magnitude of σ_2 (up to 76000 GM, PZn_5) but also the wavelength region of

the corresponding TPA transitions ($\lambda_{\text{TPA}} = \sim 1030\text{--}1100\text{ nm}$ and $\sim 1280\text{ nm}$) make them promising two-photon imaging markers for *in vivo* under excitation in the NIR-II tissue imaging window (1000–1350 nm). Density function theory calculations confirmed the existence of two-photon allowed states lying in the energy region where two-photon states were experimentally observed. The calculated frontier orbitals and excited states revealed the origin of TPA transitions with large cross-sections of **PZn₂₋₅** [$\sigma_2(\text{PZn}_2) = 1300\text{ GM}$ at 1040 nm, $\sigma_2(\text{PZn}_3) = 7000\text{ GM}$, and $\sigma_2(\text{PZn}_5) = 76000\text{ GM}$] in NIR-II: while pristine monomeric porphyrins give rise to only one-photon allowed states from transitions between occupied and unoccupied orbitals with antisymmetric relation (i.e. *ungerade* \rightarrow *gerade* frontier orbitals), *meso-to-meso* ethyne bridged porphyrins (**PZn₂₋₅**) possess occupied and unoccupied orbitals with symmetries that give rise to multiple transitions (i.e. *ungerade* \rightarrow *ungerade* or *gerade* \rightarrow *gerade*) which are accessible by two-photon absorption. The previous work predicts the possibility of large TPA cross-sections from other types of ethyne-bridged porphyrin arrays with *meso-to-meso* connectivity, for example donor-acceptor type ethyne bridged porphyrin arrays.

Table 6 summarizes the result of two-photon excited fluorescence measurements of **DA**-derived ethyne-bridged porphyrin arrays (**DA**, **DAD**, **ADA**, and **DADAD**). Congruent with the previous prediction in Chapter 3, the **DA**-derived porphyrins display large two-photon absorption cross-sections that are comparable in magnitude and energy to those for **PZn_n** of the same molecular length (Figure 39 and Table 6); $\sigma_2(\text{DA}) = 1500\text{ GM}$ at 1080 nm, $\sigma_2(\text{DAD}) = 6100\text{ GM}$ at 1100 nm, $\sigma_2(\text{ADA}) = 7400\text{ GM}$ at

1110 nm, and $\sigma_2(\text{DADAD}) = 13000 \text{ GM}$ at 1240 nm. Similar two-photon absorption cross-sections were measured from **DAD** (6100 GM at 1100 nm) and **ADA** (7400 GM at 1110 nm), almost identical to that of **PZn₃** (7000 GM at 1100 nm), considering a typical error range (10–30%) of TPEF measurement.^{5,7} Interestingly, **DA**-derived ethyne-bridged porphyrin oligomers' two-photon transition wavelengths [$\lambda_{\text{TPA}}(\text{DA}) = 1080 \text{ nm}$, $\lambda_{\text{TPA}}(\text{DAD}) = 1100 \text{ nm}$, and $\lambda_{\text{TPA}}(\text{ADA}) = 1110 \text{ nm}$] coincide with those of **PZn₂₋₃** [$\lambda_{\text{TPA}}(\text{PZn}_2) = 1030 \text{ nm}$ and $\lambda_{\text{TPA}}(\text{PZn}_3) = 1100 \text{ nm}$], indicating the similar origin of two-photon transitions. While **PZn₅** showed two distinctive two-photon transitions at 1040 nm and 1280 nm, **DADAD** displayed a single TPA peak at 1240 nm in the studied wavelength range of 1050–1500 nm, illustrating the difference in energy between the two-photon allowed excited states of **DADAD** and **PZn₅**.

It is noteworthy that strong enhancements of TPA cross-section have been reported by introducing centrosymmetric quadrapolar structure (donor-acceptor-donor or acceptor-donor-acceptor).^{108, 123, 169-170} However, these **DA**-derived porphyrin oligomers featuring centrosymmetric quadrapole architectures (**DAD**, **ADA**, and **DADAD**) possess σ_2 values that are almost identical to those of the corresponding **PZn_n** of the same molecular length. The design principle of constructing centrosymmetric quadrapolar chromophores derived from simple organic units (mainly composed of benzene and vinyl groups) has little impact upon highly conjugated porphyrin arrays, consistent with a previous study on butadiyne-bridged porphyrin dimers of

quadrupolar character.^{108, 123} Alternatively, it may be simply due to the weak strength of charge redistribution in **DAD**, **ADA**, and **DADAD**.

6.2.2.2 Two-photon absorption of **BTD**-conjugated porphyrin arrays

Two-photon spectroscopic data for **BTD**-conjugated porphyrin arrays are summarized in Table 6. For **PZn-(BTD-PZn)_n**, the two photon cross-sections increase stepwise with increasing **PZn** unit; $\sigma_2 = 2500, 5000, \text{ and } 7800 \text{ GM}$ [**PZn-BTD-PZn**, **PZn-(BTD-PZn)₂**, and **PZn-(BTD-PZn)₄**, respectively]. The maximum two photon absorption peaks shift from 1040 through 1100 nm from the dimer to the pentamer (Figure 41 and Figure 44). Due to the high fluorescence quantum yields of these porphyrin systems, two-photon action cross-sections of 800, 1800 and 2000 GM were measured for **PZn-BTD-PZn**, **PZn-(BTD-PZn)₂**, and **PZn-(BTD-PZn)₄**, respectively.

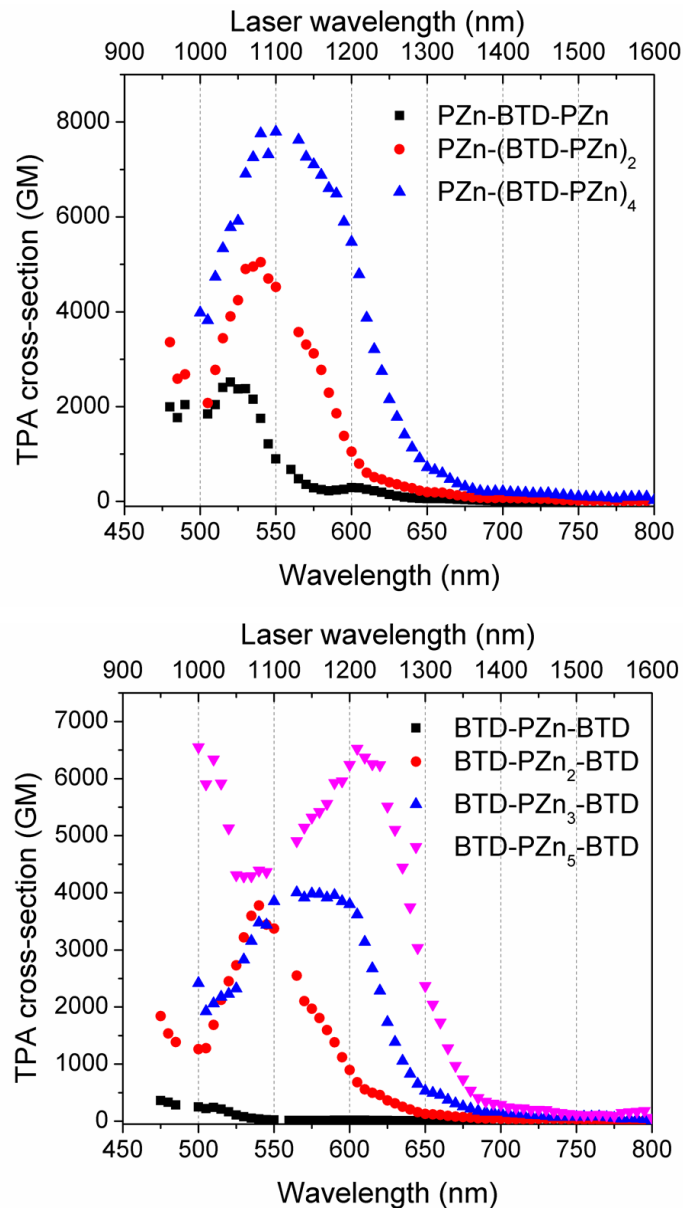


Figure 44. Two-photon absorption spectra of $\text{PZn}-(\text{BTD-PZn})_n$ and $\text{BTD-PZn}_n\text{-BTD}$ measured in Toluene. While TPA spectra are plotted with doubled laser excitation wavelength (bottom axis), original laser excitation wavelength for TPA spectra are indicated at top axis.

Large NIR-II window TPA cross-sections were also found for $\text{BTD-PZn}_n\text{-BTD}$, save the monomeric BTD-conjugated porphyrin (BTD-PZn-BTD). BTD-PZn-BTD showed a small TPA cross-section of 17 GM at 1210 nm, which is similar in magnitude to

photon absorptions of highly conjugated porphyrin arrays that include donor-acceptor type *meso*-to-*meso* ethyne-bridged porphyrin arrays, *meso*-to-*meso* ethyne bridged porphyrin heptamer, and benzothiadiazole-conjugated porphyrin arrays. These multiporphyrins exhibited large TPA cross-sections (1500–40000 GM) in NIR-II wavelengths and NIR-emissions tunable over a 688–950 nm spectral window. While donor-acceptor type *meso*-to-*meso* ethyne-bridged porphyrin arrays inherit the two-photon absorption characteristics of **PZn_n**, which are optimal for ~1100 nm and ~1300 nm excitation, benzothiadiazole-conjugated porphyrin arrays manifest two-photon transitions that progressively red-shift with increasing conjugation length in the range of 1040–1210 nm. The large TPA cross-sections of these various NIR-emissive conjugated porphyrin arrays, coupled with selectable excitation wavelength in the NIR-II region, underscore the potential of these porphyrin arrays as two-photon fluorescent markers.

6.4 Experimental

6.4.1 Materials

The synthesis and characterization of porphyrins studied here was accomplished by Drs. Kimihiro Susumu, Jeff Rawson, and Wei Qi, former Therien group members. Details of synthesis of characterization of donor-acceptor type porphyrins can be found in the work published by Dr. Kimihiro Susumu, save ADA.⁴⁸ ADA was synthesized by Dr. Jeff Rawson (personal communication). BTD-porphyrins were prepared and characterized by Dr. Wei Qi (Ph. D. dissertation; University of Pennsylvania, 2011).

Sample solutions of studied porphyrin arrays were prepared at concentrations of $< 10 \mu\text{M}$ in THF or toluene to avoid aggregation.

6.4.2 Linear absorption and emission spectra measurement

Electronic spectra were recorded on an absorption spectrometer (Shimadzu, PharmaSpec UV1700) and an emission spectrophotometer (Edinburgh, FLSP920) in 10 mm quartz optical cells. The fluorescence quantum yields (ϕ) of solution samples were measured with an absolute photoluminescence quantum yield measurement system (Hamamatsu, C9920-02) which is composed of Xe-lamp, a monochromator, and a multichannel charge-coupled device (CCD) spectrometer (Hamamatsu Photonics, PMA-12) at room temperature. Optical densities of samples in 10 mm path length quartz cuvette were kept below 0.1 and quantum yield were calculated as an average from four different measurements.

6.4.3 Two-photon absorption cross-section measurement

Two-photon absorption cross-section spectra were measured using a standard TPEF (two-photon excited fluorescence) method.⁵ Excitation laser pulses were generated using a tunable optical parametrical amplifier (OPA; Light Conversion, TOPAS-C) with pulse widths of typically 100-120 fs. For excitation, a 1 cm-path-length quartz cell was placed in a weakly focused beam (12 mrad divergence angle) using a lens with 300 mm focal length. Loosely focused beam was used to avoid linear contribution from off-focus region.⁸⁰ Typical excitation power was kept below $\sim 5 \text{ mW}$. Emission was collected at 90° with an amplified photodiode (Thorlabs, PDA36A) through an appropriate set of short-

pass filters to reject scattered excitation light. A lock-in amplifier (Stanford Research Systems, SR830) was used to selectively measure the emission. Styryl 9M (Sigma-Aldrich) in chloroform was used as a standard in the wavelength range of 900–1500 nm.⁷ The emission intensity of porphyrin arrays as a function of excitation power was acquired to confirm quadratic dependence. We obtained the two-photon absorption cross section of chromophores relative to the standard Styryl 9M (taking into account the differences in the detection efficiency) using

$$\sigma_{2, sample} = \frac{[C]_{S9M} \eta_{S9M} \phi_{S9M} n_{S9M} \langle F \rangle_{sample}}{[C]_{sample} \eta_{sample} \phi_{sample} n_{sample} \langle F \rangle_{S9M}} \sigma_{2, S9M}$$

where [C] is the concentration, η the collection efficiency of the system, ϕ the fluorescence quantum yield, n the refractive index and $\langle F \rangle$ the intensity of the detected fluorescence.

References

1. Göppert-Mayer, M., Über Elementarakte mit zwei Quantensprüngen. *Annalen der Physik* **1931**, 401 (3), 273-294.
2. Kaiser, W.; Garrett, C. G. B., Two-Photon Excitation in CaF₂:Eu²⁺. *Phys. Rev. Lett.* **1961**, 7 (6), 229-231.
3. Mertz, J., Nonlinear microscopy: new techniques and applications. *Curr. Opin. Neurobiol.* **2004**, 14 (5), 610-616.
4. Denk, W.; Strickler, J.; Webb, W., Two-photon laser scanning fluorescence microscopy. *Science* **1990**, 248 (4951), 73-76.
5. Xu, C.; Webb, W. W., Measurement of two-photon excitation cross sections of molecular fluorophores with data from 690 to 1050 nm. *J. Opt. Soc. Am. B* **1996**, 13 (3), 481-491.
6. Albota, M. A.; Xu, C.; Webb, W. W., Two-photon fluorescence excitation cross sections of biomolecular probes from 690 to 960 nm. *Appl. Opt.* **1998**, 37 (31), 7352-7356.
7. Makarov, N. S.; Drobizhev, M.; Rebane, A., Two-photon absorption standards in the 550-1600 nm excitation wavelength range. *Opt. Express* **2008**, 16 (6), 4029-4047.
8. Kierdaszuk, B.; Malak, H.; Gryczynski, I.; Callis, P.; Lakowicz, J. R., Fluorescence of reduced nicotinamides using one- and two-photon excitation. *Biophys. Chem.* **1996**, 62 (1-3), 1-13.
9. Mütze, J.; Iyer, V.; Macklin, John J.; Colonell, J.; Karsh, B.; Petrášek, Z.; Schwill, P.; Looger, Loren L.; Lavis, Luke D.; Harris, Timothy D., Excitation Spectra and Brightness Optimization of Two-Photon Excited Probes. *Biophys. J.* **102** (4), 934-944.
10. Svoboda, K.; Yasuda, R., Principles of Two-Photon Excitation Microscopy and Its Applications to Neuroscience. *Neuron* **2006**, 50 (6), 823-839.
11. Freund, I.; Deutsch, M., Second-harmonic microscopy of biological tissue. *Opt. Lett.* **1986**, 11 (2), 94-96.
12. So, P. T. C. S.; Dong, C. Y.; Masters, B. R.; Berland, K. M., Two-photon excitation fluorescence microscopy. *Annu. Rev. Biomed. Eng.* **2000**, 2, 399-429.
13. Zipfel, W. R.; Williams, R. M.; Webb, W. W., Nonlinear magic: multiphoton microscopy in the biosciences. *Nat. Biotechnol.* **2003**, 21 (11), 1369-1377.

14. Lichtman, J. W.; Conchello, J.-A., Fluorescence microscopy. *Nat. Methods* **2005**, *2* (12), 910-919.
15. Goldberg, J. H.; Tamas, G.; Aronov, D.; Yuste, R., Calcium Microdomains in Aspin Dendrites. *Neuron* **2003**, *40* (4), 807-821.
16. Cahalan, M. D.; Parker, I.; Wei, S. H.; Miller, M. J., Two-photon tissue imaging: seeing the immune system in a fresh light. *Nat. Rev. Immunol.* **2002**, *2* (11), 872-880.
17. Wilson, J. W.; Degan, S.; Gainey, C. S.; Mitropoulos, T.; Simpson, M. J.; Zhang, J. Y.; Warren, W. S., Comparing in vivo pump-probe and multiphoton fluorescence microscopy of melanoma and pigmented lesions. *J. Biomed. Opt.* **2014**, *20* (5), 051012-051012.
18. Madden, K. S.; Zettel, M. L.; Majewska, A. K.; Brown, E. B., Brain Tumor Imaging: Live Imaging of Glioma by Two-Photon Microscopy. *Cold Spring Harbor Protocols* **2013**, *2013* (3), pdb.prot073668.
19. Subha, R.; Nalla, V.; Yu, J. H.; Jun, S. W.; Shin, K.; Hyeon, T.; Vijayan, C.; Ji, W., Efficient Photoluminescence of Mn²⁺-Doped ZnS Quantum Dots Excited by Two-Photon Absorption in Near-Infrared Window II. *J. Phys. Chem. C* **2013**, *117* (40), 20905-20911.
20. Hong, G. S.; Diao, S.; Chang, J. L.; Antaris, A. L.; Chen, C. X.; Zhang, B.; Zhao, S.; Atochin, D. N.; Huang, P. L.; Andreasson, K. I.; Kuo, C. J.; Dai, H. J., Through-skull fluorescence imaging of the brain in a new near-infrared window. *Nature Photon.* **2014**, *8* (9), 723-730.
21. Kobat, D.; Durst, M. E.; Nishimura, N.; Wong, A. W.; Schaffer, C. B.; Xu, C., Deep tissue multiphoton microscopy using longer wavelength excitation. *Opt. Express* **2009**, *17* (16), 13354-13364.
22. Smith, A. M.; Mancini, M. C.; Nie, S., Bioimaging: Second window for in vivo imaging. *Nat. Nanotechnol.* **2009**, *4* (11), 710-711.
23. Matthews, T. E., Pump-Probe Molecular Imaging. *Ph.D. Thesis* **2011**.
24. Kobat, D.; Horton, N. G.; Xu, C., In vivo two-photon microscopy to 1.6-mm depth in mouse cortex. *J. Biomed. Opt.* **2011**, *16* (10), 106014-106014-4.
25. Theer, P.; Hasan, M. T.; Denk, W., Two-photon imaging to a depth of 1000 μm in living brains by use of a Ti:Al₂O₃ regenerative amplifier. *Opt. Lett.* **2003**, *28* (12), 1022-1024.

26. Balu, M.; Baldacchini, T.; Carter, J.; Krasieva, T. B.; Zadoyan, R.; Tromberg, B. J., Effect of excitation wavelength on penetration depth in nonlinear optical microscopy of turbid media. *J. Biomed. Opt.* **2009**, *14* (1), 010508-010508-3.
27. Andresen, V.; Alexander, S.; Heupel, W.-M.; Hirschberg, M.; Hoffman, R. M.; Friedl, P., Infrared multiphoton microscopy: subcellular-resolved deep tissue imaging. *Curr. Opin. Biotechnol.* **2009**, *20* (1), 54-62.
28. Herz, J.; Siffrin, V.; Hauser, A. E.; Brandt, A. U.; Leuenberger, T.; Radbruch, H.; Zipp, F.; Niesner, R. A., Expanding Two-Photon Intravital Microscopy to the Infrared by Means of Optical Parametric Oscillator. *Biophys. J.* **2010**, *98* (4), 715-723.
29. Zipfel, W. R.; Williams, R. M.; Christie, R.; Nikitin, A. Y.; Hyman, B. T.; Webb, W. W., Live tissue intrinsic emission microscopy using multiphoton-excited native fluorescence and second harmonic generation. *Proceedings of the National Academy of Sciences* **2003**, *100* (12), 7075-7080.
30. Larson, D. R.; Zipfel, W. R.; Williams, R. M.; Clark, S. W.; Bruchez, M. P.; Wise, F. W.; Webb, W. W., Water-Soluble Quantum Dots for Multiphoton Fluorescence Imaging in Vivo. *Science* **2003**, *300* (5624), 1434-1436.
31. Battersby, A. R., Tetrapyrroles: the pigments of life. *Nat. Prod. Rep.* **2000**, *17* (6), 507-526.
32. Li, L.-L.; Diao, E. W.-G., Porphyrin-sensitized solar cells. *Chem. Soc. Rev.* **2013**, *42* (1), 291-304.
33. Tanaka, T.; Osuka, A., Conjugated porphyrin arrays: synthesis, properties and applications for functional materials. *Chem. Soc. Rev.* **2015**, *44* (4), 943-969.
34. Auwärter, W.; Eciya, D.; Klappenberger, F.; Barth, J. V., Porphyrins at interfaces. *Nat. Chem.* **2015**, *7* (2), 105-120.
35. Huang, H.; Song, W.; Rieffel, J.; Lovell, J. F., Emerging Applications of Porphyrins in Photomedicine. *Front. Phys* **2015**, *3*.
36. Ishida, M.; Park, S. W.; Hwang, D.; Koo, Y. B.; Sessler, J. L.; Kim, D. Y.; Kim, D., Donor-Substituted β -Functionalized Porphyrin Dyes on Hierarchically Structured Mesoporous TiO₂ Spheres. Highly Efficient Dye-Sensitized Solar Cells. *J. Phys. Chem. C* **2011**, *115* (39), 19343-19354.
37. Yella, A.; Lee, H.-W.; Tsao, H. N.; Yi, C.; Chandiran, A. K.; Nazeeruddin, M. K.; Diao, E. W.-G.; Yeh, C.-Y.; Zakeeruddin, S. M.; Grätzel, M., Porphyrin-Sensitized Solar Cells with Cobalt (II/III)-Based Redox Electrolyte Exceed 12 Percent Efficiency. *Science* **2011**, *334* (6056), 629-634.

38. Bessho, T.; Zakeeruddin, S. M.; Yeh, C.-Y.; Diau, E. W.-G.; Grätzel, M., Highly Efficient Mesoscopic Dye-Sensitized Solar Cells Based on Donor–Acceptor-Substituted Porphyrins. *Angew. Chem. Int. Ed.* **2010**, *49* (37), 6646-6649.
39. Garland, M. J.; Cassidy, C. M.; Woolfson, D.; Donnelly, R. F., Designing photosensitizers for photodynamic therapy: strategies, challenges and promising developments. *Future Med. Chem.* **2009**, *1* (4), 667-691.
40. Ethirajan, M.; Chen, Y.; Joshi, P.; Pandey, R. K., The role of porphyrin chemistry in tumor imaging and photodynamic therapy. *Chem. Soc. Rev.* **2011**, *40* (1), 340-362.
41. Huang, Z., A Review of Progress in Clinical Photodynamic Therapy. *Technol. Cancer Res. Treat.* **2005**, *4* (3), 283-293.
42. Gouterman, M., Study of the Effects of Substitution on the Absorption Spectra of Porphin. *J. Chem. Phys.* **1959**, *30* (5), 1139-1161.
43. Gouterman, M., Spectra of porphyrins. *J. Mol. Spectrosc.* **1961**, *6* (0), 138-163.
44. Gouterman, M.; Wagnière, G. H.; Snyder, L. C., Spectra of porphyrins. *J. Mol. Spectrosc.* **1963**, *11* (1), 108-127.
45. Senge, M. O.; Ryan, A. A.; Letchford, K. A.; MacGowan, S. A.; Mielke, T., Chlorophylls, Symmetry, Chirality, and Photosynthesis. *Symmetry* **2014**, *6* (3), 781-843.
46. Jeong, Y.-H.; Yoon, H.-J.; Jang, W.-D., Dendrimer porphyrin-based self-assembled nano-devices for biomedical applications. *Polym. J.* **2012**, *44* (6), 512-521.
47. Duncan, T. V.; Susumu, K.; Sinks, L. E.; Therien, M. J., Exceptional Near-Infrared Fluorescence Quantum Yields and Excited-State Absorptivity of Highly Conjugated Porphyrin Arrays. *J. Am. Chem. Soc.* **2006**, *128* (28), 9000-9001.
48. Susumu, K.; Therien, M. J., Decoupling Optical and Potentiometric Band Gaps in π -Conjugated Materials. *J. Am. Chem. Soc.* **2002**, *124* (29), 8550-8552.
49. Shediach, R.; Gray, M. H. B.; Uyeda, H. T.; Johnson, R. C.; Hupp, J. T.; Angiolillo, P. J.; Therien, M. J., Singlet and Triplet Excited States of Emissive, Conjugated Bis(porphyrin) Compounds Probed by Optical and EPR Spectroscopic Methods. *J. Am. Chem. Soc.* **2000**, *122* (29), 7017-7033.
50. Kumble, R.; Palese, S.; Lin, V. S.-Y.; Therien, M. J.; Hochstrasser, R. M., Ultrafast Dynamics of Highly Conjugated Porphyrin Arrays. *J. Am. Chem. Soc.* **1998**, *120* (44), 11489-11498.
51. Lin, V. S.-Y.; Therien, M. J., The Role of Porphyrin-to-Porphyrin Linkage Topology in the Extensive Modulation of the Absorptive and Emissive Properties of a

Series of Ethynyl- and Butadiynyl-Bridged Bis- and Tris(porphinato)zinc Chromophores. *Chem. Eur. J* **1995**, *1* (9), 645-651.

52. Lin, V. S.-Y.; DiMagno, S. G.; Therien, M. J., Highly conjugated, acetylenyl bridged porphyrins: new models for light-harvesting antenna systems. *Science* **1994**, *264* (5162), 1105-1111.
53. Caspar, J. V.; Kober, E. M.; Sullivan, B. P.; Meyer, T. J., Application of the energy gap law to the decay of charge-transfer excited states. *J. Am. Chem. Soc.* **1982**, *104* (2), 630-632.
54. Kasha, M.; Rawls, H. R.; Ashraf El-Bayoumi, M., The exciton model in molecular spectroscopy. *Pure Appl. Chem.* **1965**, *11*, 371-392.
55. Discher, B. M.; Won, Y.-Y.; Ege, D. S.; Lee, J. C.-M.; Bates, F. S.; Discher, D. E.; Hammer, D. A., Polymersomes: Tough Vesicles Made from Diblock Copolymers. *Science* **1999**, *284* (5417), 1143-1146.
56. Discher, D. E.; Ahmed, F., Polymersomes. *Annu. Rev. Biomed. Eng.* **2006**, *8*, 323-41.
57. Levine, D. H.; Ghoroghchian, P. P.; Freudenberg, J.; Zhang, G.; Therien, M. J.; Greene, M. I.; Hammer, D. A.; Murali, R., Polymersomes: A new multi-functional tool for cancer diagnosis and therapy. *Methods* **2008**, *46* (1), 25-32.
58. Ghoroghchian, P. P.; Frail, P. R.; Susumu, K.; Blessington, D.; Brannan, A. K.; Bates, F. S.; Chance, B.; Hammer, D. A.; Therien, M. J., Near-infrared-emissive polymersomes: Self-assembled soft matter for in vivo optical imaging. *Proceedings of the National Academy of Sciences of the United States of America* **2005**, *102* (8), 2922-2927.
59. Ghoroghchian, P. P.; Frail, P. R.; Susumu, K.; Park, T.-H.; Wu, S. P.; Uyeda, H. T.; Hammer, D. A.; Therien, M. J., Broad Spectral Domain Fluorescence Wavelength Modulation of Visible and Near-Infrared Emissive Polymersomes. *J. Am. Chem. Soc.* **2005**, *127* (44), 15388-15390.
60. Ghoroghchian, P. P.; Frail, P. R.; Li, G.; Zupancich, J. A.; Bates, F. S.; Hammer, D. A.; Therien, M. J., Controlling Bulk Optical Properties of Emissive Polymersomes through Intramembranous Polymer-Fluorophore Interactions. *Chem. Mater.* **2007**, *19* (6), 1309-1318.
61. Ghoroghchian, P. P.; Li, G.; Levine, D. H.; Davis, K. P.; Bates, F. S.; Hammer, D. A.; Therien, M. J., Bioresorbable Vesicles Formed through Spontaneous Self-Assembly of Amphiphilic Poly(ethylene oxide)-block-polycaprolactone. *Macromolecules* **2006**, *39* (5), 1673-1675.
62. Christian, N. A.; Milone, M. C.; Ranka, S. S.; Li, G.; Frail, P. R.; Davis, K. P.; Bates, F. S.; Therien, M. J.; Ghoroghchian, P. P.; June, C. H.; Hammer, D. A., Tat-Functionalized

- Near-Infrared Emissive Polymersomes for Dendritic Cell Labeling. *Bioconj. Chem.* **2007**, *18* (1), 31-40.
63. Helmchen, F.; Denk, W., Deep tissue two-photon microscopy. *Nat. Meth.* **2005**, *2* (12), 932-940.
64. Hong, G.; Diao, S.; Chang, J.; Antaris, A. L.; Chen, C.; Zhang, B.; Zhao, S.; Atochin, D. N.; Huang, P. L.; Andreasson, K. I.; Kuo, C. J.; Dai, H., Through-skull fluorescence imaging of the brain in a new near-infrared window. *Nature Photon.* **2014**, *8* (9), 723-730.
65. Yaroslavsky, A. N.; Schulze, P. C.; Yaroslavsky, I. V.; Schober, R.; Ulrich, F.; Schwarzmaier, H. J., Optical properties of selected native and coagulated human brain tissues in vitro in the visible and near infrared spectral range. *Phys. Med. Biol.* **2002**, *47* (12), 2059-2073.
66. Cheong, W. F.; Prael, S. A.; Welch, A. J., A Review of the Optical-Properties of Biological Tissues. *Ieee J. Quantum Elect.* **1990**, *26* (12), 2166-2185.
67. Sarder, P.; Yazdanfar, S.; Akers, W. J.; Tang, R.; Sudlow, G. P.; Egbulefu, C.; Achilefu, S., All-near-infrared multiphoton microscopy interrogates intact tissues at deeper imaging depths than conventional single- and two-photon near-infrared excitation microscopes. *J. Biomed. Opt.* **2013**, *18* (10).
68. Huang, S.; Heikal, A. A.; Webb, W. W., Two-Photon Fluorescence Spectroscopy and Microscopy of NAD(P)H and Flavoprotein. *Biophys. J.* **2002**, *82* (5), 2811-2825.
69. Berezin, M. Y.; Zhan, C.; Lee, H.; Joo, C.; Akers, W. J.; Yazdanfar, S.; Achilefu, S., Two-Photon Optical Properties of Near-Infrared Dyes at 1.55 μm Excitation. *J. Phys. Chem. B* **2011**, *115* (39), 11530-11535.
70. Kruk, M.; Karotki, A.; Drobizhev, M.; Kuzmitsky, V.; Gael, V.; Rebane, A., Two-photon absorption of tetraphenylporphyrin free base. *J. Lumin.* **2003**, *105* (1), 45-55.
71. Karotki, A.; Drobizhev, M.; Kruk, M.; Spangler, C.; Nickel, E.; Mamardashvili, N.; Rebane, A., Enhancement of two-photon absorption in tetrapyrrolic compounds. *J. Opt. Soc. Am. B* **2003**, *20* (2), 321-332.
72. Nowak-Król, A.; Wilson, C. J.; Drobizhev, M.; Kondratuk, D. V.; Rebane, A.; Anderson, H. L.; Gryko, D. T., Amplified Two-Photon Absorption in Trans-A2B2-Porphyrins Bearing Nitrophenylethynyl Substituents. *ChemPhysChem* **2012**, *13* (17), 3966-3972.
73. Ryan, A.; Gehrold, A.; Perusitti, R.; Pintea, M.; Fazekas, M.; Locos, O. B.; Blaikie, F.; Senge, M. O., Porphyrin Dimers and Arrays. *Eur. J. Org. Chem.* **2011**, *2011* (29), 5817-5844.

74. Drobizhev, M.; Karotki, A.; Kruk, M.; Krivokapic, A.; Anderson, H. L.; Rebane, A., Photon energy upconversion in porphyrins: one-photon hot-band absorption versus two-photon absorption. *Chem. Phys. Lett.* **2003**, *370* (5–6), 690-699.
75. Drobizhev, M.; Stepanenko, Y.; Dzenis, Y.; Karotki, A.; Rebane, A.; Taylor, P. N.; Anderson, H. L., Understanding Strong Two-Photon Absorption in π -Conjugated Porphyrin Dimers via Double-Resonance Enhancement in a Three-Level Model. *J. Am. Chem. Soc.* **2004**, *126* (47), 15352-15353.
76. Drobizhev, M.; Stepanenko, Y.; Dzenis, Y.; Karotki, A.; Rebane, A.; Taylor, P. N.; Anderson, H. L., Extremely Strong Near-IR Two-Photon Absorption in Conjugated Porphyrin Dimers: Quantitative Description with Three-Essential-States Model. *J. Phys. Chem. B* **2005**, *109* (15), 7223-7236.
77. Yoon, M. C.; Noh, S. B.; Tsuda, A.; Nakamura, Y.; Osuka, A.; Kim, D., Photophysics of meso-beta doubly linked Ni(II) porphyrin arrays: Large two-photon absorption cross-section and fast energy relaxation dynamics. *J. Am. Chem. Soc.* **2007**, *129* (33), 10080-+.
78. Thorley, K. J.; Hales, J. M.; Anderson, H. L.; Perry, J. W., Porphyrin Dimer Carbocations with Strong Near Infrared Absorption and Third-Order Optical Nonlinearity. *Angew. Chem. Int. Ed.* **2008**, *47* (37), 7095-7098.
79. Pawlicki, M.; Morisue, M.; Davis, N. K. S.; McLean, D. G.; Haley, J. E.; Beuerman, E.; Drobizhev, M.; Rebane, A.; Thompson, A. L.; Pascu, S. I.; Accorsi, G.; Armaroli, N.; Anderson, H. L., Engineering conjugation in para-phenylene-bridged porphyrin tapes. *Chem. Sci.* **2012**, *3* (5), 1541-1547.
80. Park, J. K.; Fischer, M. C.; Susumu, K.; Therien, M. J.; Warren, W. S., Femtosecond pulse train shaping improves two-photon excited fluorescence measurements. *Opt. Lett.* **2014**, *39* (19), 5606-5609.
81. Pawlicki, M.; Collins, H. A.; Denning, R. G.; Anderson, H. L., Two-Photon Absorption and the Design of Two-Photon Dyes. *Angew. Chem. Int. Ed.* **2009**, *48* (18), 3244-3266.
82. Fisher, J. A. N.; Susumu, K.; Therien, M. J.; Yodh, A. G., One- and two-photon absorption of highly conjugated multiporphyrin systems in the two-photon Soret transition region. *J. Chem. Phys.* **2009**, *130* (13), 134506.
83. Duncan, T. V.; Rubtsov, I. V.; Uyeda, H. T.; Therien, M. J., Highly conjugated (polypyridyl)metal-(porphinato)zinc(II) compounds: Long-lived, high oscillator strength, excited-state absorbers having exceptional spectral coverage of the near-infrared. *J. Am. Chem. Soc.* **2004**, *126* (31), 9474-9475.

84. Rubtsov, I. V.; Susumu, K.; Rubtsov, G. I.; Therien, M. J., Ultrafast Singlet Excited-State Polarization in Electronically Asymmetric Ethyne-Bridged Bis[(porphinato)zinc(II)] Complexes. *J. Am. Chem. Soc.* **2003**, *125* (9), 2687-2696.
85. Fletcher, J. T.; Therien, M. J., Extreme electronic modulation of the cofacial porphyrin structural motif. *J. Am. Chem. Soc.* **2002**, *124* (16), 4298-4311.
86. Angiolillo, P. J.; Lin, V. S.-Y.; Vanderkooi, J. M.; Therien, M. J., EPR Spectroscopy and Photophysics of the Lowest Photoactivated Triplet State of a Series of Highly Conjugated (Porphinato)Zn Arrays. *J. Am. Chem. Soc.* **1995**, *117* (50), 12514-12527.
87. Beljonne, D.; O'Keefe, G. E.; Hamer, P. J.; Friend, R. H.; Anderson, H. L.; Brédas, J. L., Investigation of the linear and nonlinear optical response of edge-linked conjugated zinc porphyrin oligomers by optical spectroscopy and configuration interaction techniques. *J. Chem. Phys.* **1997**, *106* (23), 9439-9460.
88. Ohira, S.; Bredas, J.-L., Porphyrin dimers: A theoretical understanding of the impact of electronic coupling strength on the two-photon absorption properties. *J. Mater. Chem.* **2009**, *19* (40), 7545-7550.
89. Goerigk, L.; Moellmann, J.; Grimme, S., Computation of accurate excitation energies for large organic molecules with double-hybrid density functionals. *Phys. Chem. Chem. Phys.* **2009**, *11* (22), 4611-4620.
90. Becke, A. D., Density-functional thermochemistry. III. The role of exact exchange. *J. Chem. Phys.* **1993**, *98* (7), 5648-5652.
91. Lee, C.; Yang, W.; Parr, R. G., Development of the Colle-Salvetti correlation-energy formula into a functional of the electron density. *Phys. Rev. B* **1988**, *37* (2), 785-789.
92. Miehlich, B.; Savin, A.; Stoll, H.; Preuss, H., Results obtained with the correlation energy density functionals of Becke and Lee, Yang and Parr. *Chem. Phys. Lett.* **1989**, *157* (3), 200-206.
93. Grimme, S.; Parac, M., Substantial Errors from Time-Dependent Density Functional Theory for the Calculation of Excited States of Large π Systems. *ChemPhysChem* **2003**, *4* (3), 292-295.
94. Peverati, R.; Truhlar, D. G., Improving the Accuracy of Hybrid Meta-GGA Density Functionals by Range Separation. *J. Phys. Chem. Lett.* **2011**, *2* (21), 2810-2817.
95. Vydrov, O. A.; Scuseria, G. E., Assessment of a long-range corrected hybrid functional. *J. Chem. Phys.* **2006**, *125* (23), 234109.
96. Winters, M. U.; Kärnbratt, J.; Eng, M.; Wilson, C. J.; Anderson, H. L.; Albinsson, B., Photophysics of a Butadiyne-Linked Porphyrin Dimer: Influence of Conformational

- Flexibility in the Ground and First Singlet Excited State. *J. Phys. Chem. C* **2007**, *111* (19), 7192-7199.
97. Angiolillo, P. J.; Rawson, J.; Frail, P. R.; Therien, M. J., The evolution of spin distribution in the photoexcited triplet state of ethyne-elaborated porphyrins. *Chem. Commun.* **2013**, *49* (84), 9722-9724.
98. Ahn, T. K.; Kim, K. S.; Kim, D. Y.; Noh, S. B.; Aratani, N.; Ikeda, C.; Osuka, A.; Kim, D., Relationship between Two-Photon Absorption and the π -Conjugation Pathway in Porphyrin Arrays through Dihedral Angle Control. *J. Am. Chem. Soc.* **2006**, *128* (5), 1700-1704.
99. Hisaki, I.; Hiroto, S.; Kim, K. S.; Noh, S. B.; Kim, D.; Shinokubo, H.; Osuka, A., Synthesis of doubly beta-to-beta 1,3-butadiyne-bridged diporphyrins: Enforced planar structures and large two-photon absorption cross sections. *Angew. Chem. Int. Ed.* **2007**, *46* (27), 5125-5128.
100. Karotki, A.; Drobizhev, M.; Dzenis, Y.; Taylor, P. N.; Anderson, H. L.; Rebane, A., Dramatic enhancement of intrinsic two-photon absorption in a conjugated porphyrin dimer. *Phys. Chem. Chem. Phys.* **2004**, *6* (1), 7-10.
101. Kurotobi, K.; Kim, K. S.; Noh, S. B.; Kim, D.; Osuka, A., A quadruply azulene-fused porphyrin with intense near-IR absorption and a large two-photon absorption cross section. *Angew. Chem. Int. Ed.* **2006**, *45* (24), 3944-3947.
102. Ahn, T. K.; Kwon, J. H.; Kim, D. Y.; Cho, D. W.; Jeong, D. H.; Kim, S. K.; Suzuki, M.; Shimizu, S.; Osuka, A.; Kim, D., Comparative Photophysics of [26]- and [28]Hexaphyrins(1.1.1.1.1.1): Large Two-Photon Absorption Cross Section of Aromatic [26]Hexaphyrins(1.1.1.1.1.1). *J. Am. Chem. Soc.* **2005**, *127* (37), 12856-12861.
103. Chung, S.-J.; Zheng, S.; Odani, T.; Beverina, L.; Fu, J.; Padilha, L. A.; Biesso, A.; Hales, J. M.; Zhan, X.; Schmidt, K.; Ye, A.; Zojer, E.; Barlow, S.; Hagan, D. J.; Van Stryland, E. W.; Yi, Y.; Shuai, Z.; Pagani, G. A.; Brédas, J.-L.; Perry, J. W.; Marder, S. R., Extended Squaraine Dyes with Large Two-Photon Absorption Cross-Sections. *J. Am. Chem. Soc.* **2006**, *128* (45), 14444-14445.
104. Drobizhev, M.; Stepanenko, Y.; Rebane, A.; Wilson, C. J.; Screen, T. E. O.; Anderson, H. L., Strong Cooperative Enhancement of Two-Photon Absorption in Double-Strand Conjugated Porphyrin Ladder Arrays. *J. Am. Chem. Soc.* **2006**, *128* (38), 12432-12433.
105. Kim, D. Y.; Ahn, T. K.; Kwon, J. H.; Kim, D.; Ikeue, T.; Aratani, N.; Osuka, A.; Shigeiwa, M.; Maeda, S., Large Two-Photon Absorption (TPA) Cross-Section of Directly Linked Fused Diporphyrins. *J. Phys. Chem. A* **2005**, *109* (13), 2996-2999.

106. Ogawa, K.; Ohashi, A.; Kobuke, Y.; Kamada, K.; Ohta, K., Strong Two-Photon Absorption of Self-Assembled Butadiyne-Linked Bisporphyrin. *J. Am. Chem. Soc.* **2003**, *125* (44), 13356-13357.
107. Drobizhev, M.; Makarov, N. S.; Tillo, S. E.; Hughes, T. E.; Rebane, A., Two-photon absorption properties of fluorescent proteins. *Nat Meth* **2011**, *8* (5), 393-399.
108. Albota, M.; Beljonne, D.; Brédas, J.-L.; Ehrlich, J. E.; Fu, J.-Y.; Heikal, A. A.; Hess, S. E.; Kogej, T.; Levin, M. D.; Marder, S. R.; McCord-Maughon, D.; Perry, J. W.; Röckel, H.; Rumi, M.; Subramaniam, G.; Webb, W. W.; Wu, X.-L.; Xu, C., Design of Organic Molecules with Large Two-Photon Absorption Cross Sections. *Science* **1998**, *281* (5383), 1653-1656.
109. Chen, C.; Lu, J. Q.; Ding, H. F.; Jacobs, K. M.; Du, Y.; Hu, X. H., A primary method for determination of optical parameters of turbid samples and application to intralipid between 550 and 1630nm. *Opt. Express* **2006**, *14* (16), 7420-7435.
110. Ghoroghchian, P. P.; Lin, J. J.; Brannan, A. K.; Frail, P. R.; Bates, F. S.; Therien, M. J.; Hammer, D. A., Quantitative membrane loading of polymer vesicles. *Soft Matter* **2006**, *2* (11), 973-980.
111. Duncan, T. V.; Ghoroghchian, P. P.; Rubtsov, I. V.; Hammer, D. A.; Therien, M. J., Ultrafast Excited-State Dynamics of Nanoscale Near-Infrared Emissive Polymersomes. *J. Am. Chem. Soc.* **2008**, *130* (30), 9773-9784.
112. Ghoroghchian, P. P.; Therien, M. J.; Hammer, D. A., In vivo fluorescence imaging: a personal perspective. *Wiley Interdiscip. Rev. Nanomed. Nanobiotechnol.* **2009**, *1* (2), 156-167.
113. Kamat, N. P.; Robbins, G. P.; Rawson, J.; Therien, M. J.; Dmochowski, I. J.; Hammer, D. A., A Generalized System for Photoresponsive Membrane Rupture in Polymersomes. *Adv. Funct. Mater.* **2010**, *20* (16), 2588-2596.
114. Griepenburg, J. C.; Sood, N.; Vargo, K. B.; Williams, D.; Rawson, J.; Therien, M. J.; Hammer, D. A.; Dmochowski, I. J., Caging Metal Ions with Visible Light-Responsive Nanopolymersomes. *Langmuir* **2015**, *31* (2), 799-807.
115. Kamat, N. P.; Liao, Z. Z.; Moses, L. E.; Rawson, J.; Therien, M. J.; Dmochowski, I. J.; Hammer, D. A., Sensing membrane stress with near IR-emissive porphyrins. *Proc. Natl. Acad. Sci. U. S. A.* **2011**, *108* (34), 13984-13989.
116. Robbins, G. P.; Jimbo, M.; Swift, J.; Therien, M. J.; Hammer, D. A.; Dmochowski, I. J., Photoinitiated Destruction of Composite Porphyrin-Protein Polymersomes. *J. Am. Chem. Soc.* **2009**, *131* (11), 3872-3874.

117. Christian, N. A.; Benencia, F.; Milone, M. C.; Li, G. Z.; Frail, P. R.; Therien, M. J.; Coukos, G.; Hammer, D. A., In Vivo Dendritic Cell Tracking Using Fluorescence Lifetime Imaging and Near-Infrared-Emissive Polymersomes. *Mol. Imag. Biol.* **2009**, *11* (3), 167-177.
118. Hammer, D. A.; Robbins, G. P.; Haun, J. B.; Lin, J. J.; Qi, W.; Smith, L. A.; Ghoroghchian, P. P.; Therien, M. J.; Bates, F. S., Leuko-polymersomes. *Faraday Discuss.* **2008**, *139*, 129-141.
119. Strehmel, B.; Sarker, A. M.; Detert, H., The influence of sigma and pi acceptors on two-photon absorption and solvatochromism of dipolar and quadrupolar unsaturated organic compounds. *Chemphyschem* **2003**, *4* (3), 249-259.
120. Rumi, M.; Ehrlich, J. E.; Heikal, A. A.; Perry, J. W.; Barlow, S.; Hu, Z.; McCord-Maughon, D.; Parker, T. C.; Röckel, H.; Thayumanavan, S.; Marder, S. R.; Beljonne, D.; Brédas, J.-L., Structure-Property Relationships for Two-Photon Absorbing Chromophores: Bis-Donor Diphenylpolyene and Bis(styryl)benzene Derivatives. *J. Am. Chem. Soc.* **2000**, *122* (39), 9500-9510.
121. Welsher, K.; Sherlock, S. P.; Dai, H., Deep-tissue anatomical imaging of mice using carbon nanotube fluorophores in the second near-infrared window. *Proc. Natl. Acad. Sci. U.S.A.* **2011**, *108* (22), 8943-8948.
122. Williams-Harry, M.; Bhaskar, A.; Ramakrishna, G.; Goodson, T.; Imamura, M.; Mawatari, A.; Nakao, K.; Enozawa, H.; Nishinaga, T.; Iyoda, M., Giant Thienylene-Acetylene-Ethylene Macrocycles with Large Two-Photon Absorption Cross Section and Semishape-Persistence. *J. Am. Chem. Soc.* **2008**, *130* (11), 3252-3253.
123. Wilkinson, J. D.; Wicks, G.; Nowak-Krol, A.; Lukasiewicz, L. G.; Wilson, C. J.; Drobizhev, M.; Rebane, A.; Gryko, D. T.; Anderson, H. L., Two-photon absorption in butadiyne-linked porphyrin dimers: torsional and substituent effects. *J. Mater. Chem. C* **2014**, *2* (33), 6802-6809.
124. Raymond, J. E.; Bhaskar, A.; Goodson, T.; Makiuchi, N.; Ogawa, K.; Kobuke, Y., Synthesis and Two-Photon Absorption Enhancement of Porphyrin Macrocycles. *J. Am. Chem. Soc.* **2008**, *130* (51), 17212-17213.
125. Collins, H. A.; Khurana, M.; Moriyama, E. H.; Mariampillai, A.; Dahlstedt, E.; Balaz, M.; Kuimova, M. K.; Drobizhev, M.; YangVictor, X. D.; Phillips, D.; Rebane, A.; Wilson, B. C.; Anderson, H. L., Blood-vessel closure using photosensitizers engineered for two-photon excitation. *Nature Photon.* **2008**, *2* (7), 420-424.
126. Derfus, A. M.; Chan, W. C. W.; Bhatia, S. N., Probing the Cytotoxicity of Semiconductor Quantum Dots. *Nano Lett.* **2004**, *4* (1), 11-18.

127. Kirchner, C.; Liedl, T.; Kudera, S.; Pellegrino, T.; Muñoz Javier, A.; Gaub, H. E.; Stölzle, S.; Fertig, N.; Parak, W. J., Cytotoxicity of Colloidal CdSe and CdSe/ZnS Nanoparticles. *Nano Lett.* **2005**, *5* (2), 331-338.
128. Lovrić, J.; Cho, S. J.; Winnik, F. M.; Maysinger, D., Unmodified Cadmium Telluride Quantum Dots Induce Reactive Oxygen Species Formation Leading to Multiple Organelle Damage and Cell Death. *Chemistry & Biology* **2005**, *12* (11), 1227-1234.
129. Hauck, T. S.; Anderson, R. E.; Fischer, H. C.; Newbigging, S.; Chan, W. C. W., In vivo Quantum-Dot Toxicity Assessment. *Small* **2010**, *6* (1), 138-144.
130. Wu, S. P.; Lee, I.; Ghoroghchian, P. P.; Frail, P. R.; Zheng, G.; Glickson, J. D.; Therien, M. J., Near-Infrared Optical Imaging of B16 Melanoma Cells via Low-Density Lipoprotein-Mediated Uptake and Delivery of High Emission Dipole Strength Tris[(porphinato)zinc(II)] Fluorophores. *Bioconj. Chem.* **2005**, *16* (3), 542-550.
131. Discher, D. E.; Eisenberg, A., Polymer Vesicles. *Science* **2002**, *297* (5583), 967-973.
132. Katz, J. S.; Eisenbrown, K. A.; Johnston, E. D.; Kamat, N. P.; Rawson, J.; Therien, M. J.; Burdick, J. A.; Hammer, D. A., Soft biodegradable polymersomes from caprolactone-derived polymers. *Soft Matter* **2012**, *8* (42), 10853-10862.
133. Qi, W.; Ghoroghchian, P. P.; Li, G. Z.; Hammer, D. A.; Therien, M. J., Aqueous self-assembly of poly(ethylene oxide)-block-poly(epsilon-caprolactone) (PEO-b-PCL) copolymers: disparate diblock copolymer compositions give rise to nano- and meso-scale bilayered vesicles. *Nanoscale* **2013**, *5* (22), 10908-10915.
134. Discher, B. M.; Bermudez, H.; Hammer, D. A.; Discher, D. E.; Won, Y.-Y.; Bates, F. S., Cross-linked Polymersome Membranes: Vesicles with Broadly Adjustable Properties. *J. Phys. Chem. B* **2002**, *106* (11), 2848-2854.
135. Robbins, G. P.; Saunders, R. L.; Haun, J. B.; Rawson, J.; Therien, M. J.; Hammer, D. A., Tunable Leuko-polymersomes That Adhere Specifically to Inflammatory Markers. *Langmuir* **2010**, *26* (17), 14089-14096.
136. Robbins, G. P.; Lee, D.; Katz, J. S.; Frail, P. R.; Therien, M. J.; Crocker, J. C.; Hammer, D. A., Effects of membrane rheology on leuko-polymersome adhesion to inflammatory ligands. *Soft Matter* **2011**, *7* (2), 769-779.
137. Lee, J. C. M.; Bermudez, H.; Discher, B. M.; Sheehan, M. A.; Won, Y.-Y.; Bates, F. S.; Discher, D. E., Preparation, stability, and in vitro performance of vesicles made with diblock copolymers. *Biotechnol. Bioeng.* **2001**, *73* (2), 135-145.
138. Maeda, H., Macromolecular therapeutics in cancer treatment: The EPR effect and beyond. *J. Controlled Release* **2012**, *164* (2), 138-144.

139. Won, Y.-Y.; Brannan, A. K.; Davis, H. T.; Bates, F. S., Cryogenic Transmission Electron Microscopy (Cryo-TEM) of Micelles and Vesicles Formed in Water by Poly(ethylene oxide)-Based Block Copolymers. *J. Phys. Chem. B* **2002**, *106* (13), 3354-3364.
140. Palmer, K. F.; Williams, D., Optical properties of water in the near infrared. *J. Opt. Soc. Am.* **1974**, *64* (8), 1107-1110.
141. Huang, Q.; Shan, S.; Braun, R. D.; Lanzen, J.; Anyrhambatla, G.; Kong, G.; Borelli, M.; Corry, P.; Dewhirst, M. W.; Li, C.-Y., Noninvasive visualization of tumors in rodent dorsal skin window chambers. *Nat Biotech* **1999**, *17* (10), 1033-1035.
142. Palmer, G. M.; Fontanella, A. N.; Shan, S.; Hanna, G.; Zhang, G.; Fraser, C. L.; Dewhirst, M. W., In vivo optical molecular imaging and analysis in mice using dorsal window chamber models applied to hypoxia, vasculature and fluorescent reporters. *Nat. Protocols* **2011**, *6* (9), 1355-1366.
143. Hale, G. M.; Querry, M. R., Optical Constants of Water in the 200-nm to 200- μ m Wavelength Region. *Appl. Opt.* **1973**, *12* (3), 555-563.
144. Photos, P. J.; Bacakova, L.; Discher, B.; Bates, F. S.; Discher, D. E., Polymer vesicles in vivo: correlations with PEG molecular weight. *J. Controlled Release* **2003**, *90* (3), 323-334.
145. Cox, C. L.; Denk, W.; Tank, D. W.; Svoboda, K., Action potentials reliably invade axonal arbors of rat neocortical neurons. *Proc. Natl. Acad. Sci. U.S.A.* **2000**, *97* (17), 9724-9728.
146. Hisaki, I.; Hiroto, S.; Kim, K. S.; Noh, S. B.; Kim, D.; Shinokubo, H.; Osuka, A., Synthesis of Doubly β -to- β 1,3-Butadiyne-Bridged Diporphyrins: Enforced Planar Structures and Large Two-Photon Absorption Cross Sections. *Angew. Chem. Int. Ed.* **2007**, *46* (27), 5125-5128.
147. Odom, S. A.; Webster, S.; Padilha, L. A.; Peceli, D.; Hu, H.; Nootz, G.; Chung, S.-J.; Ohira, S.; Matichak, J. D.; Przhonska, O. V.; Kachkovski, A. D.; Barlow, S.; Brédas, J.-L.; Anderson, H. L.; Hagan, D. J.; Van Stryland, E. W.; Marder, S. R., Synthesis and Two-Photon Spectrum of a Bis(Porphyrin)-Substituted Squaraine. *J. Am. Chem. Soc.* **2009**, *131* (22), 7510-7511.
148. Zhang, L.; Allen, S. D.; Woelfle, C.; Zhang, F., Influence of Polymer Structures on Optical Power Limiting Performance of Single-Walled Carbon Nanotubes. *J. Phys. Chem. C* **2009**, *113* (31), 13979-13984.
149. Anderson, H. L., Conjugated Porphyrin Ladders. *Inorg. Chem.* **1994**, *33* (5), 972-981.

150. Kim, K. S.; Noh, S. B.; Katsuda, T.; Ito, S.; Osuka, A.; Kim, D., Charge transfer induced enhancement of near-IR two-photon absorption of 5,15-bis(azulenylethynyl) zinc(ii) porphyrins. *Chem. Commun.* **2007**, (24), 2479-2481.
151. Sheik-Bahae, M.; Said, A. A.; Wei, T. H.; Hagan, D. J.; Van Stryland, E. W., Sensitive measurement of optical nonlinearities using a single beam. *Ieee J. Quantum Elect.* **1990**, 26 (4), 760-769.
152. Zhao, M.; Cui, Y.; Samoc, M.; Prasad, P. N.; Unroe, M. R.; Reinhardt, B. A., Influence of two-photon absorption on third-order nonlinear optical processes as studied by degenerate four-wave mixing: The study of soluble didecyloxy substituted polyphenyls. *J. Chem. Phys.* **1991**, 95 (6), 3991-4001.
153. Tian, P.; Warren, W. S., Ultrafast measurement of two-photon absorption by loss modulation. *Opt. Lett.* **2002**, 27 (18), 1634-1636.
154. Fischer, M. C.; Ye, T.; Yurtsever, G.; Miller, A.; Ciocca, M.; Wagner, W.; Warren, W. S., Two-photon absorption and self-phase modulation measurements with shaped femtosecond laser pulses. *Opt. Lett.* **2005**, 30 (12), 1551-1553.
155. Denk, W. P., D. W.; Webb, W. W. , Multi-Photon Molecular Excitation in Laser-Scanning Microscopy. In *Handbook of biological confocal microscopy*, 3rd ed.; Pawley, J. B., Ed. Springer: New York, NY, 2006; pp 535-549.
156. Xu, C. Z., W. R. , Multiphoton Excitation of Fluorescent Probes. In *Handbook of biomedical nonlinear optical microscopy*, Masters, B. R.; So, P. T. C., Eds. Oxford University Press: New York, 2008; pp 311-333.
157. Englman, R.; Jortner, J., The energy gap law for radiationless transitions in large molecules. *Mol. Phys.* **1970**, 18 (2), 145-164.
158. Panchuk-Voloshina, N.; Haugland, R. P.; Bishop-Stewart, J.; Bhalgat, M. K.; Millard, P. J.; Mao, F.; Leung, W.-Y.; Haugland, R. P., Alexa Dyes, a Series of New Fluorescent Dyes that Yield Exceptionally Bright, Photostable Conjugates. *Journal of Histochemistry & Cytochemistry* **1999**, 47 (9), 1179-1188.
159. Escobedo, J. O.; Rusin, O.; Lim, S.; Strongin, R. M., NIR dyes for bioimaging applications. *Curr. Opin. Chem. Biol.* **2010**, 14 (1), 64-70.
160. Frangioni, J. V., In vivo near-infrared fluorescence imaging. *Curr. Opin. Chem. Biol.* **2003**, 7 (5), 626-634.
161. Licha, K.; Riefke, B.; Ntziachristos, V.; Becker, A.; Chance, B.; Semmler, W., Hydrophilic Cyanine Dyes as Contrast Agents for Near-infrared Tumor Imaging: Synthesis, Photophysical Properties and Spectroscopic In vivo Characterization. *Photochem. Photobiol.* **2000**, 72 (3), 392-398.

162. Tatarskiy, A. L.; Fedyunayeva, I. A.; Dyubko, T. S.; Povrozin, Y. A.; Doroshenko, A. O.; Terpetschnig, E. A.; Patsenker, L. D., Synthesis of water-soluble, ring-substituted squaraine dyes and their evaluation as fluorescent probes and labels. *Anal. Chim. Acta* **2006**, *570* (2), 214-223.
163. Russin, T. J.; et al., Measuring the fluorescent quantum efficiency of indocyanine green encapsulated in nanocomposite particulates. *J. Phys.: Condens. Matter* **2010**, *22* (33), 334217.
164. Shediach, R.; Gray, M. H. B.; Uyeda, H. T.; Johnson, R. C.; Hupp, J. T.; Angiolillo, P. J.; Therien, M. J., Singlet and Triplet Excited States of Emissive, Conjugated Bis(porphyrin) Compounds Probed by Optical and EPR Spectroscopic Methods. *J. Am. Chem. Soc.* **2000**, *122* (29), 7017-7033.
165. Ghoroghchian, P. P.; Frail, P. R.; Susumu, K.; Blessington, D.; Brannan, A. K.; Bates, F. S.; Chance, B.; Hammer, D. A.; Therien, M. J., Near-infrared-emissive polymersomes: Self-assembled soft matter for in vivo optical imaging. *Proc. Natl. Acad. Sci. U. S. A.* **2005**, *102* (8), 2922-2927.
166. Ghoroghchian, P. P.; Frail, P. R.; Susumu, K.; Park, T.-H.; Wu, S. P.; Uyeda, H. T.; Hammer, D. A.; Therien, M. J., Broad Spectral Domain Fluorescence Wavelength Modulation of Visible and Near-Infrared Emissive Polymersomes. *J. Am. Chem. Soc.* **2005**, *127* (44), 15388-15390.
167. Sunar, U.; Ghoroghchian, P. P.; Intes, X.; Therien, M. J.; Hammer, D. A.; Yodh, A. G., Pharmacokinetic assessment of a polymersome-based molecular beacon by in vivo fluorescence monitoring - art. no. 64342I. *P Soc Photo-Opt Ins* **2007**, *6434*, I4342-I4342.
168. Susumu, K.; Duncan, T. V.; Therien, M. J., Potentiometric, Electronic Structural, and Ground- and Excited-State Optical Properties of Conjugated Bis[(Porphinato)zinc(II)] Compounds Featuring Proquinoidal Spacer Units. *J. Am. Chem. Soc.* **2005**, *127* (14), 5186-5195.
169. Terenziani, F.; Katan, C.; Badaeva, E.; Tretiak, S.; Blanchard-Desce, M., Enhanced Two-Photon Absorption of Organic Chromophores: Theoretical and Experimental Assessments. *Adv. Mater.* **2008**, *20* (24), 4641-4678.
170. Mongin, O.; Porrès, L.; Charlot, M.; Katan, C.; Blanchard-Desce, M., Synthesis, Fluorescence, and Two-Photon Absorption of a Series of Elongated Rodlike and Banana-Shaped Quadrupolar Fluorophores: A Comprehensive Study of Structure–Property Relationships. *Chem. Eur. J* **2007**, *13* (5), 1481-1498.

Biography

Jong Kang Park was born in Ilsan, Korea on November 17th, 1980 and grew up in Gyeonggi-do and Seoul. He attended Yonsei University, Korea and received his B. S. in Chemistry in 2004. He served the Republic of Korea Army for two years and was discharged as a sergeant in 2006. Soon after, he went back to Yonsei University to pursue a master's degree in physical chemistry under the supervision of Prof. Dongho Kim and received his M. S. in Chemistry in 2008. He worked as a research associate in Natural Science Research Institute, Yonsei University until he moved to the United States. In 2009, he began his doctoral studies at Duke University. He has performed research in the areas of nonlinear optics and multiphoton imaging, co-advised by Professors Warren S. Warren and Michael J. Therien. He received several awards and fellowships including the Joe Taylor Adams fellowship, the John T. Chambers scholar, and an APS-DLS student travel grant. He published the following articles as a Duke graduate student: Wilson, J. W.; Park, J. K.; Warren, W. S.; Fischer, M. C., "Flexible digital signal processing architecture for narrowband and spread-spectrum lock-in detection in multiphoton microscopy and time-resolved spectroscopy." *Rev. Sci. Instrum.* 2015, 86 (3), 033707. Park, J. K.; Fischer, M. C.; Susumu, K.; Therien, M. J.; Warren, W. S., "Femtosecond pulse train shaping improves two-photon excited fluorescence measurements." *Opt. Lett.* 2014, 39 (19), 5606-5609. (The full list of his publications can be found in his LinkedIn webpage - <https://www.linkedin.com/in/jongkangpark>)